Efficient Power Coupling to Waveguides in High Index Contrast Systems

Victor T. Nguyen

Submitted to the Department of Materials Science and Engineering in partially fulfillment of the requirements for the degree of

Doctor of Philosophy in Electronic, Photonic, and Magnetic Materials

at the

MASSACHUSETTS INSTITUTE OF TECHNOLOGY

[February 2006]
September 2005

Author .....

Departments of Materials Science and Engineering

September 07, 2005

Certified by .....

Lionel C. Kimerling

Thomas Lord Professor of Materials Science and Engineering

Thesis Supervisor

Accepted by .....

Gerbrand Ceder

Chair, Department Committee of Graduate Students

Efficient Power Coupling to Waveguides in High Index Contrast Systems

by

Victor T. Nguyen

Submitted to the Department of Materials Science and Engineering in partially fulfillment of the requirements for the degree of

Doctor of Philosophy in Electronic, Photonic, and Magnetic

Abstracts

Future integrated optical circuits will hold, on a single chip, several optical components that communicate via high index contrast waveguides. Silicon nitride (Si_xN_y) and silicon oxynitride ($Si_xO_yN_z$) waveguides with silicon oxide cladding can be used to guide light on a chip because they have small dimensions, low scattering loss, and can be fabricated with silicon-based technology. With more components on a chip, we need to develop novel technologies to seamlessly route the optical signal from one waveguide to multiple waveguides simultaneously, or from the optical fiber to a waveguide.

This thesis presents the design and fabrication of two such devices. The first is a compact multimode interference coupler, also called multi-mode interferometer (MMI), which can equally distribute the optical power from one input waveguide to multiple output waveguides. The prototypes were fabricated for silicon-rich Si_xN_y waveguides with 1 input and 4 or 8 output ports. The second device is a compact fiber-to-waveguide coupler, which can efficiently confine the light from an optical fiber to a sub-micron waveguide. The prototypes were fabricated for $Si_xO_yN_z$ waveguide of index 1.70. The advantages of these couplers are their very compact size, high efficiencies, and their fabrication process can be adapted by mainstream silicon-based manufacturing technology. In addition, their designs are very robust and can be applied for efficient coupling into any high index contrast dielectric waveguide.

Thesis Supervisor: Lionel C. Kimerling

Title: Thomas Lord Professor of Materials Science and Engineering

Acknowledgements

I would like to thank the many people whose supports have helped me to survive the five years at MIT. First and foremost, I would like to express my deep gratitude to my advisor, professor Kimerling. Professor Kimerling is a great leader and with his guidance, I have navigated through the challenges and obstacles of research at MIT. Professor Kimerling values the students' works and intellect. He always makes time to discuss the research problems with me even with his very busy schedule. The conversations with Kim are always intellectually stimulating. He has helped me to develop a wider vision, to think of larger issues and solutions from solving immediate problems. I thank you, Kim for all your supports and for sharing your vision of future photonics research with me.

My research would have taken much longer if there were not weekly discussions with Dr. Jurgen Michel and Dr. Anu Agarwal. Jurgen and Anu have very deep understanding of photonics research and I am very grateful that they have shared their immense knowledge with me. Coming from a Chemical Engineering background, I had limited knowledge of how optical devices work. By asking me critical questions, they help me to explore different aspects of the problems. As a result, I have developed a deeper, fuller understanding of each research topic. Whenever I encounter a research problem that looks like impossible to solve, a knock on their office's doors is all it takes. Suddenly, there are so many possible solutions just waiting for me for try out.

Every one of my EMAT colleagues has enriched my research and personal life at MIT. I feel comfortable asking for help from any of you because I know that you will try to help out as much as you can without any reservation. I have enjoyed all the intelligent and animated discussions with Shoji, Trisha, Dan, Mark, Donghwan, Jifeng, Ching-yin, Yasha, Noks, Mike, Dave, Sajan, and Xiaoman. I would like to thank Mindy and Ellen for letting me buy all those software and computer equipments. I have a privilege of knowing you all.

I would like to thank Dr. John Yasaitis from Analog Devices for all his help and advices with device fabrication. Your diagnoses of many problems we faced in our collaborative work were precise and we were able to quickly develop solutions or workarounds. The staff at MTL has also contributed so much to the success of my research. I would like to express my gratitude to Vicky, Paul, Bob, Paudely, Eric, Donal, Bernard, Brian, Kurt, Dan and Tim who helped me to find solutions that enables my research to proceed. You always spend a lot time and effort to make sure that the MTL machines to operate at their capacities and I have the optimal recipes to do what I need in my research. I also appreciate all the help and advices from Ms. Kathleen Farrell at the department headquarters.

I am forever in debt to my parents, who have instilled in me the values of education, the work ethics, integrity, and compassion that I hold dear in both my professionally and personal life. I also want to thank my grandparents, my aunts and uncles, and cousins who had helped my family to settle down when we first arrived in the United States.

Last but not least, I would not be successful in my work without the support of the love of my life, Jennifer. With you by side, I feel like anything is possible. You cook me good meals, listen to my problems and frustrations when my experiments were not working correctly. Your love and encouragement re-energize me everyday and they have helped me to overcome many challenges at work. A happy graduate student is a productive researcher. I wish that our last few years together are only a prelude to many wonderful years to come. I devoted this thesis to you, my love.

I apologize if I have missed anyone. Once again, I would like to thank you all for your contributions to my work and my life. I hope that in some ways, my friendship has added a little bit to the richness to your lives.

Cambridge, Massachusetts. July 2005.

Table of Contents

List of Figures

Chapter 5:

V-1: The top views of fabricated 1x4 and 1x8 MMI ridge structures show that output waveguide ports are well defined well at separation of 0.8 μm.

V-2: Schematic of the optical bench setup for near-field output measurements. Power uniformity is calculated by comparing the gray-scale intensities of output beams.

V-3: Optical attenuator of 3.3 OD was used to avoid saturation of the detector with input light from a 1x4 MMI.

V-4: Variation of the light intensity with respect to the distance from the detector left edge. Calibration curve is plotted.

V-5: (A) The output power uniformity at the ports of 1x4 MMIs with w=7 μm at optimal length 25 μm. (B) Near-field output of one such MMI structure.

V-6: Near field output of 1x4 MMI ridge structures at w=8, 10 μm with silicon-rich Si_xN_y core. The outputs are uniform across the 4 ports.

V-7: (A.)Variation of output power ratio with length for 1x4 MMI structure of w=7 μm. (B) Near field output for MMI structures with length 15-21 μm shows variation in power distributions

V-8: FDTD simulation results for 1x4 MMI of w=7 μm and L=19 μm show non-uniform power distribution.

V-9: (A) Uniform power output distribution of 1x8 MMI structures of w=18 μm, L=82 μm. (B) Near field output from all 8 ports for one such MMI structure.

V-10: Schematic of the optical bench setup for direct output power measurements is shown.

V-11: Normalization of measured throughput power of 4 output waveguides of a Si_xN_y MMI coupler of w=10 μm and L=56 μm.

V-12: Similarly good power output uniformity was measured for a Si_xN_y MMI coupler of w=18 μm and L=88 μm.

V-13: Measured and FDTD simulated coupling efficiencies for 1x4 MMI couplers with respect to its width.

V-14: Schematic drawings of different width MMI couplers and the waveforms at the exiting facets demonstrate the lower coupling efficiency at larger width.

V-15: (A) Measured and FDTD simulated coupling efficiencies for 1x4 MMI couplers at 1st and 2nd distances a 4-fold image is generated. (B) The reduction in coupling efficiency at longer distance can be explained by the generation of a 2-fold image.

Chapter 6:

VI-1: Graded index fiber to reduce spot size from Shiraishi et al is shown. Their design's limitations are large focal beam size and low error tolerance fabrication.

VI-2: SEM images of inverse silicon taper fabricated by Shoji et al are shown. The limitation of their design is long millimeter device length and high requirement for accurate lithography technique.

Chapter 7:

VII-1: Diagram of proposed coupling scheme from fiber to on-chip waveguide is shown. The structure simultaneously transforms the light vertically by asymmetrical GRIN and horizontally by lens & taper.

VII-2: Vertical step-wise index profile of our 7-layer asymmetrical GRIN structure is illustrated.

VII-3: 2D FDTD simulation results for the proposed asymmetrical GRIN shows self-focusing effect and also high coupling efficiency at L=19 μm.

VII-4: 2D FDTD simulation results for a tapered lens shows high coupling efficiency for input width w=8 μm

VII-5: FDTD simulation of coupling efficiency as a function of misalignment in the lateral direction is shown.

VII-6: FDTD simulations results for coupling efficiency as a function of vertical misalignment are plotted.

Chapter 8:

VIII-1: Variation of index with flow rates of SiH_4 precursor in PECVD recipes to deposit $Si_xO_yN_z$.

VIII-2: Variation of index with flow rates of SiH_4 precursors in PECVD recipes for $Si_xO_yN_z$ films of index < 1.50. Their recipes are developed with high N_2O flow rate

VIII-3: PECVD recipes for $Si_xO_yN_z$ films of index from 1.75-1.90 are shown.

VIII-4: Schematic illustration of the setup to measure slab loss with prism coupler. Measurement results of this method do not include scattering loss associated with fabrication of waveguides.

VIII-5: Light intensity as a function of slab mode propagating distance measured at: 1307 nm and 1550 nm.

VIII-6: Schematic illustration of process flow to fabricate $Si_xO_yN_z$ waveguides using a silicon mask is shown.

VIII-7: SEM image of unclad waveguide index 1.70, defined by silicon mask and CHF_3 etching is shown. The profile angle is ~78° with relatively smooth sidewall.

Chapter 9:

IX-1: Process flow illustration for etching a $Si_xO_yN_z$ film using a PR mask and high density plasma (HDP) is shown

IX-2: SEM cross-sectional image of 7 μm $Si_xO_yN_z$ after RIE using thick PR mask is shown. The image shows severe mask erosion that transfers to small angle profile.

IX-3: Process flow for etching thick $Si_xO_yN_z$ film using thin silicon mask and CHF_3 etching gas is shown.

IX-4: Cross sectional SEM images of 6 μm $Si_xO_yN_z$ after RIE using a silicon mask. The image shows no mask erosion that leads to a profile angle of near 80°.

IX-5: Etch rate variation with addition of small 1 sccm O_2 flow. Silicon/Oxide selectivity reduces by ½.

IX-6: SEM image of 6 μm thick $Si_xO_yN_z$ film etched with (CHF_3 / O_2) plasma. Isotropy increases with O_2 mix.

Chapter 10:

X-1: Process flow for fabrication of the coupler in MTL. The devices were defined by 3 main steps that associate with 3 masks.

X-2: (A) Improving the layer alignment accuracy by increasing the thickness of the silicon layer. (B) Alignment is more accurate and consistent as observed from images taken from microscope.

X-3: Etch properties comparison shows that the recipe with lower power and higher pressure have better mask selective and on-wafer etch rate uniformity.

X-4: SEM images of the unclad tapers defined by etching of $Si_xO_yN_z$ stack with CHF_3 reveal excellent alignment of the stack and the waveguide. The sidewall is smooth and profile angle is 78 degree.

X-5: SEM image shows effect of sloping profile by overlap of structures.

X-6: Two available methods of removing thin silicon films in ICL, by plasma and by TMAH.

X-7: SEM images of $Si_xO_yN_z$ stack on silicon substrate after TMAH etch indicate isotropic etching of silicon etch stop layer.

X-8: Schematic illustration of the wafer topography after thick oxide upper clad was deposited. The peaks and valleys were formed by etching $Si_xO_yN_z$ stack.

X-9: A schematic illustration of the process flow that defines the input facet of the couplers is shown.

X-10: Relative heights of two sets of alignment marks with respect to the couplers are shown.

X-11: Re-printing of alignment marks on the top oxide cladding enhances their chances of being detected through thick silicon film.

X-12: SEM images reveal $Si_xO_yN_z$ stacks being etched due to insufficient PR coverage at wafer's high points. Planarization of the 6-μm high oxide bump is required.

X-13: The SEM images show fiber input facet of the coupler structure with the slope sidewall and etching of silicon substrate. The sidewall is very smooth to have minimal scattering loss at the input interface.

Chapter 11:

XI-1: Schematic of the Newport Auto Aligner setup for measuring power that transmits through the coupler is shown. Single mode fibers SMF28 and Nufern980 were used in measurements.

XI-2: 2D FDTD simulations taking account for the sloping profile show a maximum 0.81 efficiency for Nufern980 fiber.

XI-3: Theoretical coupling efficiency calculated for our 3D structures shows highest efficiency obtained at 19.5 μm when IMF= 1.75 is used.

XI-4: A comparison, of the experimentally measured coupling efficiency and effective FDTD simulations, shows similar variation with structure length. Highest coupling efficiency of 0.61 is achieved at a coupler length of 20 μm.

XI-5: Schematic of silicon mask removal process with He/Cl_2 plasma is shown.

XI-6: Theoretical FDTD curve adjusted for silicon film insertion. The curve displays a better fit to the experimentally measured data

XI-7: Coupling efficiency, both, measured from the fabricated couplers, and calculated from effective FDTD simulations, is high for input width which is close to the MFD of the fiber.

XI-8: Similar trend with respect to length of the coupler is observed for SMF28 input fiber. Highest coupling efficiency of 0.45 is achieved.

XI-9: Coupling efficiency with respect to misalignment on *XY* plane for SMF28 input fiber to the tested coupler.

XI-10: Variation in coupling efficiency with respect to radius of planar lenses is shown. The improvement in coupling efficiency is due to both lens' focusing effect and by matching its radius to the curvature of the incoming fiber's guided mode.

XI-11: Propagation loss of $Si_xO_yN_z$ single mode waveguide with respect to wavelength in C-band

XI-12: Insertion loss with respect to wavelength from 1520 nm to 1620 nm of our fabricated coupler structure shows small variation.

XI-13: (A) SEM image of a box shape coupler connected to a $Si_xO_yN_z$ waveguide. (B) Experimentally measured data indicates the focusing effect in GRIN box coupler that results in efficiency higher than direct coupling.

Appendices:

A-1: The AFM results for a-Si film deposited by PECVD using SiH_4 / Ar precursor.

B-1: Chromatic dispersion curve for $Si_xO_yN_z$ films deposited with PECVD technique. The dispersion effect is stronger with higher index (more silicon atoms) materials.

List of Tables

VIII-4: Slab mode propagation losses for PECVD $Si_xO_yN_z$ films at index 1.70. The propagation loss at 1550 nm is lower for materials deposited at higher substrate temperature.

Chapter 9:

IX-1: Compensating for frontside wafer bow is accomplished by depositing oxide film in the back as demonstrated on wafers with 7 μm thick $Si_xO_yN_z$ film.

IX-2: Etch rate rate calibration for $Si_xO_yN_z$ / oxide and PR mask in high density plasma chamber.

IX-3: Higher selectivity to silicon mask was observed when CHF_3 gas is mixed in with CF_4 for plasma etching in P5000.

IX-4: Etch rate calibration for standard anisotropic etch of silicon in LAM490 chamber with He/Cl_2 plasma.

IX-5: Etch rate calibration for anisotropic etch of $Si_xO_yN_z$ in HDP chamber with different plasma chemistries. Low selectivity to the silicon mask is due to high ion bombardment.

IX-6: Etch rate calibration for anisotropic etch of $Si_xO_yN_z$ / SiO_2 in P5000 chamber at different powers and pressures. High selectivity to the mask is achieved.

Chapter 11:

XI-1: Maximum throughput power obtained through the Newport station with different connecting fibers.

Chapter 1: Introduction

1.1. Motivations

The vision of silicon optoelectronics, which is the integration of optics and electronics on silicon substrate, will rapidly unfold in a very near future following many achievements in the last few years. Future integrated optical circuits will hold, on a single chip, several optical and electronics components that communicate via high index contrast (HIC) waveguides. With enhanced functionality of a chip, we need to develop technologies to seamlessly route the optical signal from one waveguide to multiple waveguides on a same chip, from larger scale fiber network to an on-chip waveguide and vice versa.

This thesis presents our solutions to the above problems via the demonstrations of two working prototypes. Our works focus on silicon nitride (Si_xN_y) and silicon oxynitride ($Si_xO_yN_z$) waveguides with silicon oxide cladding. Our solution for routing and splitting optical signal on-chip is the design of a multimode interference coupler, also called multimode interferometer (MMI). They are the first fabricated for Si_xN_y single mode waveguides. Our fabricated prototypes are very compact, 100 times smaller than typical silicon on insulator structures. In addition, they demonstrate uniform output power distribution and high coupling efficiency of 80%. These multimode interference couplers are alternatives to Y junction splitters and H-tree in distributing optical signal effectively throughout the chip. The couplers can also be incorporated into complex designs such as phase diversity network, Mach-Zehnder switches and modulator.

Although optical signal is guided on-chip by planar waveguides, larger scale communications such as from chip-to-chip and from board-to-board are done by single mode optical fibers. For wide scale applications of integrated optical circuits, we need to efficiently route the signal from a single mode fiber to an on-chip waveguide and vice versa. Direct coupling from these two devices has huge insertion loss due to their mismatch in size. We have fabricated prototypes for a novel coupling scheme to confine light from a single mode fiber to sub-micron $Si_xO_yN_z$ or Si_xN_y waveguides. The fabricated structure is compact (18-20 μm long), highly efficient (2.2 dB insertion loss from a cleaved Nufern980 fiber), and its robust design can be applied for effective coupling into Si-based single mode waveguides at a different laser wavelength.

We drew on the strength and knowledge of silicon-based fabrication technology to manufacture these efficient optical couplers presented in this thesis. As more electronics and photonics components are incorporated on a same substrate, having compatible fabrication technologies and processing on same manufacturing tools are essential for wide scale integration and commercialization in optoelectronics.

1.2. Outline of the thesis

This thesis can be divided into three main sections:

1. The development of low-loss Si_xN_y films by plasma enhanced chemical vapor deposition are presented in the next two chapters: chapter 2 and 3.

2. In chapter 4 and 5, we presented the design, fabrication, and characterization of multimode interference couplers to distribute and direct power from one waveguide to multiple output waveguides. The core material is high index Si_xN_y.

3. The following chapters from 6-11 report the design, fabrication, and measurements on a fiber to on-chip waveguide optical couplers. This highly efficient coupler design is used to confine light from large single mode optical fiber to a sub-micron single-mode $Si_xO_yN_z$ waveguide. Solutions for fabrication challenges that had been overcome during manufacturing process of the prototypes can be found in chapter 8-9.

Finally, the last chapter 12 summarizes the works in this thesis. Suggestions for future developments of power coupling and routing on HIC photonic platform are presented.

Development of highly robust dielectric films for HIC applications

Dielectric waveguides with core materials of $Si_xO_yN_z$ and Si_xN_y are alternatives to very high index silicon system. These dielectric waveguides can be used to guide light on a chip because they have small dimensions, low scattering loss. In addition, they offer flexibility in design with wide range of refractive indices.

We present in these chapters the development of Si_xN_y and $Si_xO_yN_z$ films at varying indices by plasma enhanced chemical vapor deposition (PECVD). By replacing NH_3 with N_2 as N-source precursor during the deposition, we had lowered the absorption loss in C-band caused by N-H bond vibration. The absorption loss and chromatic dispersion

curves of the materials are reported. The development of these films laid the foundation for manufacturing of many on-chip optical devices that require low loss and flexibility in index design.

Low loss, compact 1xN multimode interference couplers on HIC platform

In a future photonic integrated circuit, enhanced functionality requires the ability to route the input signal effectively to different parts of the chip. Equal power distribution among the branches and high power throughput are essential for a splitter design. In addition, small device dimensions, design flexibility, and improved fabrication tolerance are required in order to reduce cost and suitable for large scale manufacturing.

Our proposed design for multimode interference couplers satisfies all the above requirements. Design principles for the structures' length, width, minimum output port separation, and S-bend waveguides are presented in chapter 4. The fabricated devices for silicon-rich Si_xN_y waveguides are characterized by two complement optical measurements techniques presented in chapter 5. The measurement of near-field outputs provides information on the power output distribution. From the direct power measurements, both output uniformity and coupling efficiency can be calculated.

Highly efficient, compact fiber-to-waveguide coupler for HIC platform

The absence of efficient ways to connect optical fibers with on-chip waveguides is a large barrier to wide scale commercialization of optoelectronics devices. To design our fiber-to-waveguide coupler, we utilized a novel scheme which uses a vertically asymmetric

step-wise parabolic index profile and a combination of a lens and taper to achieve simultaneous vertical and horizontal confinement.

Fabrication a prototype to demonstrate the coupling principles of the design has many challenges. However, we had devised novel fabrication techniques to solve these problems. Chapter 8-9 illustrate techniques for improving profile of thick dielectric stack, lowering sidewall roughness, improving layer-to-layer alignment, and preventing formation of polymer micro masks. In chapter 11, the performance of the device with respect to the structures' parameters, wavelength, and connection misalignment are characterized. Optimizations for the design are suggested although the fabricated devices demonstrate high coupling efficiency in very compact structures.

Material Development for High-Index Contrast Dielectric Waveguide by Plasma Enhanced Chemical Vapor Deposition

High index contrast waveguides have been attracting considerable attention for dense integration of optical waveguides[1, 2]. It is well known that compact size bends can be made by increasing index difference between core and cladding. One major candidate is the Si/SiO_2 waveguide system where index difference is as much as 2.0. Another candidate is Si_xN_y/SiO_2 waveguide where index difference ranges from 0.5-0.8. For Si/SiO_2 waveguide, 1μm bend radius is achieved but scattering loss is high as reported by Lee et al[1, 3] and fiber/waveguide coupling efficiency is low since there is a large mode size mismatch between 0.5 μm single-mode silicon waveguide's core and single mode fiber mode field diameter of 7-10 μm.

Chapter 2: Deposition of Si_xN_y Films using NH_3 Precursor

2.2. Motivations

Dielectric materials such as silicon oxynitride ($Si_xO_yN_z$) and silicon nitride (Si_xN_y) are alternatives to very high index silicon waveguide. They offer flexibility in design with wide range of refractive indices, a developed understanding of their thin film properties and fabrication techniques. In addition, for Si_xO_yN or Si_xN_y waveguide with oxide cladding, scattering loss is reduced and coupling efficiency from single mode fiber is also higher due to its larger mode size. In these systems, small bend size is still possible. For

example, in Si_xN_y/SiO_2 waveguide with core index of 2.20, a 5-μm radius is required for 98% transmission and this is small enough to satisfy the demands of future opto-electronics circuits.

The drawback of Si_xN_y is its high absorption in the C-band wavelength. It has been reported that nitrogen-hydrogen (N-H) covalent chemical bond, formed during deposition process works as an absorption center at 1.55μm communication range[4-6]. For lower transmission loss, hydrogen must be removed by high temperature anneal, typically above 1000°C. The high temperature process is not compatible with other processes such as for Germanium detector/modulator integration where melting point is near 700°C. Anneal also causes film cracking problem due to high tensile stress[4]. Therefore, optimizing material loss at low process temperature is the key for constructing a dielectric HIC platform.

In this chapter, we will discuss the properties of Si_xN_y films at varying indices deposited by chemical vapor deposition (CVD) techniques. We will focus on the Si_xN_y films formed by plasma enhanced CVD. We have found that by replacing the NH_3 precursor with N_2, the film H content is reduced; thus propagation loss at 1550nm wavelength is lowered. As a result, annealing process is not required and low loss Si_xN_y films are suitable for Ge-detector integration on an optical circuit.

High quality silicon nitride films are deposited on silicon substrate by two chemical vapor deposition methods in ICL, the low pressure chemical vapor deposition technique (LPCVD) at 775°C and the plasma enhanced CVD (PECVD) at 400°C. Both techniques

are being evaluated in this section in search for a low loss, versatile material to fabricate Si_xN_y waveguides.

2.3. Low pressure chemical vapor deposition of Si_xN_y film

The silicon nitride films can be grown under low pressure condition at 775°C in a vertical thermal reactor (VTR). The precursors are dichloro-silane SiH_2Cl_2, ammonia NH_3 and nitrous oxide N_2O.

The Si_xN_y film formed by LPCVD has very low H content due to high substrate temperature which assists H out diffusion and the use of SiH_2Cl_2 precursor instead of SiH_4. As a result, the film has very small N-H bond density that leads to low absorption loss in C-band. Most papers report less than 5% H content[6-8]. In our experiment, we measured the FTIR absorption spectra of a 600 nm thick silicon rich nitride film. The first overtone absorption peaks of Si-H (2200 cm^{-1}) and N-H (3400 cm^{-1}) are non-observable. When a LPCVD Si_xN_y film (RI=2.20 @1550nm) is fabricated into a rectangular channel waveguide 1.0 μm x 0.3 μm, the Fabry-Perot waveguide loss reported by Akiyama is **0.92 ± 0.6** dB/cm[9].

Additional advantages of VTR grown film are zero wafer bowing and low surface roughness. These properties make VTR grown film good candidates for e-beam lithography work. The zero wafer bowing comes from the deposition occurring on both sides of the wafer. So, although the film has intrinsic stress, the wafer bow does not change from that of substrate. We have measured the surface roughness by atomic force microscope of a 0.4 μm thick silicon-rich Si_xN_y film (RI=2.20 at 1550nm). For 5 μm x 5

μm inspection area, the surface roughness average is 0.5 nm. PECVD film grown at the same index and thickness has the surface roughness of 2.3 nm at same measurement conditions.

Although the LPCVD Si_xN_y films have many desirable material and optical properties, they are difficult to fabricate and non-flexible with index engineering. LPCVD is limited to form films at certain indices since the deposition is dominated by equilibrium reaction at the interface at high temperature[6]. The VTR system in ICL can only deposit SiN at two indices (2.0 and 2.20). To develop a new recipe for a material with in-between index requires a lot of time and resources that the lab does not have.

The LPCVD deposition process is high temperature with low deposition rate. High temperature process makes integration with Ge, which can be used as detector in C-band a challenge. 2^{nd}, the system needs long time to achieve equilibrium conditions for the reaction to proceed and deposition rate is slow (~30 A/min). In addition, since the VTR system at MTL is isotherm, non-uniform deposition rate observed along the wafer boat. A 0.6% thickness variation for two wafers in consecutive slots is measured.

To achieve more freedom in designing HIC material for optical integrated circuit, a deposition process at lower temperature with more flexible in index engineering must be developed. Plasma-enhanced CVD is a well understood process for dielectric deposition that can fulfills these requirements. We will present our work in developing low-loss PECVD Si_xN_y films with a wide range of index on Novellus Concept 1 system first. To

lower the H atomic percentage and absorption loss in C-band, we develop the PECVD film deposited with SiH_4/N_2 chemistry in the Applied Materials DxZ reactor.

2.4. Si_xN_y film growth by PECVD using NH_3

PECVD reaction to form Si_xN_y film with SiH_4/ NH_3 precursors are described by Smith et al as followed [10]:

With NH_3 as oxidant, silane SiH_4 is converted to $Si(NH_2)_4$ and $Si(NH_2)_3$ radicals. They undergo the elimination of ammonia to form amorphous silicon nitride Si_3N_4 via two overall reactions

$$SiH_4 + 4\ NH_3 \rightarrow Si(NH_2)_4 + 4\ H_2$$

$$3\ Si(NH_2)_4 \rightarrow Si_3N_4 + 8\ NH_3$$

The higher the substrate temperature, the further the second reaction proceeds. At standard deposition temperature of 400°C, there is approximately ~15-20 atomic percent of H bonded to N or Si atoms. In excess oxidant regime, most H will bond to N in NH and NH_2 groups. We need to reduce the N-H bond density with high temperature anneal in order to have a low loss waveguide for optical transmission in C-band. Our first experiments were with the Novellus Concept 1 chamber, the PECVD tool available at that time.

2.4.1. PECVD growth of stoichiometric Si_xN_y

Silicon nitride and silicon oxynitride dielectric films are used as insulators between metallic interconnects in semiconductor applications. To have a good insulating film, the Si-H bond density must be minimal since it is electrically leaky. As a result, most conventional PECVD machine such as the Concept 1 was designed to deposit N-rich SiN

(RI=1.92-2.0) films using SiH_4, NH_3 precursors and N_2 as a diluent to enhance uniformity of thickness and index on the wafer.

The Concept 1 is a mixed-frequency system that generates power at two frequencies. The high frequency HF is set at 13.56 MHz to control how fast it can break the molecules and form the plasma. The low frequency LF power is set at 380 kHz and to control the radicals and molecules transports to the substrate. As a result, the deposition rate is controlled by the powers at high frequency while the film stress and surface morphology is directly affected by LF power.

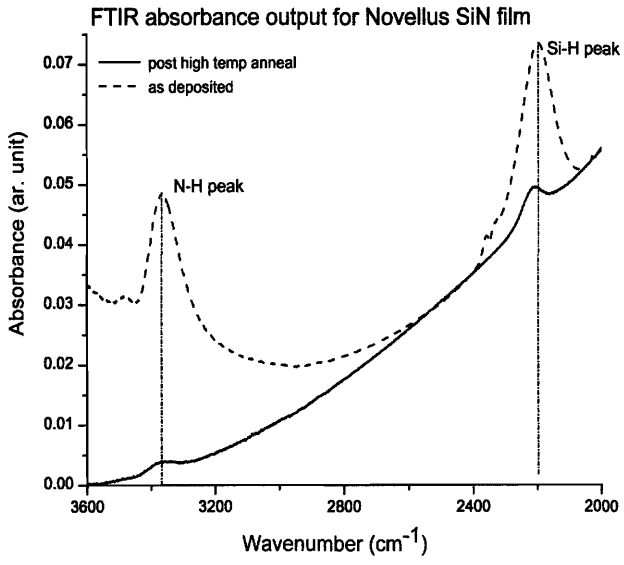

Fig II-1: FTIR scan PECVD Si_xN_y (RI=2.04) film before and after high temperature anneal. Intensity reduction in absorption peaks indicates lower N-H and Si-H bond densities after anneal.

High temperature annealing process leads to the reduction of hydrogenated bonds as indicated by the Fourier Transformation in Infrared (FTIR) spectra in Figure II-1. The deposition of Si_xN_y (RI=2.04) at 400°C results in a film with ~18% H atoms as calculated from the FTIR spectra based on the method developed by Lanford and Rand [11]. We annealed the Si_xN_y film to reduce its H atomic percentage. After annealing at 1050°C for 90 minutes, the N-H and Si-H bonds are significantly reduced to ~3%. The

film index will also increase due to faster out-diffusion of N atoms compared to Si atoms. The post-anneal film has a 2.13 index.

2.4.2. Reducing absorption loss in Silicon-rich Si_xN_y (RI=2.05-2.20)

Increase the index of the PECVD Si_xN_y material has two advantages. First, we can increase the optical device density on-chip with higher index contrast to the cladding. Second, as the film becomes more silicon-rich, the H atom will preferentially bond to Si atom; thus it reduces the N-H bond density and absorption loss at 1550 nm. We created the recipes for deposition of Si-rich Si_xN_y by increasing the SiH_4 flow. The parameters kept constant are p=2.60 torr, NH_3 flow rate of 4000 sccm, N_2=1600 sccm. The HF power is 700 W and LF at 300 W. Then, the films were annealed at 1050°C for 1 hour in N_2 atmosphere to further increase the refractive index.

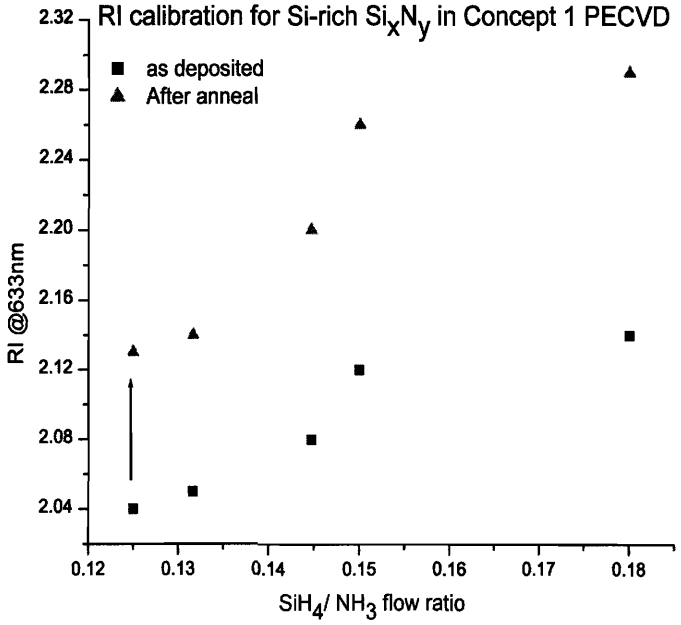

Figure II-2. Calibration curve for RI at 630 nm for Concept 1 Si_xN_y films shows index increases with SiH_4 flow. The film becomes more silicon-rich after high temperature anneal from the diffusion of N atoms.

The calibration curve for Si-rich Si_xN_y deposited in Concept 1 is drawn in Figure II-2. The refractive indices were measured at 630nm by spectral ellipsometry.

We compare the H atomic percentage via FTIR absorption for Si_xN_y films at index 2.04 and 2.12. Although the total H atomic percent is similar for both films, the si-rich SiN (RI=2.12) has smaller number of H atoms bonded in the N-H configuration.

	Total H atomic%	**H% atom in N-H bond**
PECVD Si_xN_y RI=2.12	22.1	4.5
PECVD Si_xN_y RI=2.04	18.3	8.7

Table II-1: Comparison of H atomic % for Si_xN_y films at different indices.

We were not successful in measuring the Fabry-Perot waveguide loss for film of index 2.04. However, the waveguide of Si_xN_y RI=2.12 has **2.3 ± 1.0 dB/cm** loss measured by Fabry-Perot. For its annealed film, when a same dimension waveguide is fabricated, the loss is **2.07 ± 0.5** dB/cm[9]. The waveguide loss is higher than that of LPCVD.

We observed that any PECVD Si_xN_y film with thickness higher than 0.5 μm will crack during the anneal process. The limit on how thick we can grow and anneal the Si_xN_y films is a huge constraint for our waveguide design. A thin, rectangular waveguide is polarization sensitive and it is harder to couple in the light from fiber. We also notice from the above graph that the index shift during anneal is larger with Si-rich nitride. For example, under the same annealing conditions, a Si_xN_y film with an as-deposited index of 2.04 has a $\Delta n=0.09$ shift while the film at RI=2.12 as-deposited has a shift of $\Delta n=0.13$. We believe that in silicon rich material, the N out-diffusion is enhanced by the formation of NH_3 gas via the following reaction

$$Si_2N\text{-}H + 2N\text{-}H \rightarrow 2\ Si\text{-}N + NH_3 \qquad \Delta E = -0.43\ eV\ [12]$$

Higher Si_2N-H bond density in high-index Si-rich film drives the reaction more to the right.

2.4.3. Material dispersion in Si_xN_y- Index variation with wavelength

Because of the chromatic dispersion effect, the refractive index of a silicon-based material varies over the 0.6-1.6 spectrum range. Conventional characterization tools for thin film such as the KLA-Tencor UV1280 ellipsometer in ICL cannot measure refractive index in infrared because it uses short spectral scan from 300nm to 700nm. There are ellipsometers with longer spectral scan designed to solve this problem. However, such system like the SOPRA SE-5 takes one hour to scan a point and it is placed outside ICL. Since our devices are designed to work around 1550nm or at 1300nm, and fabricated in ICL, we need to combine both methods to fully characterize the film's optical property.

Spectral ellipsometer systems use the Cauchy equation to extrapolate the index of a thin film at a certain wavelength within its spectral scan. The Cauchy's dependence of index to wavelength is

$$n(\lambda) = A + \frac{B}{\lambda^2} + \frac{C}{\lambda^4} + \ldots$$

The coefficients A, B, C of a material depends on its atomic composition and bond density configuration. We extract these coefficients for different PECVD Si_xN_y films in the 0.6 μm to 1.6 μm range. The data is plotted and the coefficients are extracted in the Table II-2 below.

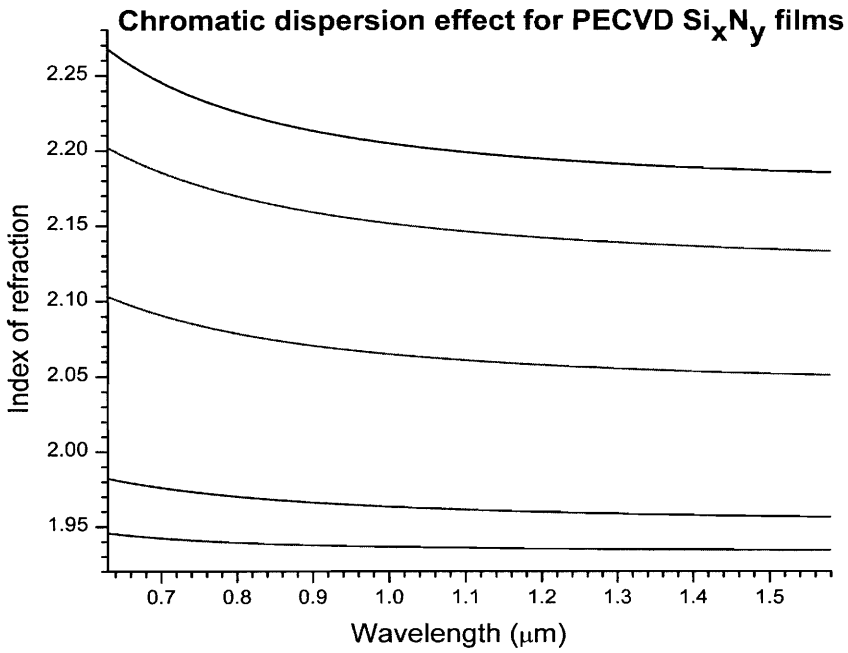

Figure II-3: Cauchy's model extrapolation curve for different Si_xN_y films to predict their refractive index at visible and near IR wavelengths.

	Cauchy parameters			Refractive Index		
	A	*B*10³*	*C*10⁴*	@630 nm	@1300 nm	@1550 nm
1.	2.174	26.529	42.015	2.266	2.191	2.185
2.	2.121	29.559	10.173	2.200	2.138	2.133
3.	2.042	22.006	9.118	2.103	2.056	2.052
4.	1.952	10.870	4.396	1.981	1.958	1.956
5.	1.933	2.040	10.552	1.942	1.934	1.933

Table II-2: Cauchy's parameters for PECVD Si_xN_y film to describe the chromatic dispersion

2.5. $Si_xO_yN_z$ film growth by PECVD with $SiH_4/NH_3/N_2O$ chemistry

We also investigated the properties of silicon oxynitride ($Si_xO_yN_z$) film as core material for HIC waveguides. The $Si_xO_yN_z$ film at index 1.70 is deposited by PECVD in Concept 1 using SiH_4, NH_3 and N_2O as precursors. To measure the material absorption, slab-mode propagation loss is a good technique since its results do not include losses induced during

device fabrication. The slab-mode propagation losses results at 1310nm and 1554 nm are **0.5 dB/cm** and **7.5 dB/cm**, respectively. Since the N-H absorbs light from 1510 nm to 1560 nm, the difference in loss results at these wavelengths indicates a high number of N-H bonds that exist in the film.

To reduce the N-H bond density, the deposited film is annealed at high-temperature. We have observed for this $Si_xO_yN_z$ material that any film thicker than 0.6 μm will crack during the anneal process. As a result, we cannot fabricate a low-loss square single-mode waveguide at 0.9 μm thick based on this material.

2.6. Summary and Conclusions

In this section, we have looked at the optical and mechanical properties of Si_xN_y films deposited by chemical vapor deposition techniques. The LPCVD method produces films with low H content and small absorption loss. However, it is a high-temperature process and can only deposit materials at certain indices. An alternative is the PECVD method which offers flexibility in index engineering and low temperature processing. To achieve low absorption loss with conventional PECVD films, high temperature anneal is an option. Si_xN_y films thicker than 0.5 μm will crack during the anneal process. We need to develop new PECVD chemistry that can form low loss films that do not require high-temperature anneal.

Chapter 3: Developing a Si_xN_y Film with Lower Absorption-PECVD using N_2 Precursor

Plasma-enhanced chemical vapor deposition (PECVD) of silicon nitride is a promising technology for the fabrication of photonic devices, due to the method's flexibility in index engineering, good on-wafer, and wafer-to-wafer uniformity, much higher deposition rate compared with LPCVD, and low thermal budget. However, Si_xN_y film deposited by conventional PECVD chemistry with NH_3 precursor has high N-H bonds that absorb in 1550nm. An alternative to film annealing in lowering the film absorption loss is eliminating the H sources in the precursors. Replacing H in NH_3 with its isotopic deuterium D reduces N-H bonds but the process is not cost-efficient[13]. Instead, we explore the use of N_2 gas as the only N-source in the Si_xN_y deposition.

3.1. Replacing N-source in PECVD to reduce absorption loss

Since the N-N bond is covalent, a higher plasma field is required to break their bond and to form N• radicals. The Novellus Concept 1 PECVD system is not configured to produce high density plasma field and N_2 is only used as a diluent for Si_xN_y deposition. On the other hand, the Applied Materials DxZ chamber with its patented gas distributing face place can create a local hollow cathode effect[14] for N_2 gas to be dissociated. The system was donated by Applied Materials and started online in September 2003.

In the SiH_4/N_2 PECVD plasma, the lightweight N• and SiH_m• radicals are formed in contrast to the heavy $SiH(NH_2)_x$ radicals in SiH_4/NH_3 plasma [10, 15, 16]. The SiH_m and N radicals react to form Si-N bond network on the substrate surface. Since the H atoms

now only come from the SiH_4, we expect the total H% to be lower than in film deposited by conventional (SiH_4 /NH_3) chemistry at the same index. In the case of excess N radicals and low SiH_4 flow, the N-H bonds are still formed via the reaction:

$$SiH + N^{+} + SiH_2 \rightarrow Si\text{-}NH\text{-}SiH_2 \quad [12]$$

To demonstrate the reduction in absorption loss at 1550nm of the PECVD film deposited with SiH_4/N_2 chemistry, we compared its propagation loss in slab mode with a same index film deposited with SiH_4/NH_3 chemistry. The films were deposited at same substrate temperature of 400°C in the Applied Materials reactor. The first film is deposited with SiH_4 /NH_3 and N_2 as diluent gas. In the 2nd deposition recipe, only N_2 gas serves as the N-source for the Si_xN_y. FTIR spectra of the two films are collected to calculate the H atomic percentages in two films. The results are listed in the Table III-1.

	RI	**Total H atomic%**	**% of H atoms in N-H bond**
PECVD Si_xN_y film of conventional chemistry - SiH_4/NH_3 precursors	1.95	18.3	55
Si_xN_y film deposited with SiH_4/N_2 precursors	1.97	9.9	60

Table III-1: Comparison of H atomic % and N-H bond density for two PECVD films with different N-source precursor

The new chemistry deposits a film of similar index but with smaller total H% and N-H bond density. The lower N-H bond density is reflected by the lower absorption loss at 1550nm as seen in the slab loss measurement results. The two above films are measured at 1310nm where there is no N-H vibration to absorb light, and at 1550nm near the peak

of N-H's 2nd overtone absorption. As observed in Figure III-1, the two films have similar baseline loss at 1310 nm. However, at 1550nm the Si_xN_y film deposited with SiH_4/N_2 precursors has a low loss of **2.8 ± 0.3 dB/cm** while the film of conventional PECVD method has a higher **4.3 ± 0.2 dB/cm** absorption loss.

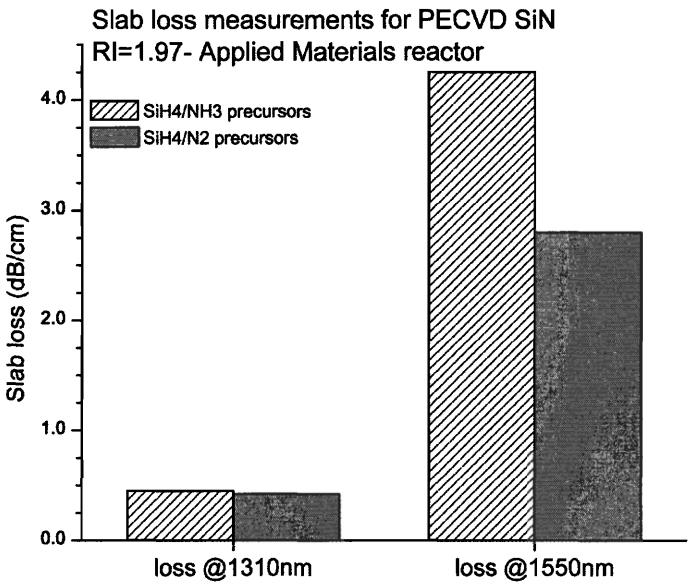

Fig III-1: Slab loss measurements of PECVD Si_xN_y films deposited in Applied Materials reactor. The film deposited with SiH_4/N_2 shows lower absorption loss at 1550nm which indicates a reduction of N-H bonds in comparison with film deposited with conventional SiH_4/NH_3.

3.2. Index engineering with SiH_4-N_2 PECVD

For Si_xN_y film deposited with SiH_4/N_2 precursors, the N-H bond density can be reduced with increasing the SiH_4 gas flow. At higher concentrations of SiH_m radicals, more di-silane Si-Si and Si_3-N bonds are formed. Since we now have a deficiency of N dangling bond, the H atoms will preferentially stay in the Si-H configuration. As the SiH_4 flow increases while the N_2 flow stays constant, the film index also increases.

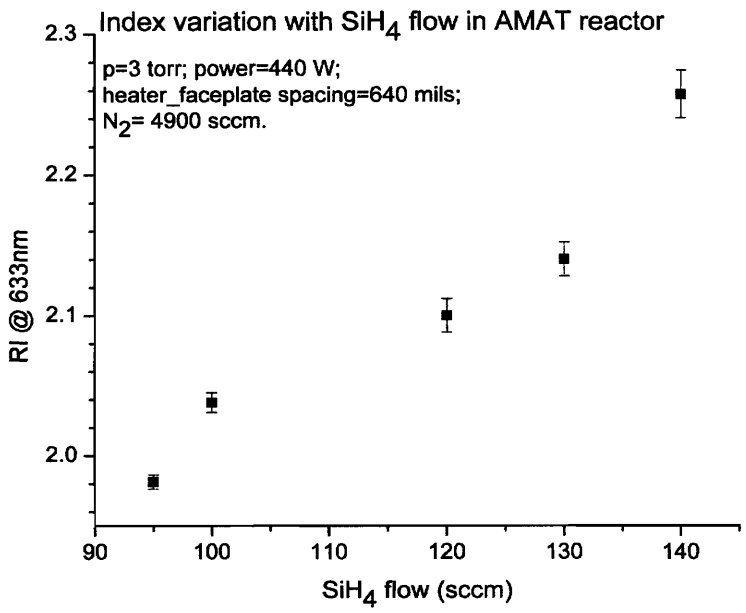

Figure III-2: Index variation with the SiH_4 flow in the Applied Materials reactor. Highest index of 2.25 is achieved.

We achieve a high index of 2.25 with an on-wafer variation of 0.015. As we increase the SiH_4 flow further for higher index, the refractive index uniformity on the wafer is reduced. The reason is that since the diameter of the Applied Materials reactor is not much larger than that of the wafer, edge effect is observed for wafers deposited with recipes using high SiH_4 flow rates. The refractive index is highest at the center of the wafer and drops off at its edge. One suggested solution is to increase the N_2 flow which is also a diluent. However, that solution does not work well for us since our recipe sets the N_2 flow near the limit of its mass flow controller (MFC) of 5000 sccm. We need a larger MFC to implement recipes for silicon-rich Si_xN_y with index higher than 2.25.

Silicon-rich Si_xN_y film at index of 2.25 is characterized by FTIR for bonded H atomics % and by slab-mode propagation for absorption loss. Even though the total H atomic percent in the film is 14.4%, only 5% of those H atoms are in N-H configuration. It is a ten time reduction in N-H/ Si-H bond ratio from that of N-rich Si_xN_y film. The lower N-H bond density is reflected in the small difference in slab-mode propagation losses at

1310nm and 1550nm. The loss measured at 1310nm wavelength is **2.0 ± 0.1** dB/cm. At 1550nm, the loss is **2.2 ± 0.1** dB/cm.

3.3. Summary and Conclusions

High index contrast waveguides such as Si_xN_y with silicon oxide cladding are good alternative to silicon waveguide for guiding light on-chip because of their lower scattering loss and flexibility in design with a wide range of indices. Si_xN_y films deposited by conventional PECVD method with SiH_4/NH_3 have high N-H bond density which results in high absorption at 1550nm wavelength. By replacing NH_3 with N_2 in the recipe, we significantly reduce the total H atomic percent and the N-H bond density. For example, at Si_xN_y film index of 1.97, the slab-mode propagation loss is reduced from 4.3 dB/cm to 2.8 dB/cm when the SiH_4/N_2 recipe is used. By increasing the SiH_4 flow in the PECVD recipe, we can increase the index of the material. Silicon-rich Si_xN_y has two advantages. The first is with higher index contrast to the silicon oxide cladding, smaller waveguide dimension and higher device density integrated on-chip can be achieved. The second advantage is silicon-rich film has lower N-H bond density. A Si_xN_y film at index of 2.25 has a low slab-mode propagation loss of 2.2 dB/cm.

Chapter 4: Design of Planar Multimode Interference Couplers for Si_xN_y Waveguides

4.1. Introduction

In a future photonic integrated circuit, enhanced functionality requires the ability to route the input signal effectively to different parts of the chip. As a result, equal power distribution among the branches and high power throughput is essential for a splitter design. In addition, small device dimensions, design flexibility, and improved fabrication tolerance are required in order to reduce cost and suitable for large scale manufacturing.

There has been a growing interest in the applications of multi-mode interference coupler, also called multi-mode interferometer (MMI) to direct and distribute optical signals to multiple waveguides on a chip since they satisfy all the above requirements. MMI can be incorporated into complex designs such as phase diversity network, optical clock distribution, Mach-Zehnder switches and modulator. The MMI principles formulated by Ulrich and Soldano [17-19]had been realized via the fabrication of devices based on Al_2O_3/SiO_2[20, 21], InGaAsP/InP[22], and silicon on insulator (SOI)[23-25] material systems.

Integrating the Al_2O_3/SiO_2 and InGaAsP/InP material systems with silicon-based waveguides is very difficult because of incompatible fabrication methods and substrates. SOI-based interference couplers have rib input and output waveguides to minimize the scattering loss of the device. As a result, their most important draw back is the large

dimensions of both the MMI and the rib waveguides. The typical width of a 1x2 SOI MMI is already 40 to 50μm. Thus, its length is in the order of millimeter [mm].

We had successfully fabricated MMI structures of silicon-rich silicon nitride core that yield uniform distribution of power output with higher than 80% throughput power. These 1x4 and 1x8 MMI's are also very compact with less than 100 μm long. We can save valuable on-chip real estate with this significant reduction of the devices' area. These structures were designed using modified calculations of 2D mode propagation analysis (MPA) method with effective index. Both near-field output and direct waveguide power measurements of these MMI structures were performed to fully characterize the transmission properties of the fabricated interference coupler devices.

4.2. Design principles for planar MMI coupler

Self-imaging in a 2D slab waveguide is described by Bryngdahl and Ulrich as the *property of multimode waveguides by which an input field profile is reproduced as single or multiple images at periodic interval along the propagation direction of the guide*[17, 19].

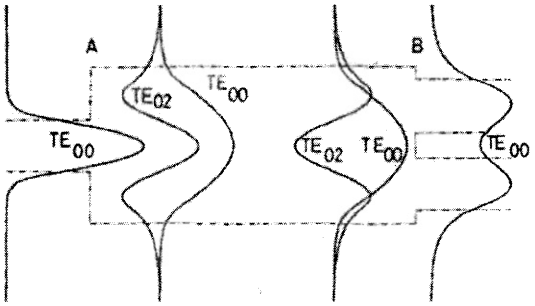

Figure IV-1. A schematic drawing of TE modes propagating in a symmetrical 1x2 MMI coupler[21]. Light is launched at the (A) facet and recovered from the two waveguides at (B).

The MMI structure is a waveguide that is designed to support multiple modes. The light is launched at one end through one or *N* single mode waveguides. *M* single mode waveguides are placed at the other end to

recover the output light as seen in the schematic picture of a 1x2 MMI exampled above. These MMI are described as *N*x*M* couplers. In our work, we designed symmetrical 1xN MMI couplers. The center line of the single input waveguide is aligned with the center line of the MMI. The output waveguides are equally spaced at the other end of the structure and are symmetrical with respect to the MMI's center line. The numbers of output ports investigated are 4, 8, and 16.

The mode propagation analysis (MPA) method proposed by Soldano et al [18]can be employed in designing 2D MMI slab structures. The advantage of MPA is its simplicity and design flexibility in determining the length at which the device yields uniform output. For 3D MMI structures, cross-sectional calculations using effective index method (EIM) combined with MPA, is used to produce a formula for MMI design.

For 2D propagation in a MMI structure of step index n_r and width W_M, the beat length L_π of two lowest-order modes is approximated as

$$L_\pi = \frac{\pi}{\beta_0 - \beta_1} \approx \frac{4}{3} * \frac{n_r W_e^2}{\lambda_0} \qquad \textbf{(4.1)}$$

where λ_0 is the propagation wavelength and W_e is the beam width of the MMI structure's fundamental mode. For high index contrast system where the wave is well confined within the structure, W_e can be approximated as the physical width of the MMI, W_M.

The first distance at which the single image is reproduced is $L = \frac{3 * L_\pi}{4}$. The distance at which an N-fold image is generated is $L_{N,p} = \frac{p}{N} * (\frac{3 * L_\pi}{4})$ **(4.2)** with p is an integer number (1, 2, 3...). If N waveguides are equally spaced at the end facet of a MMI structure length $L_{N,p}$, the output power propagates through each is expected to be equal. To design the length of a 3D MMI structure, in the above formula 4.1, the core index n_r is replaced by the effective index n_{eff} calculated from Apollo Photonics™ software.

To calculate the throughput power, the overlap of waveforms at input port and at each output port is integrated. However, in the MPA method, the description of the waveform with lateral distance is not formulated; thus, the power overlap cannot be calculated. As a result, full modal propagation analysis using finite difference time domain (FDTD) simulation were utilized to describe the mechanism of multimode interference in a MMI structure. A full 3D FDTD simulation requires large amount of time and computing power that we do not have. As a result, we collapsed the 3D structure into a 2D slab using effective index method and 2D FDTD simulations were performed to calculate the power exiting the output ports. The simulation results were also used to double-check the design of MMI length with the calculated value provided by the MPA method.

4.3. Design constraint on the separation of output waveguides

As formulated in the MPA method, the length of a 1xN MMI structure depends on its width. The MMI width in turn depends on the number of output ports and the separation between two adjacent ones. This separation must be large enough to assure no

evanescent cross coupling between them. For example, the rib output waveguides for a SOI MMI waveguide need a large separation between them since they have wide mode underneath. As a result, although the rib waveguide has low scattering loss due to minimal interaction with the sidewall, a 1x 2 SOI MMI has 50 μm width and millimeter length[25].

If the output waveguides have well confined mode, the optical lithography and etch resolution may determine the waveguide separation. For example, Lim D. had not succeeded in fabrication of compact MMI structures based on silicon channel waveguide because the separation of output waveguides is not well defined. The dimension of a square silicon channel waveguide is 0.5 μm x0.5 μm. For a 1x8 MMI with 8 μm width, the edge-to-edge separation is 0.5 μm. With conventional optical lithography available at MIT, the gap between the output ports could not be well defined as seen in Figure IV-2[26]. Therefore the power output at each port could not be calculated.

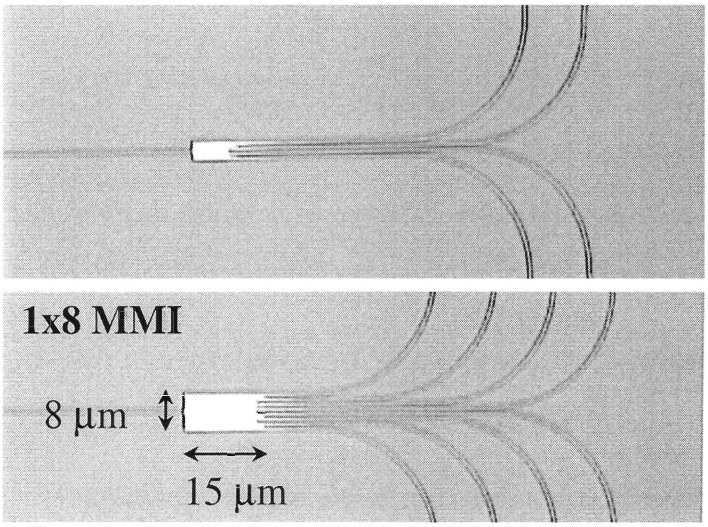

Figure IV-2. Silicon multi-mode interferometers based on channel waveguide was fabricated by D. Lim. Limitation in optical lithography resulted in output ports not being able to define well. The power output measurement is no longer accurate.

The silicon-rich Si_xN_y output waveguides that we propose for the MMI design is rectangular with a 0.8 μm width and 0.3 μm high. The high index contrast with the cladding, Δn=1.2 for ridge structures and Δn=0.75 for channel structures, results in well confined fundamental mode. From FDTD simulations results, evanescent coupling at 1550nm was no longer observed for waveguides with 0.6 μm or larger edge-to-edge separation. As a result, for our proposed 1x4 MMI structures, the widths are 7 μm and larger. For the 1x8 MMI structures, the minimum width is 15 μm. The output ports of all our MMI structures have at least 0.8 μm edge-to-edge separation. This separation can also be well defined by the optical lithography and etching tools available to us.

4.4. Length design for Si_xN_y 1x4 and 1x8 MMI via MPA formulations and FDTD simulations.

We designed the MMI structures for two waveguide configurations: the ridge structure and the channel structure. The MMI design principles are the same for both configurations. The cross sections of the designs are drawn in the Figure IV-3 below. The waveguide dimension is 0.8 μm x 0.3 μm which satisfies single mode condition for index of 2.20 at 1550 nm light. The effective index n_{eff} of our proposed silicon–rich Si_xN_y MMI structures were calculated by Apollo Photonics™ software. The 0.3 μm thick ridge structure has an effective index of 1.59. For the channel structures with oxide cladding of the same physical dimension, the

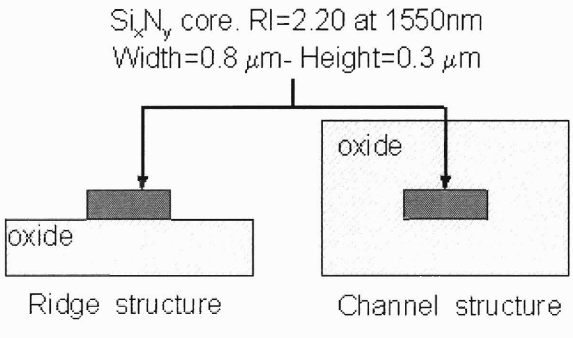

effective index is 1.68.

Figure IV-3. (Previous page) Cross sectional dimensions of the ridge and channel waveguides used as input and output ports of MMI structures.

For slab propagation of wavelength λ_0 =1550nm in MMI structures of step index n_{eff}, the distances at which an *N*-fold image is generated are reported as a function with length using MPA method in the below table.

	w [μm]	n_{eff}	MPA- based	
			1st distance for N-fold image	**2nd distance**
1 x4 MMI	7	1.59	12.6	25.1
	8		16.4	32.8
	10		25.6	51.3
1x 8 MMI	15	1.59	28.9	57.7
	18		41.5	83.1

Table IV-1: Optimal lengths at which N-fold images are generated for 1xN MMI coupler (N=4, 8). The results are obtained from mode propagation analysis and FDTD simulations.

Due to limitation of computing power, we only performed 2D FDTD analysis on out MMI structures using EIM. The FDTD results for length at which an N-fold image is generated are very similar to those yielded from calculations based on MPA method. For example, a channel 1x4 MMI of si-rich Si_xN_y with w=10 μm yield highest output uniformity at optimal length of 27.5 μm based on MPA calculation. In Figure IV-4, the FDTD output for light propagating in a MMI structure of w=10 μm and L=28 μm also shows high uniformity.

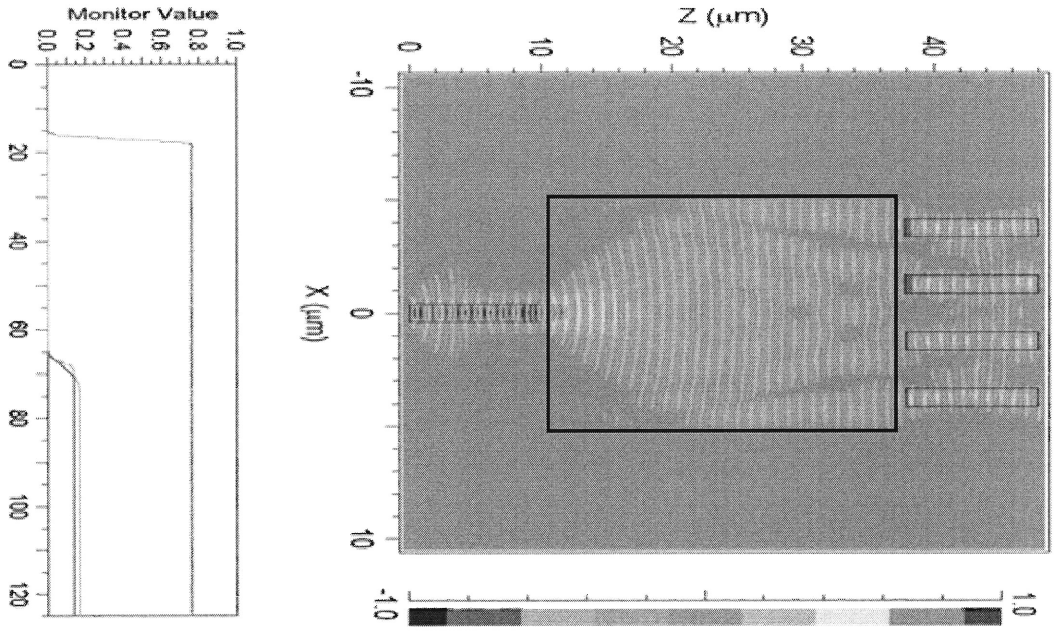

Figure IV-4. FDTD simulation results show equal output light distribution in a Si_xN_y 1x4 MMI structure. The simulated MMI is a channel structure of w=10 μm and L=28 μm.

4.5. Design of S-bend

The silicon-based MMI structure pictured in Figure IV-2 have its output ports bend at different radii from the end of the MMI for array waveguide applications. The output powers would be measured on the sides of the chip. As a result, each MMI device must be measured separately. In addition, we need to increase the separation of the output ports exiting MMI's end facet to measure power output of each port with our optical bench setup. S-bend waveguides are therefore utilized to guide light from the output ports of our proposed MMI structures to the end of the die.

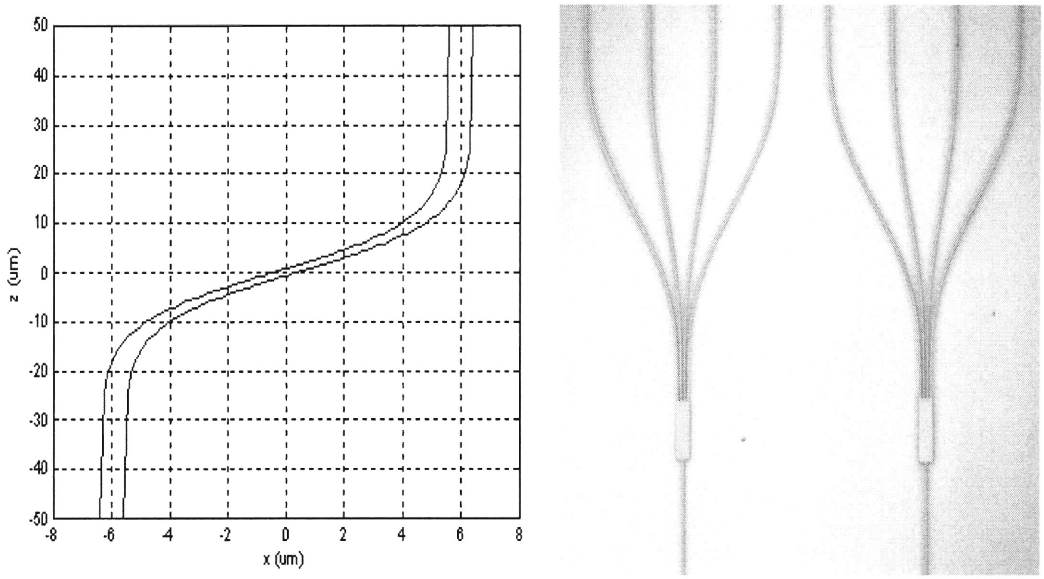

Figure IV-5. (Left) Schematic design for a slowly variation S-bend of w=12 μm and L=100 μm. (Right) Different S-bend waveguides were fabricated to guide light from the 1x4 MMI outputs

The radiation loss for light propagating in a slowly variation S-bend is low because there is no abrupt change in direction[27, 28]. Sin(x), cosine(x) and high order polynomial functions are good candidates for a low loss S-bend. We propose an S-bend design that adopts the form of a 7^{th} order polynomial function $Y= AX^7 + BX^5 + CX^3 + DX$. To calculate the coefficients, we use 4 boundary conditions. The 1^{st} boundary condition is the empirical function is Y=1 when X=1. The 2^{nd} condition is the slope at bond ends is infinitive. The other two conditions are related to the width and length of the S-bend. Figure IV-5 is the schematic of an S-bend design for a 0.8 μm waveguide. The width of the S-bend is 12 μm and length equals 100 μm. On the right is the realization of the S-bend waveguides in our fabricated MMI structures. At the output facet of the die, the separation between ridge output waveguides is 24 μm.

Chapter 5: Fabrication Process and Measurement Results for the Multimode Interference Couplers

5.1. Fabrication process for MMI structures

The core material for the MMI and waveguides of input and output ports is silicon-rich nitride (Si_xN_y) that we had developed and reported in chapter 3. The film index measured at 1550 nm is 2.20. We studied MMI structures with air and oxide cladding. The core of the structures was formed by CVD processes. The substrate is 6-in silicon wafer oxidized to form a 3 μm thermal oxide film. Since the thermal oxide has very low surface roughness, light scattering at the interface of the device and cladding is minimized.

The Si_xN_y core of ridge MMI structures was deposited by LPCVD at 725°C. The measured film thickness is 0.3 μm. The MMI structures were patterned by a 0.3-μm thick silicon mask and etched at high plasma power in the clean room facility of Lincoln Lab. The silicon mask remain was removed by TMAH solution after the nitride etch is completed. The width of their ridge waveguide is 0.8 μm. The patterning of these ridge structures had been completed by Steve Spector from Lincoln Lab.

For the channel structures, the Si_xN_y film was deposited by PECVD with SiH_4/N_2 precursors at 400°C. The deposition conditions are: p=3.0 torr, power=440 W, SiH_4= 140 sccm; N_2=4900 sccm. The film is 0.30 μm thick and has index of 2.19 measured at 1550nm. The wafer was patterned with a 0.25-μm thick silicon mask and etched with CHF_3 plasma power. The silicon mask was subsequently removed by He/Cl_2 plasma

etching after the Si_xN_y etch process had been completed. 3 μm of silicon oxide PECVD is grown as an upper clad. Most MMI structures on the masks have waveguides of 0.8 μm width. Few others have waveguides of width 0.6 μm. Both wafers were then cleaved into chips of 5 mm wide for optical measurements.

For our structures with Si_xN_y core, the output ports' separation is 0.8 μm and larger. The optical stepper lithography defined the separation well as observed from the top view of ridge MMI's in Figure V-1 below.

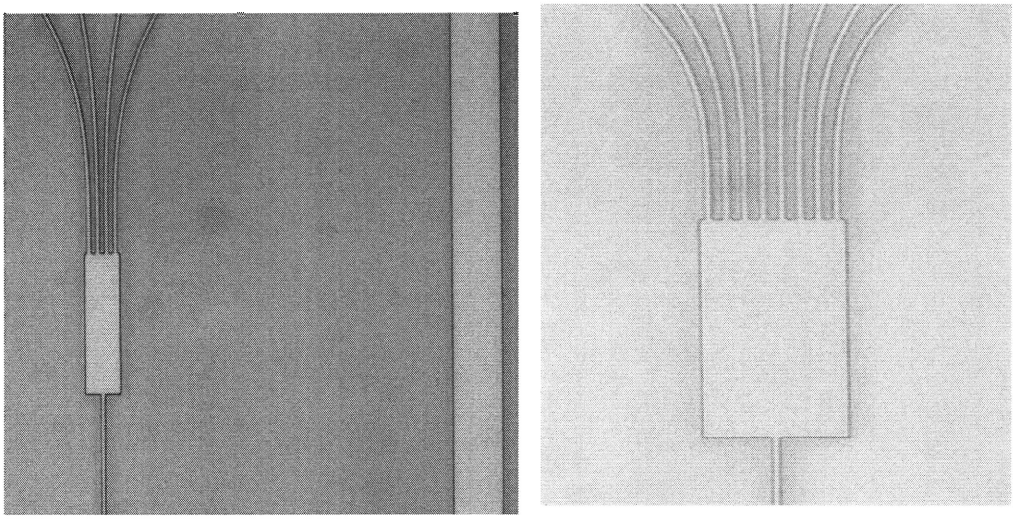

(A) 1x4 MMI w=7 μm; L= 19 μm. (B) 1x8 MMI w= 15 μm; L= 49 μm

Figure V-1. The top views of fabricated 1x4 and 1x8 MMI ridge structures show that output waveguide ports are well defined at minimum separation of 0.8 μm.

5.2. Measurements setup for the near fields of the MMI's output

5.2.3. Near-field measurement setup

The first requirement for good MMI performance is the uniform distribution of power exiting from the output waveguides. One method of measuring the uniformity is via the near-field output light intensity.

In our experiment, a lens-tipped fiber with a mode field diameter of 2 μm was used to guide the 1550 nm light into the waveguide of the input port. The exiting light was collected through a focusing lens to the Vdicon detector of an Electrophysics IR camera. The lens' magnification of either 10 or 25 was used in order to simultaneously capture all output beams in one detector area. A Scion LG-3 frame grabber stores the output signals of the detector in gray scale for further analysis. The power uniformity would then be calculated accurately by analyzing the intensities of beams impinging on the detector.

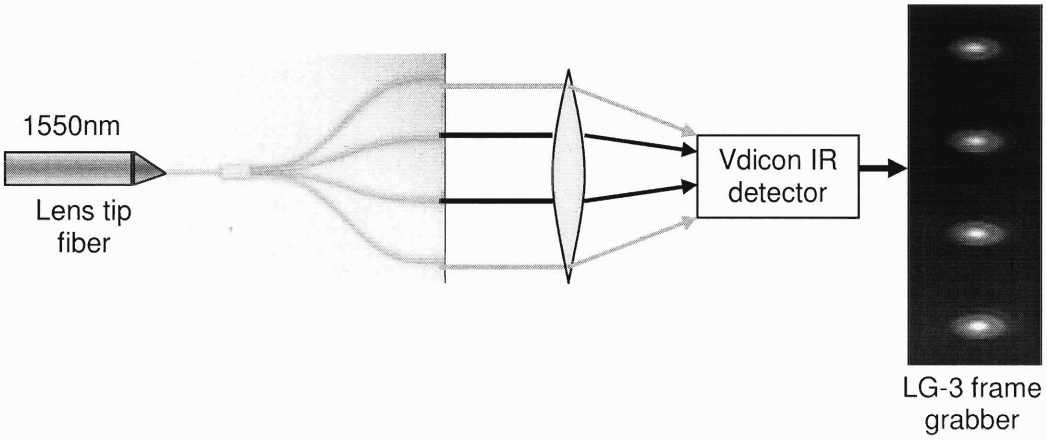

Figure V-2. Schematic of the optical bench setup for near-field output measurements. Power uniformity is calculated by comparing the gray-scale intensities of output beams.

If necessary, attenuators were used to prevent saturation of output intensity. The Vdicon detector stores the illumination of each pixel on a gray scale with 0 as the darkest while 255 white as the highest illumination. For example Figure V-3 illustrates the difference in outputs from a 1x4 MMI when an attenuator is used. Without the attenuator, all the beam spots are saturated and power intensity on the gray scale cannot be calculated. If an attenuator of OD 3.3 is applied, the signals are reduced to below 255. Power output through each MMI port can be compared through the non-saturated gray scale intensities.

Figure V-3. Optical attenuator of 3.3 OD was used to avoid saturation of the detector with input light from a 1x4 MMI.

(A) No attenuator

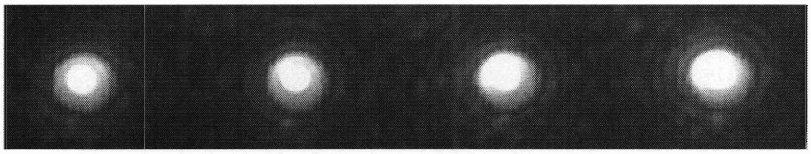

(B) A 3.3-OD attenuator placed in front of detector

5.2.4. Characterization of the Vdicon detector

a) Gamma values χ of the detector

The results that we obtain from the Scion LG-3 frame grabber are the signal outputs from the IR detector. We have to convert the detector signal into the power of the light incident on the detector via gamma χ, a light transfer characteristic of an IR detector. Gamma is obtained by plotting the log of incident beam power with respect to the log of detector intensity output. The representative equation is

$$\left[\frac{I_2}{I_1}\right]^{gamma} = \left[\frac{Ds_2}{Ds_1}\right]$$ Where I is the input beam power, and Ds is the output detector signal. For the Vdicon detector that we used, the gamma value is 0.7.

b) Adjusting for different responses in the sensing field of the detector

Parallel light beams coming from different output ports are captured at different horizontal locations on the mesa of the IR detector. A perfect detector will have the same responsivity from left to right. However, we observed that when we moved the same light beam horizontally across our Vdicon detector, the illumination registered on the right field is higher than the one on the left field as seen in Figure V-4 below.

Plot of light beam intensity with respect to horizontal position was plotted and its sloped was obtained. We need to use the value of this slope to correct for the power variation with separation between the beam spots.

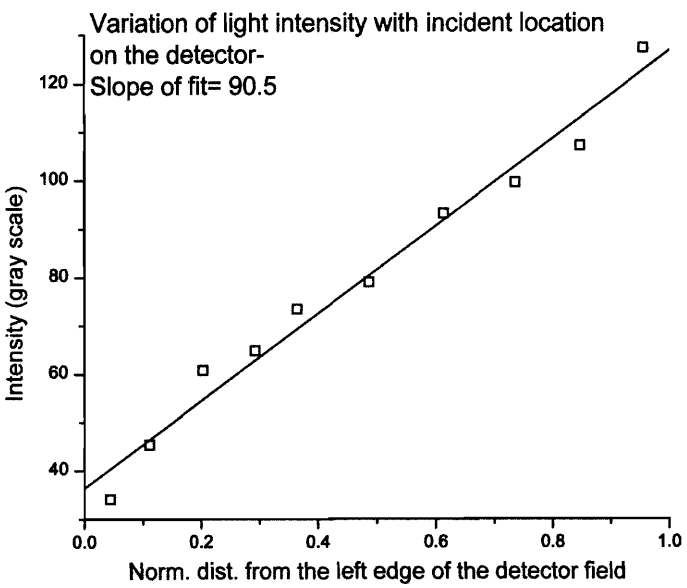

Figure V-4. Variation of the light intensity with respect to the distance from the detector left edge. As observed in the above (A) figures, the detector responsitivity increases from left to right. To accurately compare the intensity between output beams, the location-dependent of responsivity must be accounted for.

5.3. Near field output results and Analysis

5.3.1. Near field outputs for 1x4 ridge MMI structures

a) Length of MMI structures that produce most uniform power output

For the 1x4 MMI ridge configurations, we designed the structures at three widths: 7 μm, 8 μm, and 10 μm. In each set, the structures have the same width but various lengths. We measured the illumination output to the IR detector from these structures and selected the devices that yield the most uniform output. These optimal MMI structures are compared to the design parameters calculated from the MPA method. The results are displayed in the below table.

MMI *w* [μm]	n_{eff}	MPA- based		Experimentally optimized distance
		1st distance for 4-fold image	2nd distance	
7	1.59	12.6	25.1	25
8	1.59	16.4	32.8	32
10	1.59	25.6	51.3	52

Table V-1: Comparison of MMI lengths that experimentally yield uniform output distribution with results calculated by mode propagation analysis is shown. The values for 1x4 MMI structures match well at 3 device's widths.

For example, 1x4 MMI devices of width w= 7 μm and length L=25 μm, the output power ratio between two non-symmetrical ports, an outside and an inside port, is **1.05 ± 0.05**. The power at each port as a fraction of the total output power from this MMI is presented in Figure V-5a. The outputs of 4 ports are very near to the uniform condition of 0.25 for each. A near field output of one MMI structure is presented in Figure V-5b. The intensities of four beams, after adjusting for the responsitivity of the detector, are similar.

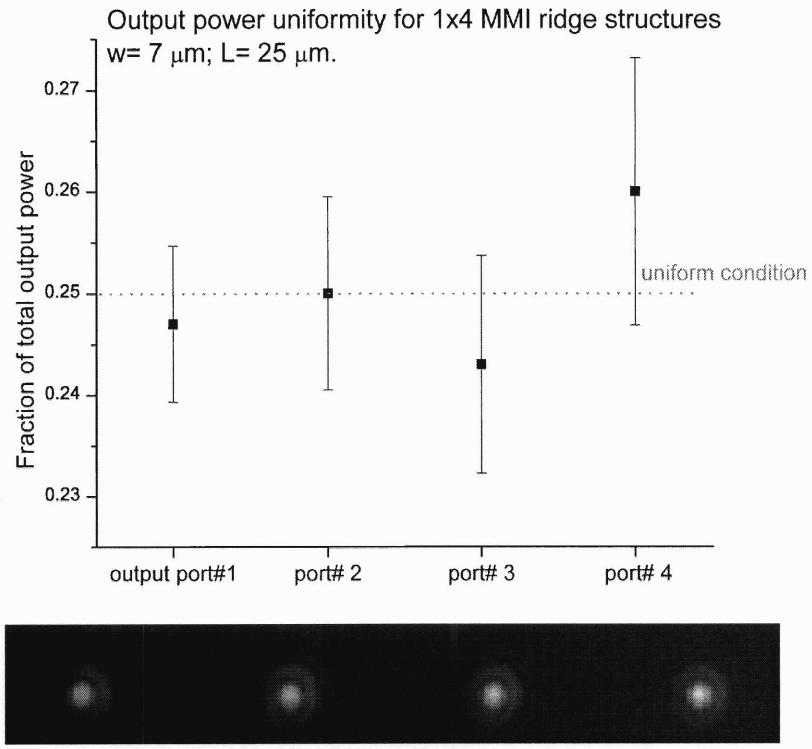

Figure V-5. (A) The output power uniformity at the ports of 1x4 MMIs with w=7 μm at optimal length 25 μm. (B) Near-field output of one such MMI structure shows beam power uniformity at 4 ports.

We also achieved good output power uniformity for 1x4 MMI devices of widths 8 μm and 10 μm at optimal lengths. For structures of w= 8 μm, the structure that has best power uniformity across the 4 ports is 32 μm long. The measured power ratio between outside and inside ports is **1.03 ± 0.08**. For 1x4 MMI devices of w= 10 μm and L=52 μm, the power is also very uniform. Its experimentally measured output power ratio is **1.02 ± 0.04.** Figure V-6 shows the near field outputs of 1x4 MMI structures that have the optimized designs that we discussed above.

(A) W=8 μm and L= 32 μm

(B) W=10 μm and L= 52 μm

Figure V-6. Near field output of 1x4 MMI ridge structures at w=8, 10 μm with silicon-rich Si_xN_y core. The outputs are uniform across the 4 ports.

b) *Variation of output power uniformity with device length*

For 1x4 MMI structures of w=7 μm, we also measured devices in which a 4-fold image is not generated at the end. Their near-field output and the output power ratios are described in Figure V-7. We observed a very high output power non-uniformity for MMI structure of length L=19 μm. For this device, the power transmitted through the outside ports is much higher than those through the two center ones as observed in the near field output.

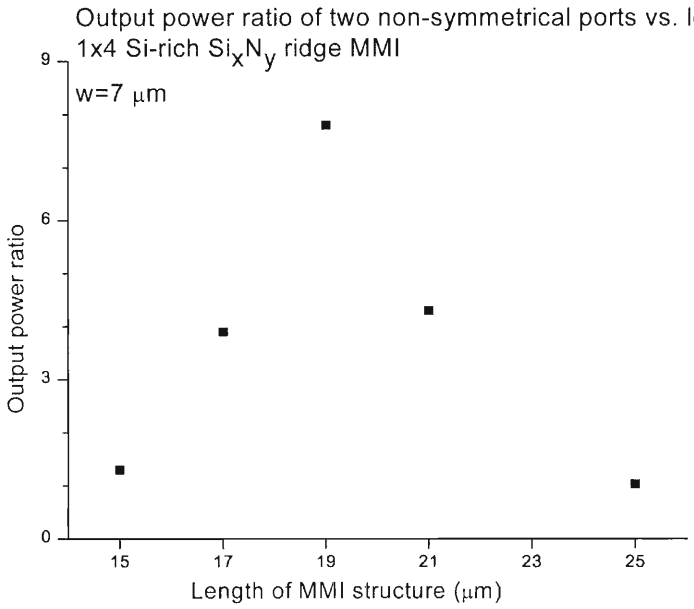

(B) 1x 4 MMI w= 7 μm and L=15 μm

Figure V-7. (A.)Variation of output power ratio with length for 1x4 MMI structure of w=7 μm. Lowest uniformity was measured on device with length L=19 μm. (B) Near field output for MMI structures with length 15-21 μm shows variation in power distributions.

L=17 μm

L=19 μm

L=21 μm

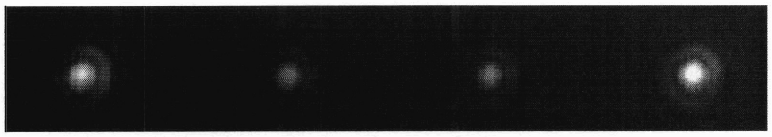

The equations in the MPA method can only calculate the distance at which a 1xN image is generated so that a MMI structure with N outputs can be designed optimally. However, the MPA method cannot describe accurately the non-uniform power distribution when the length is not optimized. 2D FDTD simulations using effective index were used to investigate the wave propagation in MMI structures at various length. Figure V-8 displays the wave propagation in a 19 μm 1x4 MMI brought up in the above discussion.

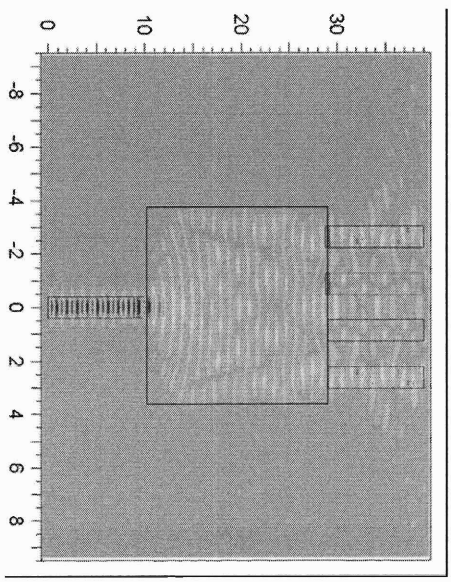

Figure V-8. FDTD simulation results for 1x4 MMI of w=7 μm and L=19 μm show non-uniform power distribution.

5.3.2. Near field output for 1x8 ridge MMI structures

1x8 MMI ridge structures had also been fabricated on the same chip with the above 1x4 MMI's. The width of their input and output waveguides is also 0.8 μm. MMI structures at two different widths w=15 μm, and 18 μm are designed and their near-field measured using the Vdicon IR detector. We have obtained good power uniformity on structures whose lengths are close to the values provided by MPA calculations based on the MPA method as seen in the table below.

w [μm]	n_{eff}	1st distance for 8-fold image	2nd distance	Experimentally optimized distance
15	1.59	28.9	57.7	55
18	1.59	41.5	83.1	82

Table V-2. Comparison of lengths that experimentally yield uniform output distribution with results calculated by MPA for 1x8 MMI.

A problem that we encountered was that the IR detector could no longer capture the whole output optical field of 8 output ports at a same time a focus lens of 25x was used. We found two solutions for this problem. The first solution is to use the same focus lens to capture the near field output of port number 1 to 6. Then, the lens is moved laterally to capture those of ports 3-8. Due to the symmetrical nature of the MMI structures, accurate output uniformity can be calculated. The second solution is to use a focus lens with smaller magnification to capture the whole field. A lens with 10x magnification was used. Both these experimental methods in capturing near-field outputs gave us same results.

For 1x8 MMI's of w= 15 μm, at length of 55 μm, we achieve good uniformity on the two outermost ports. However, the centered ports produce very low output power as observed in the near field output of port number 1 to 6 acquired through a 25x lens.

For a 1x8 MMI structure with w= 18 μm and L=82 μm, the power fraction of the output ports are closer to the uniformity value to 0.125. The near field output of all 8 ports is shown below in Figure V-9 using a 10x focus lens. The power uniformity of the output ports was calculated.

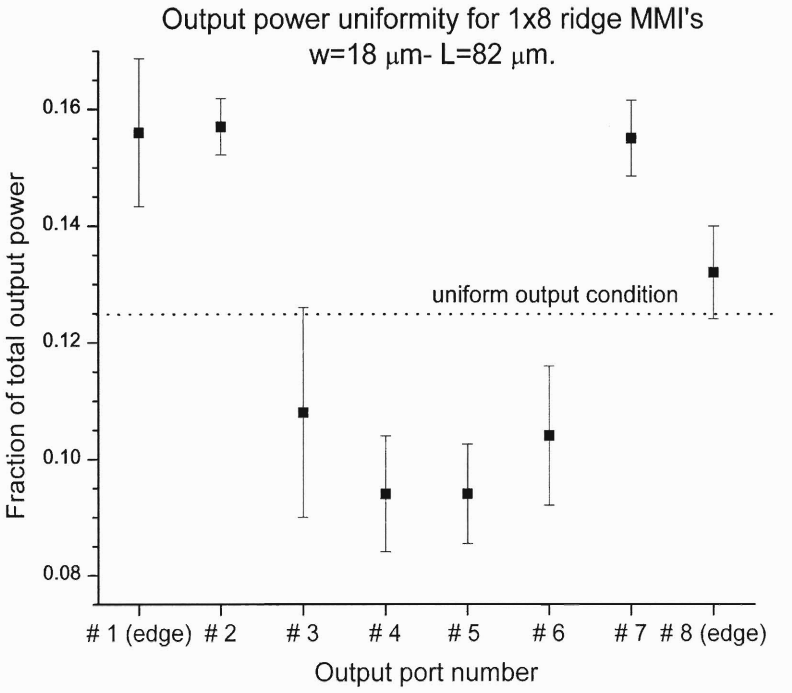

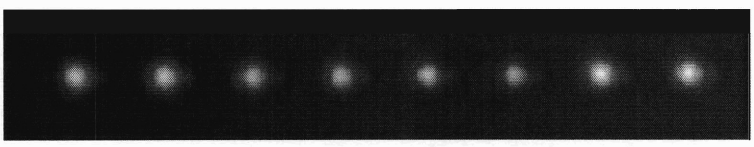

Figure V-9. (A)Uniform power output distribution of 1x8 MMI structures of w=18 μm and L=82 μm. (B) Near field output of all 8 ports for the one such MMI structure.

5.4. Measuring the power throughput of MMI structures

5.4.1. Design of MMI couplers based on channel Si_xN_y waveguide

The objective of this study is to understand the variation of efficiency of a MMI coupler with respect to the geometry of its structure. Since the length of the MMI structure depends on its width to have uniform output power distribution, the two independent variables that we investigated are the width and the height of the MMI structure

In order to understand the effect of MMI height to the power throughput, 3D FDTD simulations are required. Due to our limitations in computing power, we only investigated the efficiency with respect to the width of the device. As a result, we design channel-based MMI's at thickness of d= 0.3 μm. Two MMIs at very different widths were designed. The widths and heights of the 1x4 MMI tested structures are listed in the table below.

	Effective index (N_{eff})	MMI width (μm)	Length (μm) that yields 1st 1x4 image
1x4 MMI- d= 0.30 μm	1.68	W= 10 μm	27.5
		W= 18 μm	88

Table V-3: MPA-based calculations of distances that yield uniform output distribution with for 1x4 channel MMI.

The input and output channel waveguides have silicon-rich Si_xN_y core (RI=2.20) with oxide cladding. Their cross section dimensions are 0.8 μm width x 0.3 μm height.

5.4.2. Measurement setup for direct power measurement at output ports

We had calculated the power distribution of MMI structures by measuring their near field output via the illumination on an IR Vdicon detector. We can compare the power of two beams by the ratio of their intensities in gray scale. However, calibrating the beam power from the gray-scale intensities of the detector is not accurate because we do not know precisely the light reflection and attenuation through the components of the measurement systems such as the focus lens, re-directing mirrors and attenuating lens.

Therefore, to accurately calculate the throughput power of a MMI structure, we need to use direct power measurement system such as the Newport Auto Aligner station. The schematic setup for such a station is illustrated in Figure V-10. Light at 1550nm is guided from the laser source to the input facet and from the output facet to the power meter by single mode waveguides. The fiber placement with respect to the waveguide is optimized in all three directions to yield the highest throughput power.

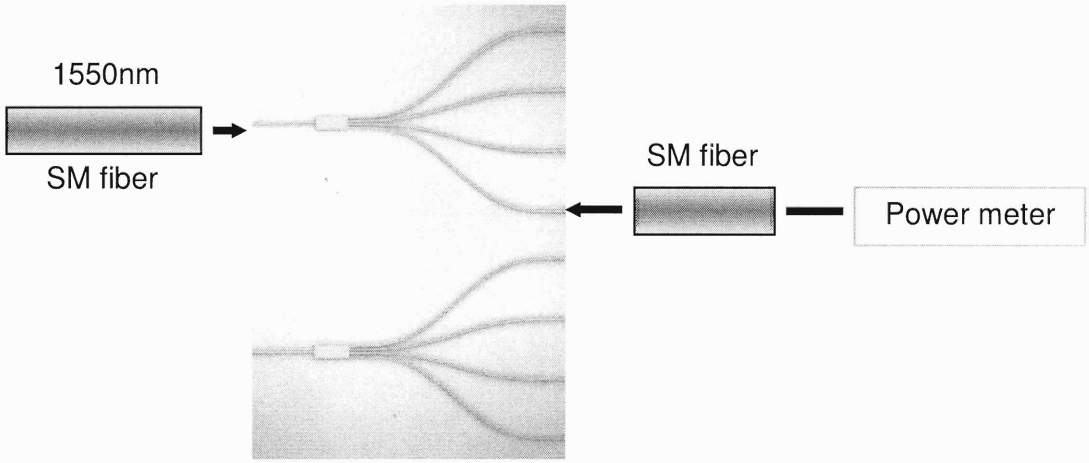

Figure V-10. Schematic of the optical bench setup for direct output power measurements is shown. Sum of power transmitted in 4 ports are compared with throughput power of a single-mode straight waveguide on the same chip.

The coupling efficiency of a MMI device is obtained from the ratio of total power exiting all its output waveguides over the throughput power of a straight waveguide on the same chip. We performed throughput power measurements on channel-based structures since their waveguides have smaller propagation loss compared to the ridge structures. Lower propagation results in higher power measured at end of the device.

5.4.3. Output uniformity of MMI measured by direct output power

The length of a MMI structure that yields highest power uniformity is designed with the MPA method and 2D FDTD simulations with effective index as presented in chapter 4. We tested the fabricated 1x4 MMI structures at 1550nm wavelength on the Newport Auto Aligner station. Nufern980 cleaved fibers with a mode field diameter of 6.8 μm were used. Once the input position to the input waveguide was optimized, we could scan another fiber along the output waveguide facet for direct power measurement. Index matching fluid was used at the input facet to enhance coupling efficiency with the input waveguide. We achieve high output uniformity for structures of w=10 μm and 18 μm at respective lengths similar to the theoretical results as seen in the output scans of figures V-11 and V-12. The output waveguides are positioned 20 μm apart at the output facets by using S-bends.

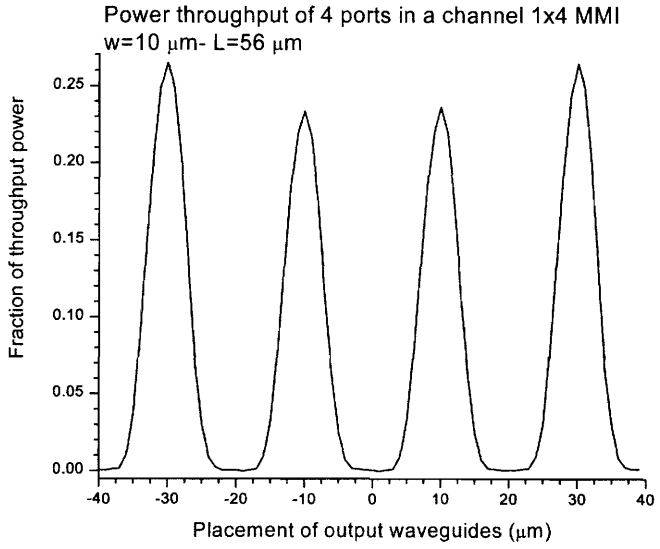

Figure V-11. Normalization of measured throughput power of 4 output waveguides for a Si_xN_y MMI coupler of w=10 μm and L=56 μm. Good output uniformity is achieved

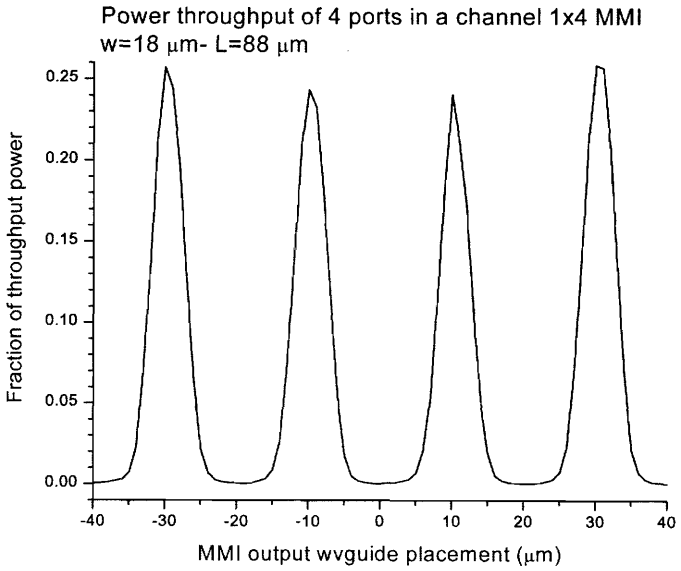

Figure V-12. Similarly good power output uniformity was measured for a Si_xN_y MMI coupler of w=18 μm and L=88 μm. Output power scan were done on the Newport Auto Aligner station.

With both near field output analysis and direct power measurements, we had experimentally validated the method of combining the effective index and mode propagation analysis proposed by Soldano to design MMI lengths that yield highest uniformity.

5.4.4. Coupling efficiency measurement results and analysis

a) Dependence of power throughput with device width for 1x4 MMI

The sums of power throughput at 4 ports were compared for MMI structures of two widths, w=10 μm and w=18 μm. Their lengths are respective 28 μm and 88 μm, which are the first distances in each structure that an *N*-fold image is generated. As observed in Figure V-13, in MMI coupler of w=10 μm and L=28 μm, the output power equals to **0.80 ± 0.05** of the power guided through a straight waveguide of the same length. At larger MMI width w=18 μm, the measured throughput power is reduced to **0.64 ± 0.06**.

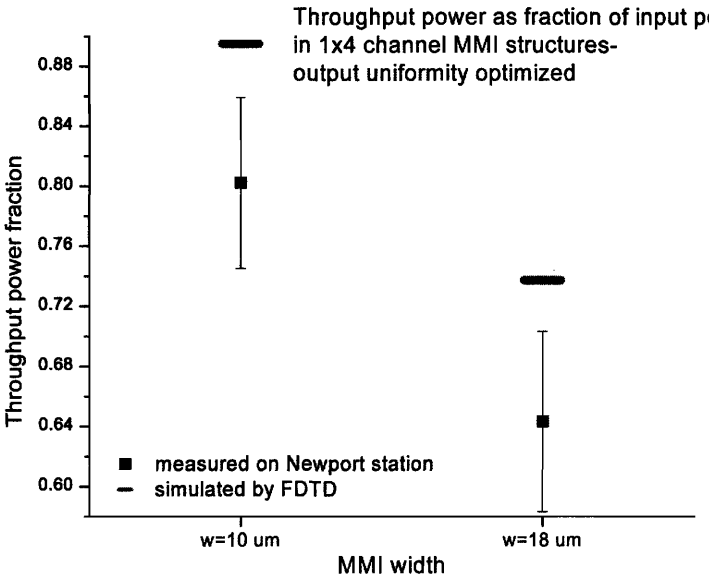

Figure V-13. Measured and FDTD simulated coupling efficiencies for 1x4 MMI couplers with respect to its width. The lengths of the devices are optimized to yield uniform output. We achieved a 0.80 coupling efficiency for a compact structure of w=10 μm and L=28 μm.

$$E(y,z) = \sum_{m=0}^{M} a_m U_m(y) * e^{(-j\beta_m z)}$$

$$U_m(y) = \sqrt{\frac{2}{W}} * \cos(\frac{m\pi y}{W})$$

Output power is reduced at larger MMI width because the amplitudes $U_m(y)$ of the propagating modes in the structure are smaller. In simplest form, the electric field E (y,z) in a multi-mode waveguide where only symmetrical modes are excited, can be

expressed as a sum of all M modes as in the equation above. W is the width of the MMI where β_m is the propagation constant. Z is the propagation direction where Y is the lateral direction.

Since we have the same input power, normalization conditions requires the mode to be more spread out at larger width W. As a result, the amplitude of $U_m(y)$ is smaller and produces smaller overlap with the output waveguides of same dimensions. The output power at each port is therefore smaller. The trend in measurement data are confirmed by the FDTD simulation results.

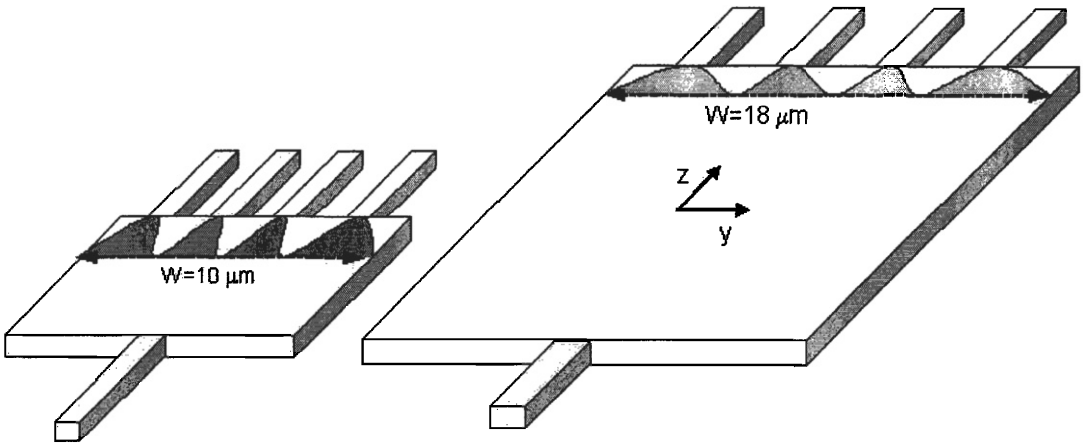

Figure V-14. Schematic drawings of MMI couplers having different width and the waveforms at the exiting facets demonstrate the lower coupling efficiency at larger width.

The measured data is smaller than the results from FDTD simulations of each width probably because of the sidewall scattering loss of the fabricated structures. The FDTD simulations only account for the power loss due to overlap mismatch between the *N*-fold images in the MMI structure and the output waveguides.

b) Dependence of power throughput with device length for 1x4 MMI

We also observed a reduction in power throughput at the 2nd length that a 4-fold image is produced. For example, in 1x4 MMI structures of w=10 μm, the measured throughput power fraction reduces to **0.34 ± 0.03** at length L=56 μm as shown in Figure V-15 (A). The reason is that the length L=56 μm is the first distance a 2 fold image is produced for MMI structure of w=10 μm as expressed by equation 4.1. Even though a two fold image can still result in equal power distribution at 4 equally spaced output ports, its peaks' lateral positions do not coincide with the location of the output ports as seen in Figure V-15 (B) below.

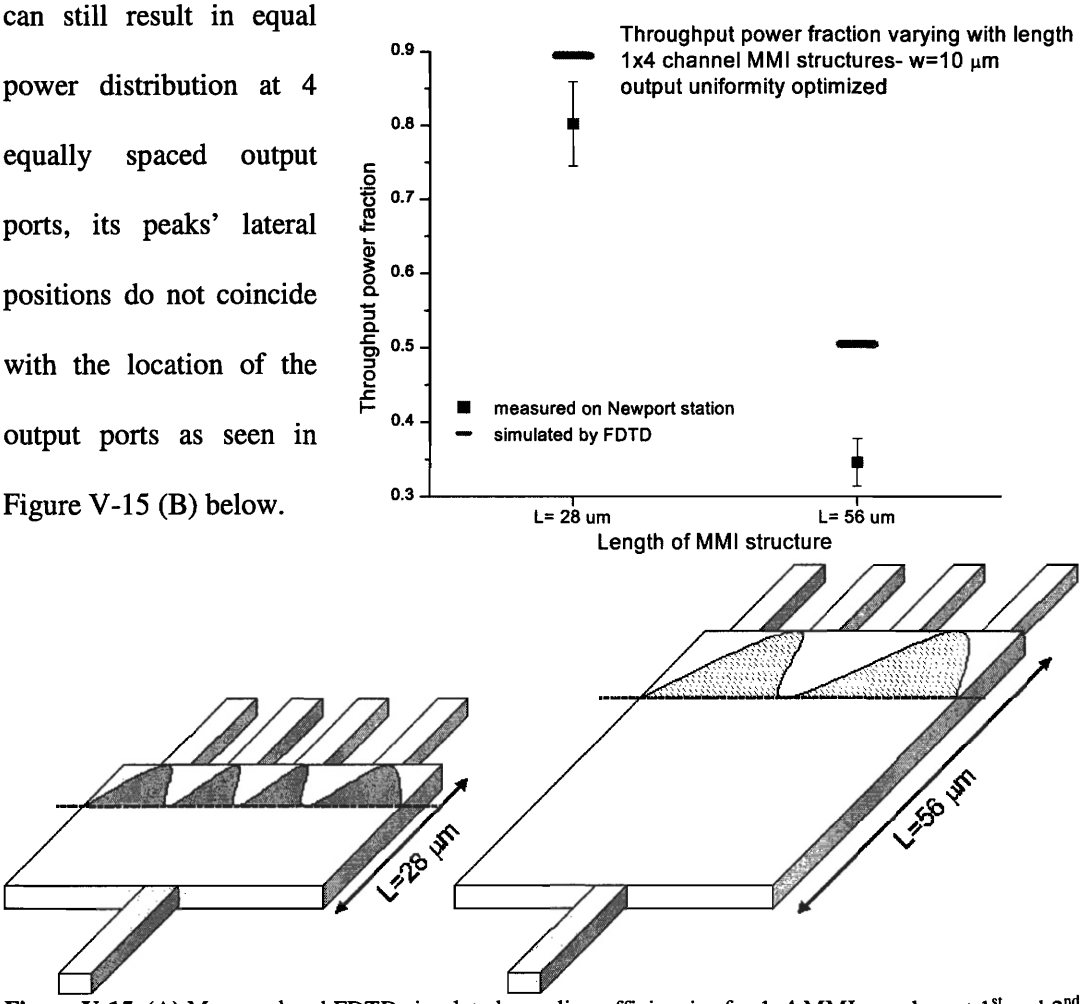

Figure V-15. (A) Measured and FDTD simulated coupling efficiencies for 1x4 MMI couplers at 1st and 2nd distances a 4-fold image is generated. (B) The reduction in coupling efficiency at longer distance can be explained by the generation of a 2-fold image.

5.5. Conclusions

We had successfully demonstrated in these two chapters the design, fabrication and characterization of multimode interference couplers, of silicon-rich silicon nitride core that yield uniform distribution of power output and higher than 80% throughput power. These 1x4 and 1x8 symmetrical multimode interference couplers are also very compact with less than 100 μm long. We can save valuable on-chip real estate with this significant reduction of the devices' area.

These structures were designed using modified calculations of 2D mode propagation analysis method with effective index. Both near-field output and direct waveguide power measurements of these MMI structures were performed to fully characterize the transmission properties of the fabricated devices. The lengths of the devices that yield uniform power output at N output waveguide is close to the theoretical value at which an N-fold image is generated. Higher coupling efficiency is achieved at smaller width although the separation of output waveguides must be considered to ensure no evanescent coupling. In the future, if we have computing power to perform 3D FDTD simulations, we can investigate the effect of device height to coupling efficiency.

Silicon-based, High Efficiency Compact Coupler from Single-Mode Fiber to Sub-micron Waveguide

A chip that has both electronics and photonics components will have performance and functionality far greater than its current electronics predecessor. As a result, silicon has rapidly become a platform on which integrated optical circuit designers seek to integrate several optical components that communicate via waveguides[29, 30]. Silicon nitride (Si_xN_y) and silicon oxynitride ($Si_xO_yN_z$) waveguides with silicon dioxide cladding are alternatives to very high index silicon systems in guiding light on a chip because they have small dimensions, low scattering loss. In addition, their material properties are well understood since they have wide applications in the semiconductor industry. However, optical fibers still guide light for chip-to-chip and board-to-board communications. As a result, optical signals from these fibers still need to be coupled to on-chip waveguides and vice versa.

Direct coupling is inefficient because of three main reasons; first is the high power-loss from reflections due to the difference in refractive index of the fiber and waveguide core materials, second is a mode-size mismatch, and third is a mode-shape mismatch between a fiber's circular and waveguide's typical elliptical modes. Direct coupling from a standard single mode SMF28 fiber (9 μm core diameter) to a single-mode $Si_xO_yN_z$ waveguide (index n = 1.70) leads to 13.5 dB insertion loss. This insertion loss is much higher than the propagation loss of that same on-chip waveguide. Minimizing the

insertion would result in smaller number of optical amplifiers to be built and free up valuable real estate on-chip.

We demonstrate in this work a very efficient fiber-to-waveguide coupling scheme with our compact couplers fabricated entirely by silicon-based processes. The fabricated devices are compact (18-20 μm long), highly efficient (2.2 dB insertion loss from a cleaved Nufern980 fiber), and its robust design can be applied for effective coupling into single mode waveguides of core indices up to 3.5. We will present simulations and measurements of coupling efficiency as a function of coupler dimensions for light coupled from a single-mode optical fiber to a single-mode $Si_xO_yN_z$ waveguide of index 1.70. Theoretically calculated values of coupling efficiency obtained using Finite-Difference Time-Domain method are compared to experimentally measured values.

Chapter 6: Sources of Loss in Fiber-to-Waveguide Coupling and Known Coupling Schemes

6.1 Sources of loss in direct fiber-to-waveguide coupling

Direct coupling is inefficient because of three main reasons. The first reason is the high power-loss from reflections due to the difference in refractive index between the fiber and waveguide core materials. For example, if there is no index matching fluid between the fiber and $Si_xO_yN_z$ waveguide (RI=1.70), the reflection loss is 0.5 dB. The second reason is a mode-size mismatch. Coupling directly from a standard Nufern980 fiber to a 0.9 μm x 0.9 μm single mode $Si_xO_yN_z$ waveguide, the radiation loss to the cladding is 12.5 dB. Last is a mode-shape mismatch between a fiber's circular and waveguide's typically elliptical fundamental modes. Since our waveguide has a square cross-section, its mode shape is close to circular. The mode shape mismatch between fiber and this waveguide is very small. For passive optical alignment, there is a loss induced by misalignment of the fiber's center to the waveguide's center.

6.1.1. Reflection loss at fiber-air-waveguide interfaces

A large index contrast between the fiber core and the waveguide leads to high reflection at their interface. Usually, the fiber core is doped silica, which has an index slightly higher than 1.46, while a waveguide is silicon or silicon dielectric ($Si_xO_yN_z$ or Si_xN_y with RI from1.5 to 2.2). The power reflection loss can be estimated by the equation

$$R = \frac{|n1 - n2|^2}{(n1 + n2)^2}$$

During measurements, we avoid placing the fiber very close to the waveguide facet because we may scratch both surfaces and induce more scattering loss. There are now two surfaces with high index contrast, fiber-air and air-waveguide. Only 90% of the light transmitted that result in a total reflection loss of 0.45 dB. A solution is to use a material which has a transitional index to fill the gap between the components. An index-matching fluid (IMF) is commonly used to fill the air gap between an optical fiber and the waveguide. For example, if an IMF of index 1.46 is used, 98% of light is transmitted and the reflection loss is reduced to 0.09 dB.

6.1.2. Coupling loss due to mode size mismatch

Mode-size mismatch is the largest source of radiation loss for fiber-to-waveguide coupling. The coupling loss between two components can be calculated from overlapping their fundamental modes' wavefunctions. The two wavefunctions can be assumed to have Gaussian profile with different beam diameters. The overlapping equation is

$$\Gamma = \frac{\int_{-\frac{W_x}{2}}^{\frac{W_x}{2}} \int_{-\frac{W_y}{2}}^{\frac{W_y}{2}} e^{-2[\frac{x^2+y^2}{w_0^2}]} dxdy}{\int_{-\infty}^{\infty} \int_{-\infty}^{\infty} e^{-2[\frac{x^2+y^2}{w_0^2}]} dxdy}$$

Direct overlapping of those two wavefunctions is small because most of the incident power is leaked into cladding. With W_0= 5 μm for an SMF28 fiber and our waveguide dimension of W_x=W_y=0.9 μm, the overlapping factor Γ equals to 0.0211. If a smaller fiber such as the Nufern980 (W_0= 3.4 μm) is used, the overlapping factor increases to 0.0435 since the light is more confined at the center.

Furthermore, coupling loss can be induced from difference in shape of the fundamental modes. The fiber has a perfectly circular fundamental mode due its core's shape. The waveguide is usually a square or rectangle. A square waveguide mode can be approximated as circular while its rectangular brother is elliptical. Since our design is for a channel waveguide with square cross-section, this loss should be very small.

6.1.3. Packaging misalignment loss

There is power loss associated with misalignment of the centers of the fiber and the waveguide. Because of the symmetrical shapes, the center lines of both the fiber and waveguide are their wavefunction's propagating axes. Since both structures have Gaussian waveforms with maximum power at center, loss arises when the center lines not aligned. The magnitude of misalignment loss depends on the separation between these lines. Active alignment by measurement system such as the Newport Auto Aligner station will minimize this loss.

Silicon v-groove has been used a solution for passive alignment between the fiber core and a planar optical component [31, 32]. The technique is based on the preferred wet etching of crystal silicon in <111> direction. By controlling the etch depth, precise alignment of the fiber core to the planar optical component is achieved. The fiber has a diameter of 80-100 μm. In order to form a deep v-groove, the challenge is to develop a silicon etching process that also has high selective with dielectric. The commonly used etching agent is KOH which will damage the facet of the $Si_xO_yN_z$ waveguide. Since we

have limited resources to do directional silicon etch in our lab, the development of a working v-groove is saved for future work.

6.2 Prior techniques for fiber-to-waveguide coupling in published literature

Various documented spot-size converter schemes are used to lower the coupling loss from fiber to waveguide. We only present here only the concepts or principles that had been realized via the fabrication of a coupling device. Many other spot-size reducing designs cannot be realized because they cannot confine the beam simultaneously in vertical and lateral directions.

One way to lower the coupling loss is for the wavefunction to not change abruptly as light propagates. Its effective index, optical impedance, boundary conditions should be maximally matched as wave propagates. An adiabatic taper is an example of a device utilizing this principle and it is realized in the form of a very long linear taper to slowly reshape the beam size from input width to smaller input width[33, 34]. The size, shape, effective index of the propagating beam is slowly changed and finally confined into the smaller structure.

A different way is using a focusing lens to yield a minimal beam width at the focal distance. Devices utilizing this concept includes a planar lens[35] or a graded index (GRIN) structure that behaves as a focusing lens. Their focusing principle is well understood[36-38] and is used for Ge-doped silica fibers and polymer optical fibers. The advantage of these designs is the ability to focus length in a very short distance. Our

calculation has shown that for a parabolic GRIN structure of index contrast Δn=0.24, the focusing length is 20 μm for 1550 nm propagating light.

6.2.1. Schemes to confine light in the vertical direction

Previous arts, prevalently graded index fiber lenses and high silica graded index stack on-chip had been used to confine the light vertically.

Shiraishi et al reported a simple method to reduce the SMF28 spot size to 5 μm utilizes a quarter-pitch length of a *graded-index fiber* (GIF)[39]. It is well known that quarter-pitch length of a GIF can be used as a collimator that expands the spot diameter from a laser light source to a single mode fiber. In this paper, the authors also demonstrated that a tip with a square-law index profile can be used as a spot size reducer.

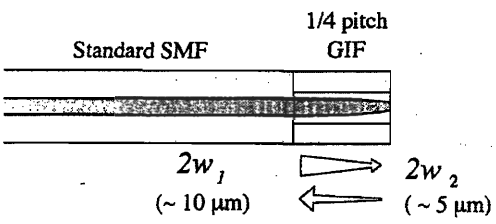

With Δ=1.93%, and a ¼ pitch GIF=71μm, the spot diameter is reduced from 10.8 μm to 5.7 μm. The coupling loss is reduced from 2.3 dB for direct coupling to 0.4 dB with the GIF. The reducer can obtain low loss coupling between single mode fiber and an optical waveguide having small spot diameter.

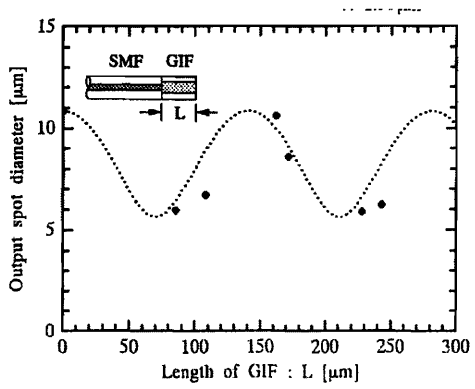

Figure VI-1. Graded index fiber to reduce spot size from Shiraishi et al is shown. Their design's limitations are large focal beam size and low error tolerance fabrication.

However, one limit of this design is the large final beam size that it is able to reduce to. In addition, the fabrication technique is unique and has small error tolerance. An etched fiber can easily be damaged and has smaller alignment tolerance than a standard larger cleaved fiber.

On the chip side, planar GRIN lens on silica has been fabricated by Beltrami et al[40]. In his paper, the author varies index around 1.44 by adjusting the amount of F doping in oxide PECVD. The periodic focusing effect of the parabolic profile is demonstrated. The main limitation of this design is the ability to control the index contrast. With F doping, the author can only achieve a maximum index of 1.47. As a result, the small index contrast leads to long focus length and large final beam width. The structure cannot focus the beam diameter of a standard fiber down to 1.0-2.0 μm. In addition, the doping profile has a large width of 20 μm. A thick structure is a hindrance to fabrication and integration of other on-chip devices.

6.2.2. Schemes to confine light in the horizontal direction

A laterally tapered waveguide for coupling out from photonic device into a single-mode fiber is a well known idea. However, there is no taper fabricated to focus light from a single mode fiber to a submicron waveguide since there is no practical method to create a vertical taper on-chip. A lateral taper alone still results in high-coupling loss.

An alternative solution is a tapered rib waveguide used in conjunction with a much bigger mesa waveguide as shown by Smith et al [41]. The light injected in the mesa below, is coupling up due to higher n and also to the tapered shape of the ridge. The device is in the

order of millimeter in length. Although, the author can demonstrate the coupling effect, there is no coupling efficiency value reported in that paper.

A novel coupling scheme that attracts attention the last couple of year is the adiabatic inversed taper[34, 39, 42-44]. An adiabatic inversed taper to couple light from had been fabricated by Shoji and Yamada to coupler light from a SM fiber to a 0.3 μm x 0.3 μm Si wire[43, 45]. Its design principle is mode enlarging at very small waveguide as demonstrated by Shani et al[46].

The silicon taper is in the order of millimeter long and the fabrication is very challenging since the tip of taper is 60nm as seen on the left. The lithography technique at this scale is e-beam writing which may not be the best tool for dense optical integration.

Figure VI-2. SEM images of inverse silicon taper fabricated by Shoji et al are shown. The limitation of their design is long millimeter device length and high requirement for accurate lithography technique.

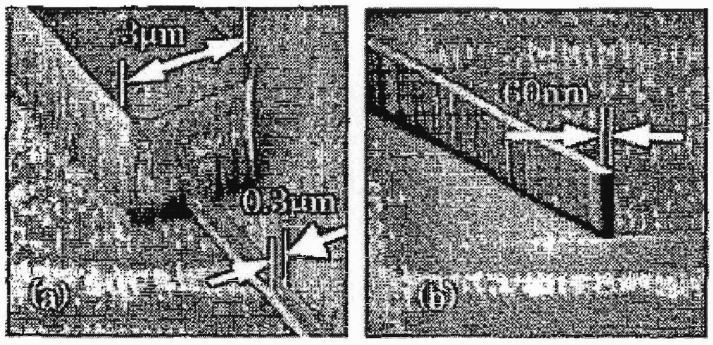

For all the previous coupling schemes reported above, confining the light into submicron waveguide was not achieved. In addition, they have stringent fabrication and lithography requirements. In contrast, we would like to introduce a design for a compact, high efficiency on-chip coupler structure that can be fabricated entirely by silicon-based

processes at the Microsystems Technology Lab (MTL) at MIT. The coupler design offers effective coupling for single mode waveguides of core indices up to 3.5. Its design will be presented in chapter 7. Fabrication processes which utilize many novel techniques are reported in chapters 8 to 10. Optical characterizations are in chapter 11.

Chapter 7: Proposed Design for a Compact, Efficient Fiber-to-Waveguide Coupler

7.1. Proposed design for the coupler

To achieve high coupling efficiency and a compact design, we utilized a tapered GRaded INdex (GRIN) structure, whose schematic is shown in Figure VII-1. The self-focusing effect for light traveling in a parabolic GRIN medium is well known and is used for Ge-doped silica fibers and for optical polymer fibers. However, the fabrication of such a circularly symmetrical GRIN profile in a planar format on a chip leads to processing complexity. Therefore, we utilized a novel coupling scheme that achieves simultaneous vertical and horizontal confinement, using an asymmetric step-wise parabolic index profile to confine light vertically[35, 47, 48] and a combination of a lens and taper to confine light horizontally[35, 48].

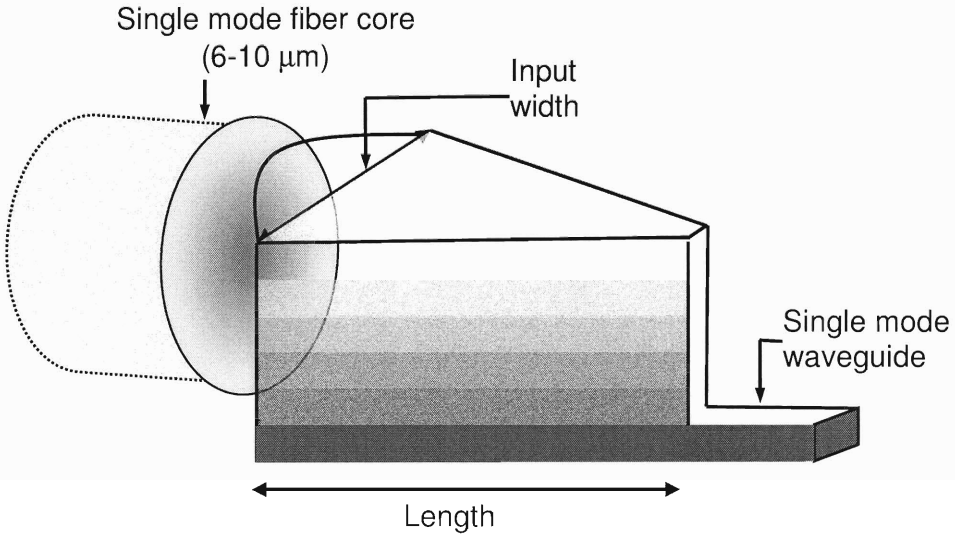

Figure VII-1. Diagram of the proposed coupling scheme from fiber to on-chip waveguide is shown. The structure simultaneously transforms the light vertically by asymmetrical GRIN and horizontally by lens & taper.

The proposed scheme can be used to couple light into any high index $Si_xO_yN_z$ and Si_xN_y waveguide because we can deposit films with index varied from 1.5 to 2.2 by PECVD. We choose to demonstrate the coupling effect to a single-mode $Si_xO_yN_z$ channel waveguide of index 1.70 because of system design issues. At 1550nm wavelength, its single mode dimension is 0.9 μm x 0.9 μm. The waveguide and the coupler are built on a 3 μm oxide under clad on silicon wafer. The waveguide is integrated into the coupler structure to eliminate a coupler-waveguide interface and its scattering loss.

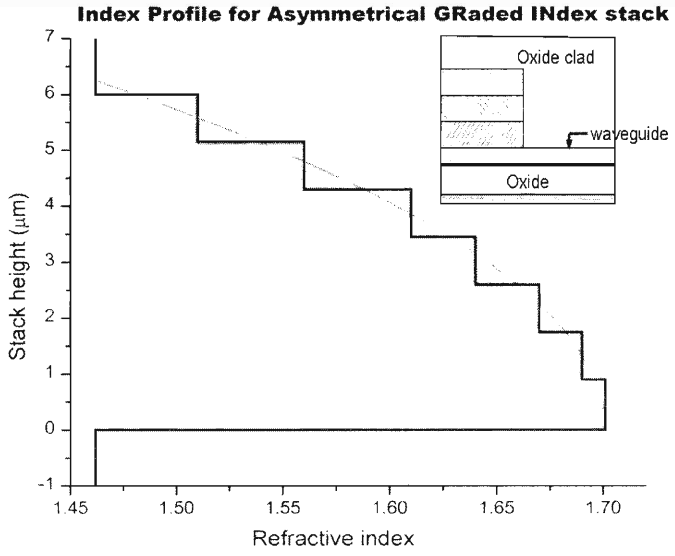

Figure VII-2. Vertical step-wise index profile of our 7-layer asymmetrical GRIN structure is illustrated. The indices follow a parabolic profile from 1.52 to 1.70 for 6 μm height.

The coupler consists of a stack of $Si_xO_yN_z$ layers. The total stack height can be scaled up to the diameter of the fiber. The index profile of our prototype is shown in Figure VII-2. The stack height is 6 μm, similar to the mode field diameter of the Nufern980 fiber. Oxide upper clad covers both coupler and waveguide structures and protect their upper surfaces.

We kept the coupler height and graded index profile constant while varying coupler's length, input width, the lens radius on our test devices. The central structure is a flat-end taper of 8 μm wide at the fiber-end and 0.9 μm at the waveguide end. The total length is 20 μm.

7.2. Design parameters and simulations

7.2.1. Graded index for vertical coupling

The proposed device will use an asymmetrical graded index to focus the spot size from 6-10 μm to under 1 μm. The propagation of a Gaussian beam in a symmetrical GRIN medium has minima and maxima of field intensity along its length. This self-focusing effect is most studied with a 2D parabolic index profile. In such medium, if the index of refraction varies along the vertical axis y as

$$n(y) = n_0 (1 - \tfrac{1}{2} \alpha^2 y^2)$$

Then, the self-focusing period of the structure is

$$d = (2p+1) * \frac{\pi}{2\alpha} \text{ [35]} \qquad \text{Where p is an integer}$$

For a symmetrical parabolic GRIN with maximum index n_0= 1.70, Δn=0.24, this calculation yields a focus length of 17 μm for 1550nm light.

For an asymmetrical GRIN structure similar to our design, we will try to obtain the numerical solution from Rsoft™ FullWave® program. FullWave utilizes the finite difference time domain (FDTD) method to calculate the field and power of the wave at a distance from the input's location. This technique is based on direct integration in time of Maxwell's equations using the Yee mesh[49]. The FDTD simulations for this 3D

coupler were accomplished by using the effective index method to collapse the 3-dimensional structure into 2D FDTD simulations. The first simulation calculates the coupling efficiencies of the vertically asymmetrical GRIN structure. The second simulation calculates the efficiency of the non-adiabatically linear taper in the horizontal plane. A value for 3D coupling efficiency is obtained as a product of these 2D coupling efficiencies.

Trisha Montalbo reported the simulations in her M. S. thesis[48]. She also confirmed the FDTD results with simulations utilizing beam propagation (BPM) method for 3D structures. Both methods show similar variation effect, although the values yielded by BPM are 0.05 to 0.1 lower. Since the slowly varying field approximation of BPM places restriction on the index contrast between adjacent layers, their results may not be as accurate as those of FDTD simulations.

The 2D simulations of an asymmetrical GRIN show a maximum coupling efficiency of 0.94 at length of 19.5 μm for input fiber with a 6 μm MFD. If a Nufern980 fiber with a larger MFD of 6.8 μm is used, the maximum efficiency is 0.82 as seen in Figure VII-3.

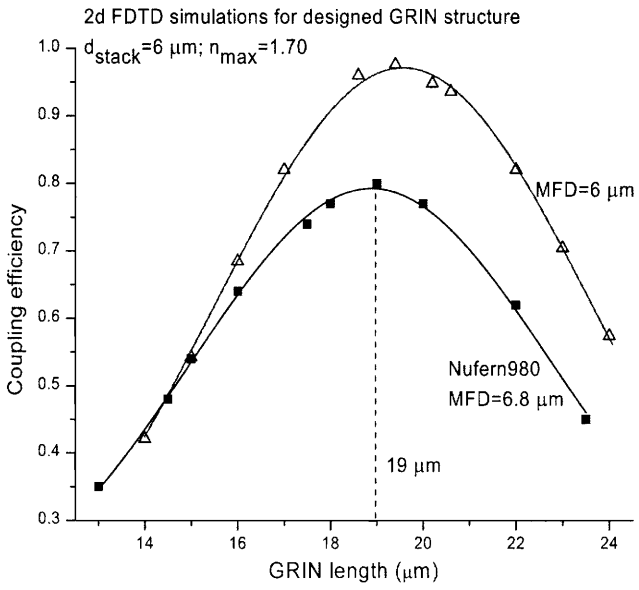

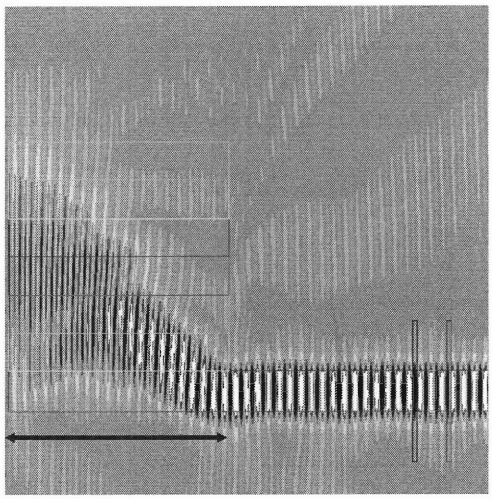

Figure VII-3. 2D FDTD simulation results for the proposed asymmetrical GRIN shows self-focusing effect and also high coupling efficiency at L=19 μm.

7.2.2. Lens and non-adiabatic taper for lateral coupling

Because a lateral variation of the refractive index is difficult to fabricate, the guiding structures in the horizontal plane are a non-adiabatic taper and a planar lens at the fiber input facet. The taper length is matched with the GRIN's focus length, which is 20 μm or 60 μm. The taper's shape and the lens radius are the variables that affect coupling efficiency in the horizontal direction.

The taper would have an input width at 8-10 μm, close to the diameter of the guided mode of the fiber. Then the width is tapered down to that of the waveguide. At L=20 μm, light propagation in the taper does not comply with adiabatic conditions. However, FDTD simulations show an already high coupling efficiency of 0.82 from Nufern980 fiber. Lower the radiation loss at the coupler-cladding interface is obtained at smaller angle. At taper length of 60 μm, the efficiency is higher at 0.84.

The effect of the lens radius was also studied for taper at L=20 μm. We came to the same conclusion that Dr. Manolatou had mentioned in her thesis that the lens marginally increases the coupling efficiency as seen in Figure VIII-4[35].

Figure VII-4. 2D FDTD simulation results for a tapered lens shows high coupling efficiency for input width w=8 μm. The FDTD output power chart reveals most of the guided mode of the fiber is confined into the waveguide.

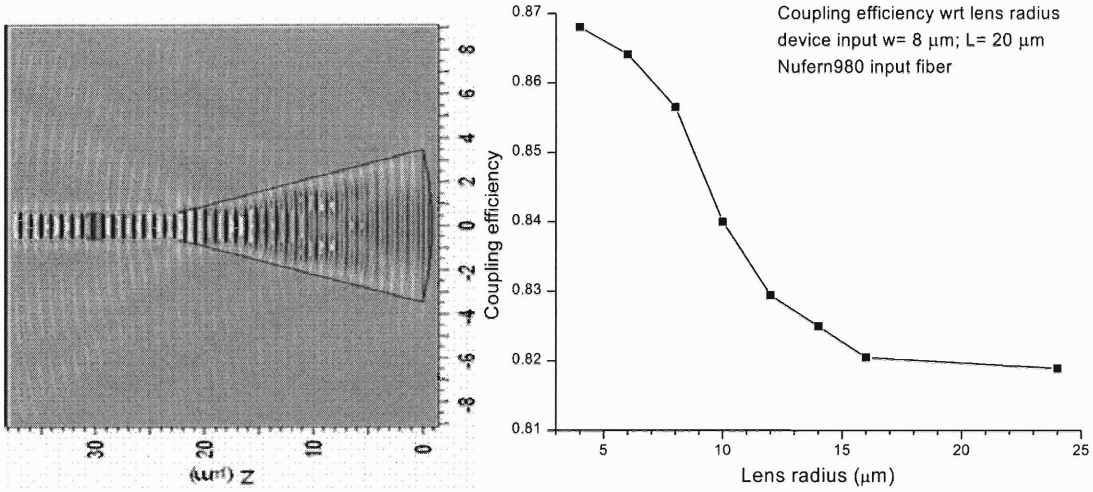

For a 3D coupler structure, the coupling efficiency is the product of the coupling efficiencies yielded from 2D FDTD simulations. As a result, theoretically, a linear taper of length L=20 μm without lens is expected to have a 0.68 coupling efficiency. A taper with lens radius R= 5 μm has a 0.71 coupling efficiency.

7.2.3. Packaging misalignment

As mentioned above, we used active alignment on Newport Auto Aligner station to obtain the best placement of the fiber in front of the coupler structure. We also investigated the effect of misalignments in both horizontal and vertical directions. The results are reported for tapers with and without a 5 μm input facet lens at L=20 μm.

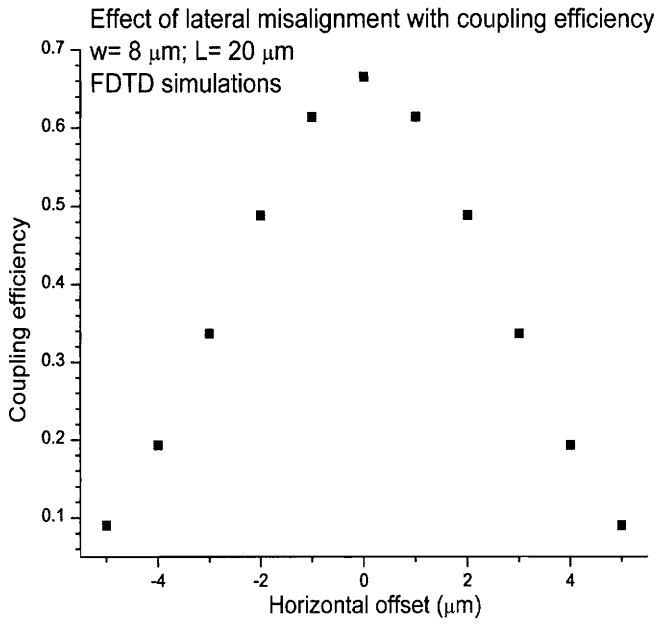

Figure VII-5. FDTD simulation of coupling efficiency as a function of misalignment in the lateral direction is shown. Since both the Nufern980 fiber and the coupler are symmetrical in the lateral direction, the fit is a symmetrical Gaussian curve.

To investigate the effect of lateral misalignment with coupling efficiency, FDTD simulations were performed and results are reported in Figure VII-5. The coupling efficiency of the vertical GRIN is assumed to be 0.82. Since both the fiber and the coupler are symmetrical in the lateral direction, the fit is a symmetrical Gaussian curve. At 4 μm offset from center, only half of the fiber is contained within the coupler. However, since the taper does not provide much confinement in this case, more power will leak out and result to a coupling efficiency of only 0.2 as seen in the simulation output.

We also simulated with FDTD the fiber vertical offset to understand the effect of misalignment on the asymmetrical GRIN structure. When the fiber is moved up 3 μm, its center is lined up with top of the GRIN and only power in its lower half is coupled into structure. When the fiber is moved down 3 μm from the optimized position, now only power in its top half is coupled by the structure. The trend in the Figure VII-6 indicates

the asymmetrical nature of the structure. The lower layers in the stack, which have higher indices, contribute more to the mode transformation.

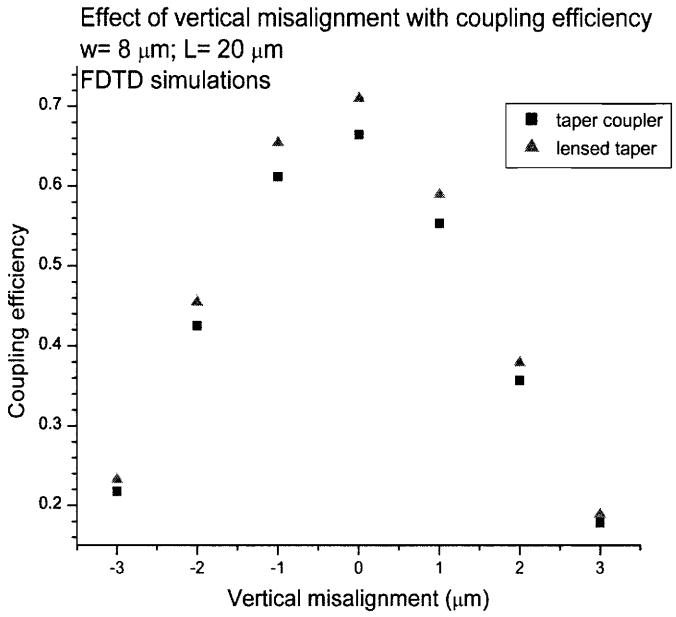

Figure VII-6. FDTD simulation results for coupling efficiency as a function of vertical misalignment are plotted.

We have designed a compact structure to couple light from a single mode fiber with mode field diameter of 6-10 μm to a $Si_xO_yN_z$ waveguide of 0.9 μm x 0.9 μm. We propose a novel coupling scheme which achieves simultaneous vertical and horizontal confinement, using an asymmetric step-wise parabolic index profile vertically and a combination of a lens and taper in the horizontal direction. At short length of 20 μm and thickness d=6 μm, FDTD simulation results show 0.68 efficiency or 1.65 dB insertion loss from a Nufern980 fiber (MFD 6.8 μm).

These simulation results assisted us in designing the first coupler prototype. The fabrication process at MTL has its own limitations that will affect the coupler's performance. We re-did some FDTD simulations when the fabrication had been completed to take into account these changes. The new FDTD results are reported later in chapter 11.

Chapter 8: Material Development for $Si_xO_yN_z$ Waveguide and Asymmetrical GRIN Structure

High index contrast (HIC) silicon nitride (Si_xN_y) and silicon oxynitride ($Si_xO_yN_z$) waveguides with oxide cladding have wide applications on planar optical circuit because they have small dimensions, low scattering loss and can be fabricated with silicon-based technology. Plasma-enhanced chemical vapor deposition (PECVD) is our fabrication technique for the materials of the waveguide and the asymmetrical GRIN structure.

PECVD is a promising technology for the fabrication of photonic devices, due to the method's flexibility in index engineering, good on-wafer, and wafer-to-wafer uniformity, much higher deposition rate compared with sputtering and LPCVD, and low thermal budget. $Si_xO_yN_z$ can be deposited by PECVD with continuous refractive index from 1.5 to 1.9. The typical deposition rate is about 3000 [A/min] at 400°C. The low temperature of the deposition process allows the integration of germanium-based devices. Wafer-to-wafer uniformity, deposition rate, and index, vary less than 1% for commercial systems.

In a PECVD process to deposit $Si_xO_yN_z$ film, silane (SiH_4) is the silicon source, while nitrous oxide (N_2O) provides oxygen-containing radicals, ammonia (NH_3) or nitrogen (N_2) provides the source for N radicals. By adjusting the ratio of these gases, the desired index is achieved. PECVD films contain a high percentage of hydrogen originated from the precursors, in N-H and Si-H configurations. At the deposition temperature of 400°C,

H atom cannot detach from its bonds and out-diffuses. N-H bond absorbs light in the C-band due to its second overtone vibration from 1490-1570nm.

8.1. $Si_xO_yN_z$ waveguide formed by PECVD

8.1.1. PECVD for $Si_xO_yN_z$ film of index 1.70

The $Si_xO_yN_z$ material for the waveguide was deposited with Applied Materials Centura reactor. The precursor gases are SiH_4, N_2O, and N_2. Patented design of the faceplate and gas blocker plate creates the hollow cathode effect[14], and thus enables the disassociation of N_2 to form N• radicals. The recipes for depositing film at index 1.70 are listed in Table VIII-1.

	Applied Materials Centura		
Deposition Temperature [°C]	400 (N_2)	500 (N_2)	400 (NH_3)
SiH_4 flow [sccm]	165	142	125
N_2O flow [sccm]	90	90	110
NH_3 flow [sccm]	--	--	110
N_2 flow [sccm]	3000	3000	4000
Power [W]	575	575	675
Pressure [torr]	4.2	4.2	4.2
Spacing [mils]	650	650	650

Table VIII-1; Recipes to deposit $Si_xO_yN_z$ films of RI 17.0 in our Applied Materials PECVD reactor are shown.

The film thickness and index at 630 nm are both measured by ellipsometry. The on-wafer thickness refractive index non-uniformity was calculated from a 49-point circular pattern.

	Applied Materials Centura		
Deposition Temperature [°C]	400 (N_2)	500 (N_2)	400 (NH_3)
Deposition rate [A/min]	5400	4600	5200
d uniformity[%]	0.6	0.8	0.8
RI @ 630nm	1.72	1.74	1.70
RI range	0.02	0.03	0.01

Table VIII-2: Properties of $Si_xO_yN_z$ films deposited by different recipes in Applied Materials PECVD reactor are liste.

In all reactions, a high flow of N_2 ensures good thickness and index uniformity across the wafer since the SiH_4 is better diluted. Reduction of the flow of N_2 to 2500 sccm in both of the above reactions results in RI range ~0.06.

The indices measured at 1310 nm and 1550 nm are lower than that at 630 nm due to dispersion effect. Below is the index calibration of a sample in that index range on a SOPRA ellipsometer.

RI@630 nm	**RI@1310 nm**	**RI@1550 nm**
1.75	1.74	1.74

Full data for the chromatic dispersion effect of PECVD $Si_xO_yN_z$ materials is in Appendix B.

8.1.2. Calculation of atomic Hydrogen percentage

In the SiH_4/ N_2O/N_2 PECVD plasma, the lightweight N• and SiH• radicals are formed. In contrast, the reaction in SiH_4/N_2O/NH_3 plasma leads to a majority of heavy $SiH(NH_2)_2$ and $Si(NH_2)_3$ radicals[10, 15, 16] . The latter film has a higher amount of atomic H and N-H bond density.

The content of atomic hydrogen in the $Si_xO_yN_z$ films was calculated based on FTIR absorption bands through the Lanford and Rand calibration[11]. The FTIR system is a Nicolet Magna 860 with IR source and DTGS KBr detector. Peak intensities at the first overtone of N-H and Si-H, respectively at 3300 [cm^{-1}] and 2200 [cm^{-1}], were extracted. From these intensities, the atomic H% was calculated.

	Applied Materials Centura	
Film Index	**$Si_xO_yN_z$** - 400°C (N_2)	**$Si_xO_yN_z$** - 500°C (N_2)
Atomic H%	10.3	8.6
Atomic H% in N-H	4.8	4.7
Atomic H% in Si-H	5.5	3.9

Table VIII-3: Atomic H% contents for $Si_xO_yN_z$ films with RI of 1.70 at two substrate temperatures are shown. Higher substrate temperature results in lower total H atomics %.

At higher substrate temperature, the atomic H% percentage is reduced. Most of the reduction is in Si-H bonds since their dissociation reaction is more thermodynamically favorable compared to that of N-H.

$$2\ \text{N-H} \rightarrow H_2 + \text{N-N} \quad \Delta E=1.55\ \text{eV}$$

$$2\ \text{Si-H} \rightarrow H_2 + \text{Si-Si} \quad \Delta E=-0.49\ \text{eV}\ [12]$$

As a result, lower absorption loss in the C-band can not be achieved by raising the substrate temperature to 500°C.

8.2. Fabricating $Si_xO_yN_z$ films of the GRIN stack

The graded index structure requires the development of PECVD recipes for $Si_xO_yN_z$ films of indices ranging from 1.50 to 1.70. We developed their recipe using the recipe of RI=1.70 as a starting point.

The PECVD reaction with $SiH_4/N_2O/N_2$ to form $Si_xO_yN_z$ can be modeled using the following two competing reactions: (a). SiH_4 /N_2O radicals to form Si-O bonds, and (b) SiH_4/ N_2 to form Si-N bonds. N_2 gas flow is kept high to maintain good on-wafer uniformity. Therefore, N_2 is not the limiting reactant and we adjusted SiH_4 and N_2O flow rates to achieve new indices.

8.2.1. Deposition recipe for $Si_xO_yN_z$ films with index below 1.70

For films of indices from 1.50 to 1.70, the N_2 flow can be maintained at 4000 sccm. As we reduce the SiH_4/ N_2O ratio, the index decreases. The relation between the gas ratio and index is graphed in Figure VIII-1. We established the recipes at index increments of 0.05 (1.50, 1.55, etc...). Using these marking posts, we can extrapolate the deposition conditions of film that has in-between index.

Figure VIII-1. Variation of index with flow rates of SiH_4 precursor in PECVD recipes to deposit $Si_xO_yN_z$. At RI> 1.55, the recipes have high N_2- low N_2O flow rate.

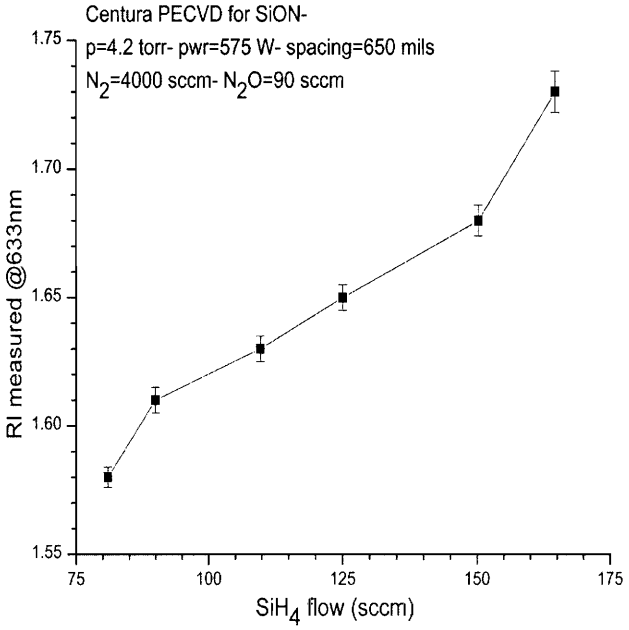

The deposition rate increases with SiH_4 flow. At SiH_4 flow rate of 80 sccm and index of 1.57, the deposition rate is 2150 A/min. At higher flow rate of 165 sccm and index of 1.73, the deposition rate increases to 5300 A/min.

To achieve indices lower than 1.5, the recipes were developed based on the oxide recipe. In these recipes, the N_2O are flown at much higher rate. The N_2 flow rate was reduced to below 1000 sccm and we could still maintain good wafer uniformity since now both N_2O and N_2 serve as diluents. The deposition rates are also high despite lower plasma power. The deposition rate is 1 μm /min at index of 1.47, and 7500 A/min at index of 1.52. We believe that in recipes to deposit films of indices higher than 1.55, the rate of N- radicals production is the limiting factor. Since the N_2 bond has higher dissociate energy than N_2O bond, its rate of molecular dissociation is slower, and this smaller dissociation speed will result in to lower film deposition rate.

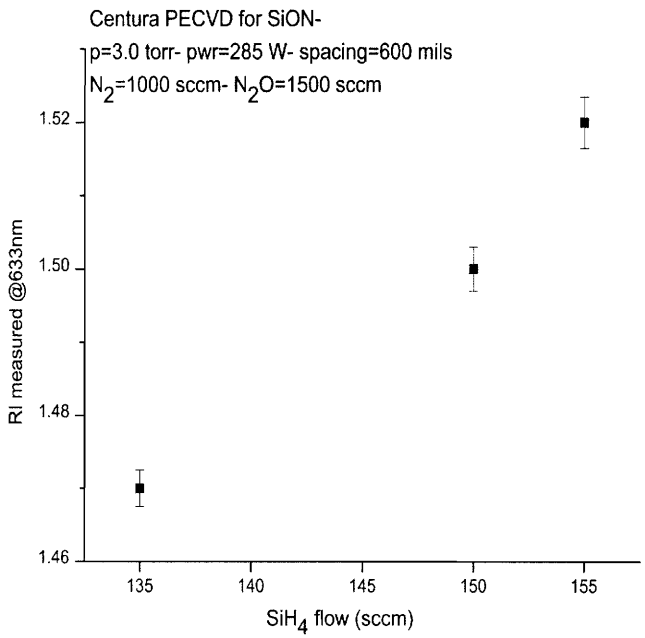

Figure VIII-2. Variation of index with flow rates of SiH_4 precursors in PECVD recipes for $Si_xO_yN_z$ films of index < 1.50. Their recipes are developed with high N_2O flow rate.

8.2.2. Deposition of $Si_xO_yN_z$ films with index above 1.70

The advantage of the GRIN design in confining the beam vertically is the capability to scale the indices of its layers to couple light into the waveguides of higher indices. We chose the index of 1.70 for this project because of system design issues. However, the same scahme can be used to efficiently couple light from a single mode fiber to a single-mode waveguide whose core is Si_xN_y or higher index $Si_xO_yN_z$ materials. Tuning the indices of PECVD Si_xN_y film had been studied and presented in chapter 2-3 of the thesis. In this section, we present the recipes for PECVD of $Si_xO_yN_z$ films with indices higher than 1.70 and less than 1.90 of N-rich nitride.

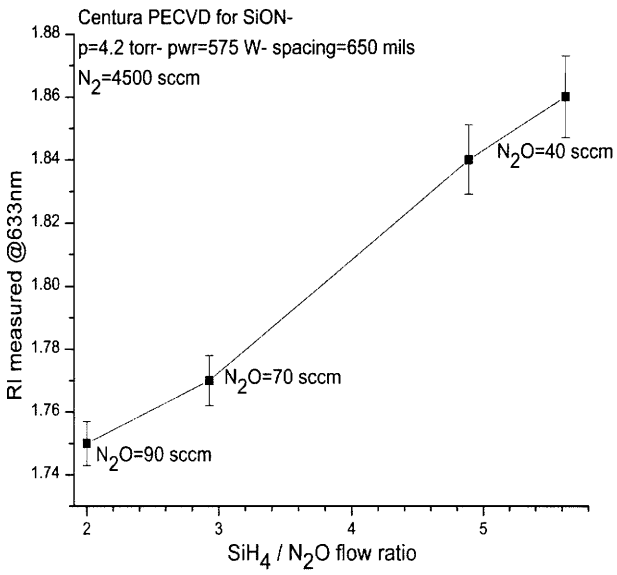

Figure VIII-3. PECVD recipes for $Si_xO_yN_z$ films of index from 1.75-1.90 are shown.

In order to extend the index from 1.72, SiH_4/N_2O flow ratio is increased. To maintain good on-wafer uniformity, the N_2 must also be increased to 4500 sccm as we decrease N_2O flow to control SiH_4 flow rate. Only four films with high indices were deposited since we can always calibrate more recipes as need arises.

8.4. Propagation loss of $Si_xO_yN_z$ materials RI=1.70

The losses of our $Si_xO_yN_z$ films were measured both in slab-mode propagation as well as in waveguide propagation. Slab-mode propagation loss is measured on a Metricon system

via prism coupling techniques while the waveguide loss is measured by the Fabry-Perot and cutback methods at 1550nm.

8.3.1. Slab loss measurements via prism-coupler

a. Techniques and sample preparation

This method measures the intensity of the fundamental mode as it propagates in the slab film as shown in Figure VIII-4. The intensity is then fitted to a propagation curve $I(z) = I_0 * e^{(-\alpha z)}$ to extract the propagation constant α. This method only measures the material loss, and does not include scattering loss associated with fabrication of waveguide structures.

The $Si_xO_yN_z$ film of interest was deposited on silicon wafers oxidized to form a 3 μm thick oxide film. Thermal oxide is used as a substrate due to its small surface roughness, which results in minimum scattering loss at the interface. The oxide under clad must be sufficiently thick so that no light leaks into the silicon substrate. The $Si_xO_yN_z$ film must be sufficiently thick to support at least one propagation mode at the measured wavelength. For material of index 1.70, $Si_xO_yN_z$ film thickness of $d > 2$ μm can support three modes at 1550 nm.

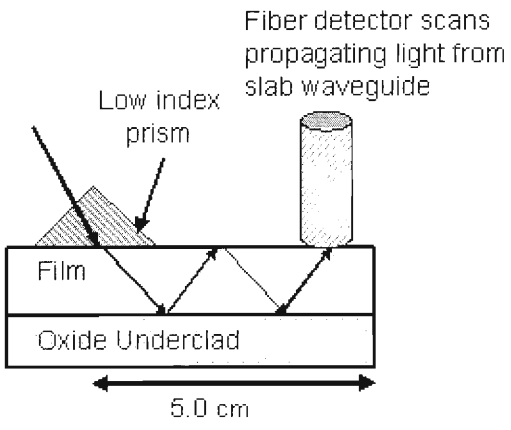

Figure VIII-4. Schematic illustration of the setup to measure slab loss with prism coupler. Measurement results of this method do not include scattering loss associated with fabrication of waveguides.

b. Measurement results

The $Si_xO_yN_z$ film slab losses were measured on a Metricon Prism 2010, using prism code 1048.4. The losses were measured at 630nm, 1310 nm and 1550 nm. The Metricon slab loss results from for $Si_xO_yN_z$ films of index 1.70 are listed in Table VIII-4.

	Slab-mode propagtion loss		
	@630nm	**@1310nm**	**@1550nm**
RI=1.72 $Si_xO_yN_z$ - 400°C (**1**)	1.8 ± 0.1	0.5 ± 0.2	2.6 ± 0.2
RI=1.74 $Si_xO_yN_z$ - 500°C (**2**)	2.2 ± 0.1	0.2 ± 0.1	1.9 ± 0.1

Table VIII-4: Slab mode propagation losses for PECVD $Si_xO_yN_z$ films at index 1.70. The propagation loss at 1550 nm is lower for materials deposited at higher substrate temperature.

Figure VIII-5. Light intensity as a function of slab mode propagating distance measured at: 1307 nm and 1550 nm. For PECVD $Si_xO_yN_z$ film, higher loss at 1550nm is induced by N-H absorption.

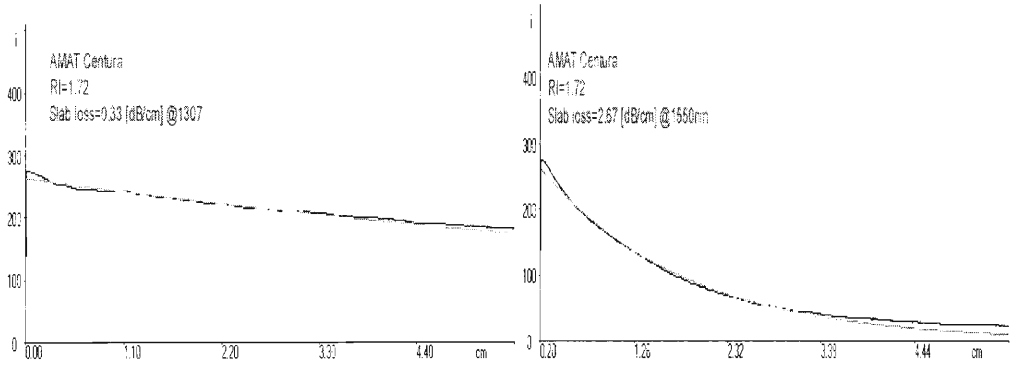

8.3.2. Measuring waveguide loss by Fabry-Perot method

Single mode channel waveguides of RI=1.72 with dimensions 0.9 μm x 0.9 μm were fabricated. The waveguide was defined by RIE on the HDP Centura oxide etcher. 4 μm of PECVD oxide was subsequently coated to form the upper clad. The wafer was then diced and the die's facets were polished. The Fabry-Perot resonances were obtained for wavelengths near 1550 nm. Since the wavelength limit for our tunable laser is 1450 nm, waveguide loss at 1300 nm was not measured.

The Fabry-Perot resonant loss measurement technique method is based on the ratio of maximum and minimum resonances induced during spectral scan. The propagation loss α is calculated by [50]

$$\alpha[cm^{-1}] = -\frac{1}{L} * \ln(\frac{1}{R} * \frac{\sqrt{\mathrm{Im}\,ax / \mathrm{Im}\,in} - 1}{\sqrt{\mathrm{Im}\,ax / \mathrm{Im}\,in} + 1})$$

Loss in [dB/cm] = 4.34 * α

I_{max}, and I_{min} are the Fabry-Perot resonances.The waveguide length, *L*, was measured by a profilometer for better accuracy. R is the reflectivity at air/waveguide interface.

Our single mode waveguide of RI=1.72 ((1) in Table VIII-4) has a loss of **4.7 ± 0.6** dB/cm at 1550 nm. For waveguide of RI=1.74 ((2) in Table VIII-4), the loss is **4.3 ± 0.5** dB/cm at 1550 nm.

8.3.3. Measuring waveguide loss by cutback method

a. *Principal of measurement*

Another method to measure propagation loss in a waveguide is the cutback method. In this method, the powers transmitted through paperclip waveguides are plotted as a function of their lengths. If P, P_0 are the power of waveguide of length x and x_0, the propagation equation is:

$$P = P_0 * e^{-\alpha \Delta x}$$

Where $\Delta x = x - x_0$

$$\ln(\frac{P}{P_0}) = -\alpha \Delta x$$

Propagation constant α is extracted from the curve fit. The bending radius in the paperclips waveguides is very large. As a result, the bending loss is small and does not affect the calculation of the propagation constant. In addition, since calculations are based on the difference in length of waveguides from a same chip, insertion loss can be ignored.

b. Waveguide fabrication using a silicon hard mask

The $Si_xO_yN_z$ film was deposited by PECVD at substrate temperature of 400°C on 3 μm thermal oxide under clad. The film thickness is 8700A and RI=1.72 at 630nm wavelength. A 2500A poly silicon mask was then grown by LPCVD at 625°C. The silicon mask is then patterned by He/Cl_2 plasma with 1 μm thick photoresist. The width of the waveguide is 0.9 μm.

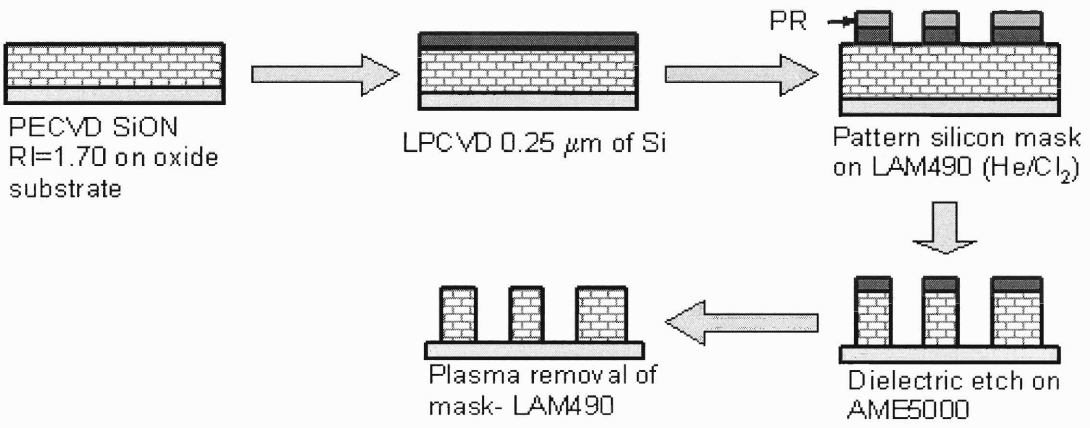

Figure VIII-6. Schematic illustration of process flow to fabricate $Si_xO_yN_z$ waveguides using a silicon mask is shown.

The dielectric was then etched in Applied Materials P5000 CHF_3 plasma. The etching yielded structures with smooth sidewall and a profile angle of 78°. The silicon mask was removed by He/Cl_2 plasma. The wafer was subsequently coated with a 3-μm PECVD oxide film for upper cladding. The SEM image of the fabricated waveguide is shown in Figure VIII-7.

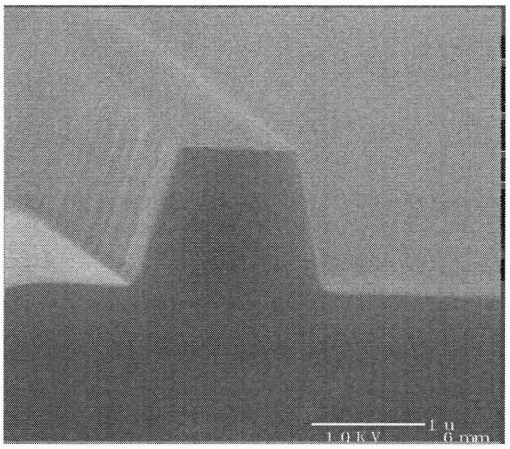

Figure VIII-7. SEM image of unclad waveguide index 1.70, defined by silicon mask and CHF_3 etching is shown on the right. The profile angle is ~78° with relatively smooth sidewall.

c. Measurement results

The paperclip waveguides are measured on the Newport Auto Aligner station. The SMF28 fiber (MFD=10 μm) was used to guide light into the waveguide. The Newport Auto Aligner system optimized the fiber positions in all three axes to obtain a maximum output power. Throughput powers of the paperclip waveguides were used to calculate the propagation loss.

To fit on the measurement stage, the chip was cleaved to pieces of approximately 5 mm in width. A shorter chip at 3mm length would pick up evanescent light from the input fiber; thus, increase the noise amount and lead to less accurate result.

Due to restriction of mask space, we only had 3 waveguides of different lengths and each has two turns of 50μm radius. The length increments from the straight waveguide are

714, 3314, and 5914 μm. For the fabricated single mode $Si_xO_yN_z$ waveguides of index 1.70, the propagation loss is **4.8 ± 0.5** dB/cm at 1550 nm. The result is similar to that obtained with Fabry-Perot resonances.

Chapter 9: Process Development for Etching Thick $Si_xO_yN_z$ GRIN Films

9.1 Wafer bow controlled by oxide back deposition

In the course of fabricating the couplers, we would need to process the wafer through an optical lithography system and a Centura plasma etcher. Both are sensitive to wafer bow. Wafer bow first affects wafer transferring in the systems since there is no longer a seal between the vacuum transfer arm and wafer's back. Similarly, in the Centura etcher, if there is no vacuum between the wafer's back and the He cooling plate, the wafer is heated up quickly and etch rate is affected. On the optical lithography system, alignment between levels can vary on a bowed wafer due to different traveling distances from the alignment laser to wafer's center and to the wafer's edge. The interlock in both systems will reject a wafer with higher than 80 μm bow in either direction. We have to ensure our wafers' are acceptable with these systems' requirements.

Wafer bow is an issue in processing thick films since it increases with thickness at constant film stress. Film stress is induced when the wafer is cooled down from deposition temperature to room temperature. PECVD $Si_xO_yN_z$ and silicon oxide films deposited at 400°C and above are compressive.

In PECVD reaction, minimizing the film stress without affecting other wafer properties is challenging. Instead, we reduced only the wafer bow by depositing compressive oxide film in the back without modifying the film stress. For a 7 μm thick film on silicon

wafers, the wafer bows before and after oxide backside deposition are listed in Table IX-1

	Stress [MPa]	Bow [μm] after 7μm film deposition	Bow after 3 μm oxide back deposition
$Si_xO_yN_z$ (RI=1.70) - sub. temp 400°C	-120 Compressive	130	90
$Si_xO_yN_z$ (RI=1.72) - sub. temp 500°C	-100 Compressive	90	50

Table IX-1: Compensating for frontside wafer bow is accomplished by depositing oxide film in the back as demonstrated on wafers with 7 μm thick $Si_xO_yN_z$ film.

The film deposited at 500°C with oxide back deposition was handled well by both tools. We would need to deposit a thicker film for $Si_xO_yN_z$ film stack deposited at 400°C.

9.2 Etching of thick oxide or $Si_xO_yN_z$ using a PR mask

The fabrication of the graded index $Si_xO_yN_z$ stack requires 5-7 μm deep plasma etch. We combined fabrication knowledge and in semiconductor and MEMS processing to develop a deep-etch process for oxide and $Si_xO_yN_z$ thick films. Our two main challenges for successful deep etching are the selection of an appropriate mask material and an optimal anisotropic etch recipe that delivers desired selectivity between mask and $Si_xO_yN_z$ material. We first conducted experiments in etching a 7-μm thick $Si_xO_yN_z$ film using a thick photoresist (PR) mask in high-density plasma Centura chamber.

.

9.2.1. Process flow

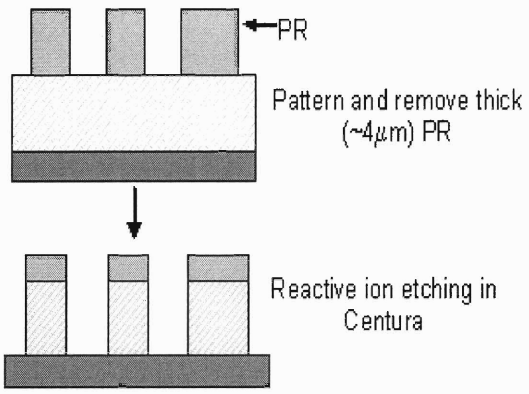

The process for etching a thick film using a PR mask was completed in ICL. We use the Nikon optical stepper to define the PR shape. Then, a reactive ion etcher was used to etch the stack. The process flow schematic is illustrated in Figure IX-1 on the left.

Figure IX-1. Process flow illustration for etching a $Si_xO_yN_z$ film using a PR mask and high density plasma (HDP) is shown.

9.2.2. Improving coating process to spin thicker PR

To etch a 7-μm film of $Si_xO_yN_z$ with index of 1.70 at high plasma density, a PR film of minimum 3 μm thickness is needed. The PR is deposited on a coater track in ICL and its thickness is measured by an ellipsometer. For SPF 1.2 PR, at a spin rate of 1500 rpm, the first coat yielded d=2.0 μm with a non-uniformity of 1.0%. Applying a second coat at 1200 rpm yielded d=3.3 μm with a non-uniformity of 1.6%.

After the third coat had been applied at 1200 rpm, the thickness was 3.9 μm with a non-uniformity of 6.2%. The increments in coating thickness are successively smaller because the PR is solvent based. So, the next PR application will dissolve some of the PR of the previous coating. Since the PR near the wafer's edge is more easily washed away in spin coating than at the center, the on-wafer thickness non-uniformity increases.

To improve adhesion, roughening of the 1st coat was considered as an option. The PR surface was roughened by exposing for 5s to Ar/O_2 plasma, and then 2nd coat was applied. The final thickness is measured at 3.9 μm, the sum of two coats. However, since the Ar/O_2 plasma changes the sensitivity to light of the PR film, the roughened film could not be developed with current, conventional setup and chemistry. Besides, for our current application, the mask's thickness of 3.3 μm is sufficient.

9.2.3. Principles of reactive ion etching in high density plasma for $Si_xO_yN_z$

Reactive ion etching (RIE) was utilized to define the structure. RIE is an etching technique that combines physical sputtering and chemical reactivity. Oxide/ $Si_xO_yN_z$ RIE processes that base on fluorocarbon gases are commonly used in the semiconductor industry due to its high selectivity with silicon and good etch directionality. The fluorocarbon gas is dissociated in the plasma as free fluoride F- and CF_n^+ ions. Fluoride ions and sputtering are responsible for etch. The CF_n^+ ions are deposited on the substrate as a fluorocarbon polymer film. On oxide surfaces, they react with oxygen to form volatile gases such as CO, CO_2, and COF_2. As the fluorocarbon film is reduced, the free fluoride can continue to etch the silicon.

On the other hand, this protecting film does not react on the silicon or PR surface. As a result, Si-F reaction cannot occur. Other etching gases such as SF_6 and NF_3 are isotropic and etch silicon at the same rate as oxide since they do not form such protective polymers. The fluorocarbon film deposition rate and F/C ratio in the etching gas are determining factors to the structure shape, the etch rate, the selectivity to the mask, and the underneath substrate[51].

For the PR mask, we used the Centura ECR (electron-cyclotron resonance) plasma etch system to take advantage of its low-pressure operation and high plasma density. In high plasma density, we still can achieve a higher etch rate even with gas of lower F/C ratio since the gas is better dissociated. In addition, low pressure and high ion bombardment increase etch anisotropy because they accelerate etching in the vertical direction while minimize lateral erosion[52].

The two gases utilized in the Centura etch are C_2F_6 mixed with CH_3F. C_2F_6 provides the high etching rate due to the abundance of F^+ ions. Since C_2F_6 is a strong isotropic etching gas due to high F/C ratio, we minimized sidewall erosion and roughness by mixing in CH_3F gas, which has a lower F/C ratio. A carbon-rich CH_3F forms carbon-rich polymer films[53] to reduce the lateral etching rate. By combining all the above advantages, we hope to achieve high etching rate and straight sidewall.

The etch conditions are

Power [W] =1800	C_2F_6 [sccm]= 17.9
Bias [W]=490	CH_3F [sccm] = 12.1
p [mtorr]= 3	

The etch rates on blanket wafer of PECVD oxide, $\underline{Si_xO_yN_z}$ and baked PR films are:

	Etch rate [A/s]
PECVD Oxide	54
PECVD $\underline{Si_xO_yN_z}$ (RI=1.70)	57
High-temp baked PR	23

Table IX-2: Etch rate rate calibration for $Si_xO_yN_z$ / oxide and PR mask in high density plasma chamber.

We calibrated the etching time to a 7-μm thick $Si_xO_yN_z$ stack to be 1230 seconds. Although the wafer is cooled by Helium on the wafer backside, the wafer temperature increases due to the intense ion bombardment. Therefore, extended etch time is not recommended and we should divide the time into 70-second etch steps. Seventeen 70-sec etches plus one 40-sec etch were performed.

9.2.4. Etch results analysis

This SEM work was performed at Analog Devices Inc. From the images, we observe that after 7 μm of $Si_xO_yN_z$ is removed, there is still approximately 1.5 μm of PR remaining on top of the structure. We estimated that the selectivity between PR and $Si_xO_yN_z$ for the patterned wafer is ~3.5. The PR is thicker at the center and slopes down to the etched wall. The structure angle is 76 degree due to severe lateral etching of the PR mask. The angle in the PR layer is translated into the slope profile of the structure.

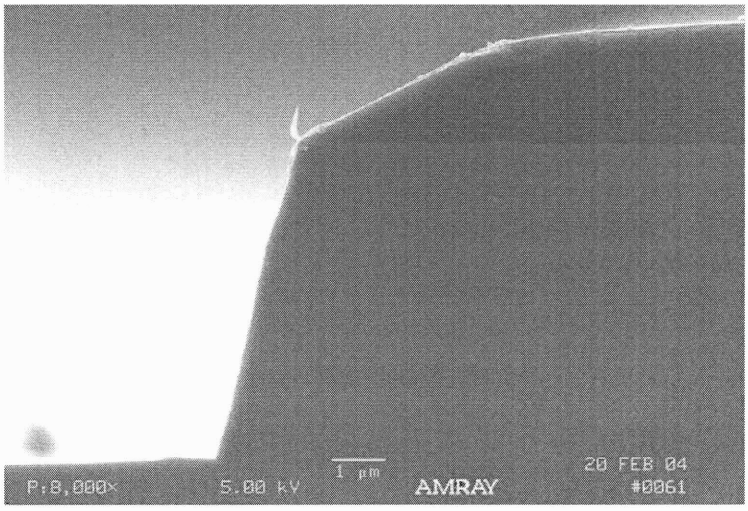

Figure IX-2. SEM cross-sectional image of 7 μm $Si_xO_yN_z$ after RIE using thick PR mask is shown. The image shows severe mask erosion that transfers to small angle profile.

To improve the sidewall profile, we must use a mask that is more resistant to isotropic plasma etching. Two material systems can be used: metal or LPCVD silicon. Since metal is not allowed in the oxide etcher in ICL, we explored the feasibility of silicon mask.

Silicon is absorbing in the UV and thick film prevents the lithography source from recognizing alignment marks in multi-mask fabrication. Therefore, we need to develop an etch process that has higher selectivity for Si to $Si_xO_yN_z$. A minimum selectivity of 7 is needed.

9.3 Reactive ion etching of thick $Si_xO_yN_z$ layer using LPCVD silicon mask

To improve the angle profile, we conducted etch experiments with thin Si mask that is more resistant to plasma isotropic etching. Plus, we needed to develop an etch process that has higher selectivity for Si/ $Si_xO_yN_z$. In this next chapter, we report the development of an etch process that fulfils the above two requirements.

9.3.1. Principles of selective etching of oxide or $Si_xO_yN_z$ with silicon mask

Selective reactive ion etching of oxide/ $Si_xO_yN_z$ with silicon mask can be achieved with fluorocarbon carbon plasma. On the wafer, although the CF_n^+ (n=2, 3) ion flux is the same to silicon and oxide surfaces, the fluorocarbon polymeric film on silicon is thicker than that on oxide. The thinner film on oxide surface is due to the continuous freeing of oxide through the formation of the volatile COF_n. Because the film on silicon is thicker, thus longer distance for diffusion of released species, the etch rate of silicon is slower. So, the etch rate of silicon strongly depends on the thickness of its fluorocarbon film.

In addition, the silicon etch depends more strongly on the F/C ratio of the fluorocarbon film than oxide etch. One known example is the addition of H_2 to CF_4 RIE. In pure CF_4 RIE, the SiO_2 /Si selectivity is small. However, the addition of H_2 to CF_4 slows the etch

rate of silicon down; thus, it increases the selectivity over oxide[54]. In CF_4 plasma, the main radical is CF_3^+. The addition of H_2 results in subsequent reaction $CF_3^+ + H \rightarrow CF_2^+ + HF$. Thus, CF_2^+ now becomes a more dominant radical. By lowering F/C ratio in radicals, the fluorocarbon etch rate on silicon decreases since F is the etching agent. On the other hand, the oxides etch rate changes insignificantly. As a result, the SiO_2/ Si selectivity increases. Same effect is observed in RIE of CHF_3 plasma due to a same reaction mechanism[55, 56].

Experimentally, we observed a four fold increase of RIE selectivity when switching from (CF_4/CHF_3) mixture plasma to pure CHF_3 plasma. The two plasma conditions are listed in Table IX-3.

CF_4/ CHF_3 etch recipe	
p [mtorr]= 200	Power [W] =350
CF_4 [sccm]= 8	Magnetic field [Gauss]= 50
CHF_3 [sccm]= 6	Coupled bias [W]= -275
CHF_3 etch recipe	
p [mtorr]= 40	Power [W] = 400
CHF_3 [sccm]= 30	Magnetic field [Gauss]= 90
	Coupled bias [W]= -300

The etch rate and selectivity are

	LPCVD Si etch rate [A/s]	**Oxynitride etch rate [A/s]**	**poly-Si/ SiON selectivity**
(CF_4/ CHF_3) mixture	5.2	22.5	4.3
(CHF_3) plasma	2.7	44.2	16.3

Table IX-3: Higher selectivity to silicon mask was observed when CHF3 gas is mixed in with CF4 for plasma etching in P5000.

In the CHF_3 chemistry, the $Si_xO_yN_z$ etch rate is essentially unchanged if we scale with total flow rate, or total F atoms. However, the silicon etch rate is reduced by four ➔ the selectivity has increased by four fold.

9.3.2. Procedure for etching thick $Si_xO_yN_z$ film using a LPCVD silicon mask

The silicon mask was defined by anisotropic RIE etch to assure a straight profile by He/Cl_2 plasma. In LAM490, the oxide/silicon selectivity is found to be approximately 30:1, close to those in most literature[57]. The $Si_xO_yN_z$ film was then etched with CHF_3 chemistry. A process flow in Figure IX-3 illustrates the steps associated with using the LPCVD mask.

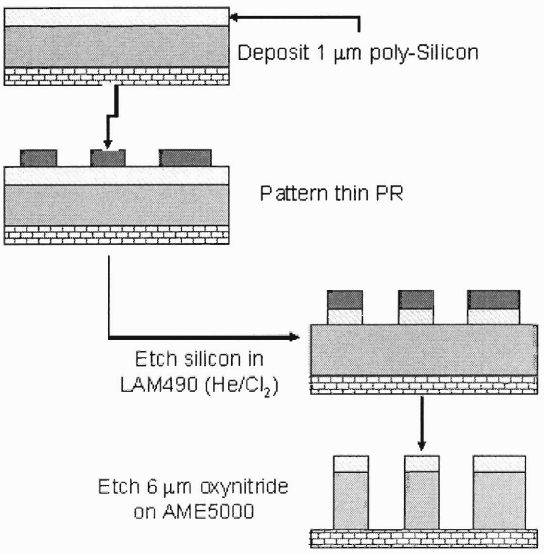

Figure IX-3. Process flow for etching thick $Si_xO_yN_z$ film using thin silicon mask and CHF_3 etching gas is shown.

9.3.3. Etching silicon mask

Etching of the silicon mask was completed on the LAM490B using the standard 50% overetch recipe with the displayed etch rates. Since the selectivity is high between the silicon and others, the silicon-coated wafer should be free of native oxide film before etching. A 30-second HF dip is recommended.

	Etch rate [A/s]
Oxide	1.8
Oxynitride	2.9
LPCVD Silicon	70

Table IX-4: Etch rate calibration for standard anisotropic etch of silicon in LAM490 chamber with He/Cl_2 plasma.

9.3.4. Etching $Si_xO_yN_z$ film with silicon mask in HDP

We first conducted etch rate calibration to establish silicon/ $Si_xO_yN_z$ selectivity in high density plasma. The available gases are C_2F_6, CH_3F, and CHF_3. In C_2F_6 plasma, CF_3 and CF_3^+ are the most abundant neutral and ionic species, respectively[58]. These etches tend to be very isotropic that will results in undercut and mask deterioration. CHF_3 plasma produces CHF_2^+ and CF^+ at plasma power of 600-1200 and 1400 W, respectively[59]. Although the etching rate is reduced with the lower F/C ratio, the selectivity to silicon mask should be higher.

Four etch recipes in high density plasma were explored. The plasma power was set at 1800 W – 2400 W. The etch rates and their selectivity are listed in Table IX-5.

	Oxide etch rate [A/s]	**Oxynitride etch rate [A/s]**	**LPCVD Si etch rate [A/s]**	**Selectivity Si/ SiO_2**
C_2F_6-only (**1**)	57.9	52.9	30.7	1.89
High C_2F_6/ CHF_3 (**2**)	53.9	-	24.4	2.21
Low C_2F_6/ CHF_3 (**3**)	47.1	-	29.7	1.59
C_2F_6/ CH_3F (**4**)	53.8	55.0	25.5	2.11

Table IX-5: Etch rate calibration for anisotropic etch of $Si_xO_yN_z$ in HDP chamber with different plasma chemistries. Low selectivity to the silicon mask is due to high ion bombardment.

We observed that in HDP, the etch selectivity between SiO_2/ Si is low since substantial ion bombardment makes chemical difference between materials less important. At high power and bias, the fluorocarbon polymeric film on silicon is thin; thus, its silicon etch rate will increase. To etch a 7 -μm thick film on Centura, we need an unacceptably thick ~3.5 μm of LPCVD Si mask. So, we explored the use of a magnetically enhanced RIE in ICL called AME P5000 to continue our work.

9.3.5. Result analysis for RIE using CHF_3 chemistry at low power

The two fluorocarbon gases available on AME5000 are CF_4 and CHF_3. We can achieve higher mask selectivity with CHF_3 plasma, rather than mixing in CF_4. At low power, the dominant species is CHF_2^+. We explored three CHF_3 recipes that vary in power and pressure at constant CHF_3 flow of 30 sccm and magnetic field at 90 Gauss.

	p [mtorr]	Power [W]	Bias [W]	O_2 flow [sccm]
#1	40	400	-300	0
#2	25	500	-380	0
#3	25	500	-380	3

In recipe #3, we explored the properties of O_2-mixed recipe as a method to get rid of micro masks. Micro mask is common in deep oxide etching with PR mask. In micro mask, specks of PR are sputtered on the oxide clear field. Due to high etch selectivity, the PR specks become masks that stop etching of the underneath oxide. Sharp columns of oxide are formed [60]. By mixing in a small oxygen flow, we will be able to prevent PR deposition on the oxide surface.

We found from observation with microscope that micro mask did not exist when silicon mask was used. We believe that at low bias power, the silicon mask is hard enough to not be sputtered off as PR is. The etch rates of different materials and the selectivity are reported in Table IX-6

	Oxide etch rate [A/s]	$Si_xO_yN_z$ etch rate [A/s]	LPCVD Si etch rate [A/s]	$Si_xO_yN_z$ / Si selectivity
#1	32.4	44.2	2.7	16.3
#2	36.1	53.3	3.6	14.8
#3	37.3	45.5	8.7	5.2

Table IX-6: Etch rate calibration for anisotropic etch of $Si_xO_yN_z$ / SiO_2 in P5000 chamber at different powers and pressures. High selectivity to the mask is achieved.

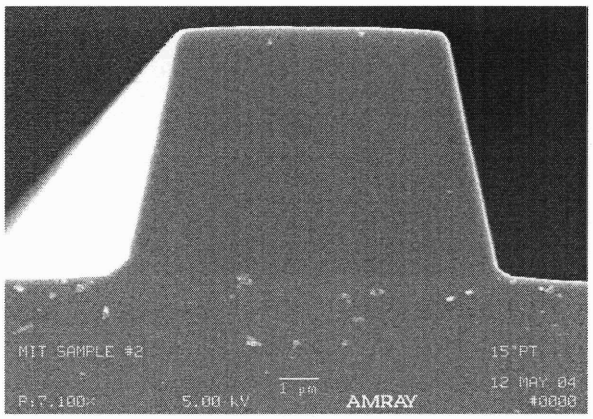

High power and low pressure result in high bias power and profile angle closer to 90 degree. However, for the AME5000 system, at high power and low pressure, the etch rate non-uniformity is high at 6.0%. The etch rate is faster at the wafer center and slower at the edge. At lower power and high pressure, the etch rate non-uniformity is smaller at 2.1%. We used a two-step etch process. First, we used the high-power, low-pressure recipe #2 to remove most of the $Si_xO_yN_z$ thick film. Then in the 2nd step, the low power, high-pressure recipe #1 was utilized to remove the remaining material and to compensate for high non-uniformity created in step 1 etch. The results for etching 6 µm of $Si_xO_yN_z$ index of 1.70 are shown in the SEM pictures below. We achieved a profile angle close to 80°. We also did not observe a transition

point between two recipes on the structure sidewall which indicated that two recipes have similar lateral etching rates.

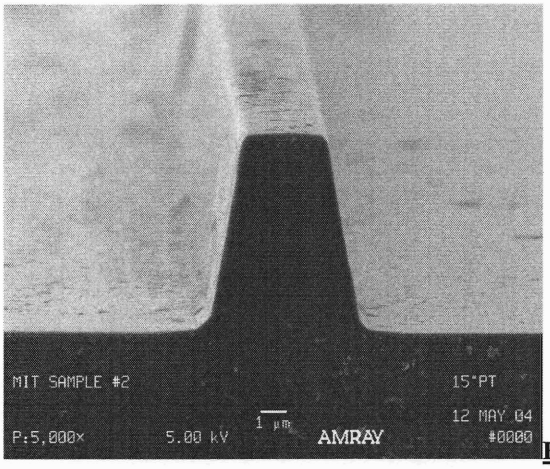

Figure IX-4: Cross sectional SEM images of 6 μm $Si_xO_yN_z$ after RIE using a silicon mask. The image shows no mask erosion that leads to a profile angle of near 80°.

9.3.6. Preventing micro mask formation during plasma etch for higher-index $Si_xO_yN_z$ or Si_xN_y materials

As observed from the SEM images, etching a 6-μm thick $Si_xO_yN_z$ film of index 1.70 using silicon mask and CHF_3 chemistry leaves no micro mask. However, if we need to etch a stack of higher index $Si_xO_yN_z$ or Si_xN_y materials for coupling into respective waveguides, micro masks of C-N polymer are likely to form.

C-N bond has formation energy of 251 kJ/mol, lower to that of C-H, and C-O bonds (338 kJ/mol and 399 kJ/mol respectively). As a result, radicals containing C-H is more thermodynamically favorable to form polymers on the nitride surface but not on the surface of oxide film [61]. For our waveguide structures, the potential problem is if the column created by micro mask is close to the waveguide, then loss due to scattering in the waveguide will increase. There are currently two common methods to avoid C-N

polymerization. NF_3 can be used in place of carbo-fluoro chemistry in the plasma[62]. The second method is to use oxygen plasma to clean off the polymer right after they are formed. The latter method can be incorporated to the existing etch recipes.

However, mixing O_2 flow in the plasma increases the silicon etching rate since the oxygen radicals will also oxidize silicon surface. Even a very small amount of O_2 mix will change the selectivity significantly. When 1 sccm O_2 flow was mixed in with recipe #2 in Table IX-6, we observed a doubling in silicon etch rate and constant oxide etch rate. As a result, the oxide/ silicon selectivity is reduced from 10 to 5.5. The $Si_xO_yN_z$ (RI=1.70) to silicon selectivity is also reduced from 12 to 7. To compensate for lower selectivity, to etch the same $Si_xO_yN_z$ thickness, thicker silicon mask is required.

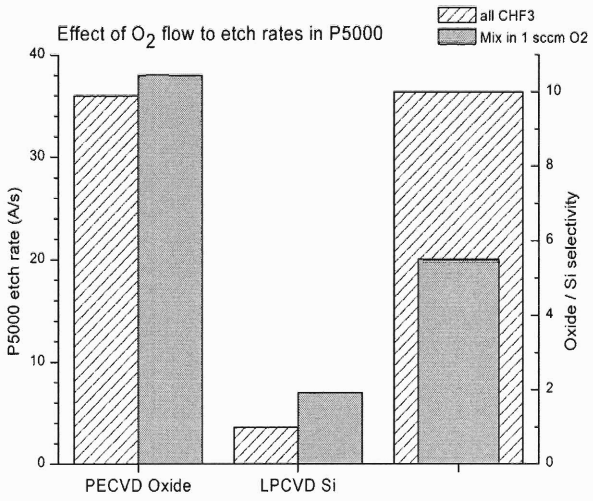

Figure IX-5. Etch rate variation with addition of small 1 sccm O_2 flow. Silicon/Oxide selectivity reduces by ½ with adding in O_2 to the P5000 CHF_3 recipe #2 of Table IX-6.

The second problem is that the oxygen mix recipe is more isotropic since the O_2-plasma thins down the polymeric film that protects the structure's sidewall. As seen in the SEM image of Figure IX-6, the angle now is 75°.

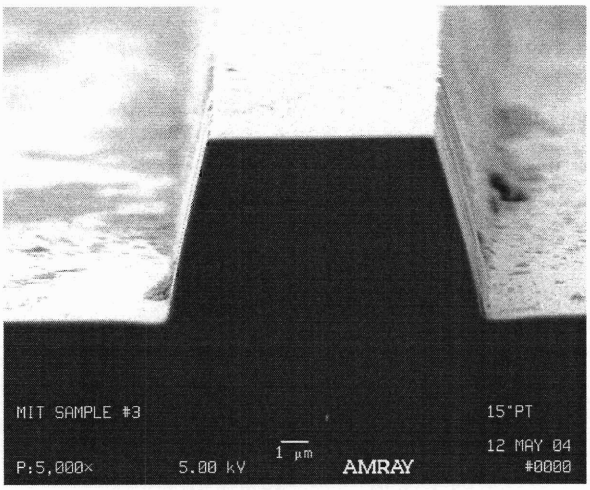

Figure IX-6. SEM image of 6 µm thick $Si_xO_yN_z$ film etched with (CHF_3 / O_2) plasma. Isotropy increases with O_2 mix.

So, to etch dielectric with high N atomic such as high index $Si_xO_yN_z$ or Si_xN_y materials, we may have to sacrifice the angle profile and etch selectivity to avoid the formation of micro masks.

In chapters 8, using PECVD technique, we developed and characterized propagation properties of $Si_xO_yN_z$ films at varying indices to build the vertically graded index structure. In chapter 9, we developed novel process to etch a 6-µm thick $Si_xO_yN_z$ films with silicon mask. The etching process with silicon mask solved the problems with mask erosion and small angle profile when thick photoresist is used. The novel etching recipe yields an 80 degree angle and a very smooth sidewall. We are now ready to build the coupling devices that we proposed in chapter 7.

Chapter 10: Fabrication of the Asymmetrical GRIN Couplers

10.1 Process flow for fabrication of couplers

The fabrication process of the coupler can be divided into three parts: (I) definition of waveguide, (II) formation of the taper, and (III) definition of the coupler's length plus fiber-end facet. The entire process flow is illustrated in Figure X-1 below. The detailed explanation of the process is in the next page.

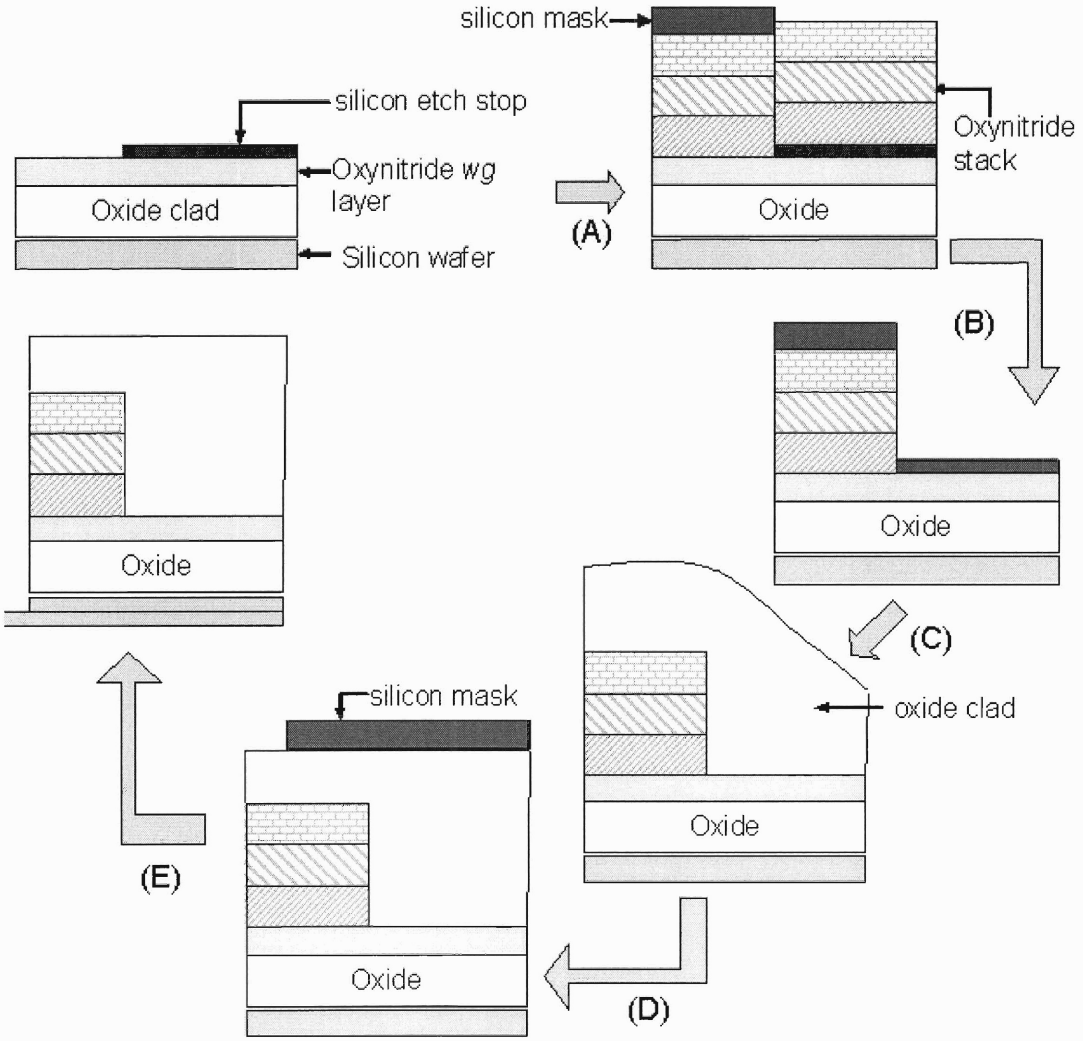

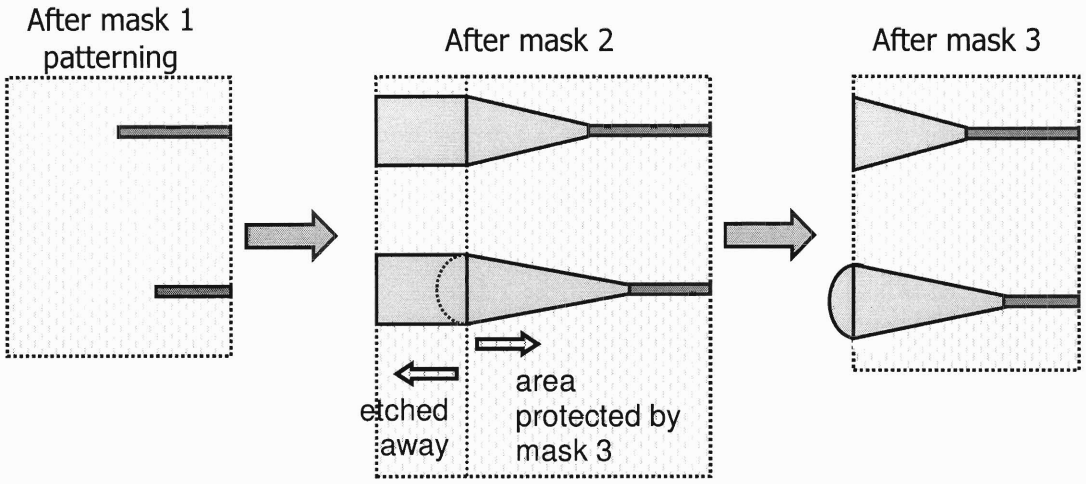

Figure X-1: Process flow for fabrication of the coupler in MTL. The devices were defined by 3 main steps that associate with 3 masks: (1). To define the waveguide; (2) to define the taper shape and (3) to define the fiber input facet with lens.

The entire fabrication process was completed in the integrated circuit lab (ICL) on tools designed for CMOS-compatible processes. In step (A), the wafer was deposited with $Si_xO_yN_z$ films with varying indices to form a step-wise asymmetrical graded index stack. The layer closest to the waveguide has the highest index of 1.68 while the topmost has index of 1.52. Silicon hard mask was then patterned to form the taper shape. In (B), the whole structure was etched down to the oxide substrate with the waveguide protected by the etch stop layer. The silicon from the hard mask and etch stop were removed and a thick oxide film was subsequently deposited to form an upper clad film in (C). In (D), chemical mechanical polishing process was utilized to planarize the structure. Another silicon mask was deposited and the fiber-end of the coupler was defined through deep etching of cladding and $Si_xO_yN_z$ stack. Etch of the silicon substrate followed to form a ledge so that a standard fiber with cladding could be moved as close as possible to the input facet of the coupler with steps in (E).

Three masks were used in the fabrication process with dies' dimensions of 1 cm x 1cm. The first level mask is for patterning the silicon etch stop above the waveguide and the first set of alignment marks. The Nikon *i*-line stepper that we use for optical lithography relies on these marks to accurately align the next pattern to existing ones on the wafer.

The second level mask defined the end of the taper stack that connects to the waveguide. The many variations of the coupler structure were drawn on this level. This mask also contains an additional set of alignment marks. The last mask level defined the back end of the taper which determines its length and radius of curvature for the facet lens. This mask could be aligned by marks of either previous level.

10.2 Deposition of waveguide film, silicon etch stop and pattern of level 1

We started the process with 6-in silicon wafers that had been oxidized to form a 3 μm thick oxide film. The $Si_xO_yN_z$ waveguide core was deposited by PECVD in Applied Materials Centura reactor with SiH_4, N_2O and N_2 precursors. The waveguide film is 880 nm thick with index of 1.72 measured at 630 nm wavelength.

In the following steps, we grew a 150nm thick silicon layer as etch stop to protect the waveguide structure. The silicon film was deposited by LPCVD at 625°C. The film was then patterned with the 1st mask and etched in He/Cl_2 plasma. The silicon etches would stop on the $Si_xO_yN_z$ surface due to high etch selectivity. We had defined the waveguide width of 0.9 μm with this etch process.

10.3 Formation of the vertically asymmetrical tapers

10.3.1. PECVD of the asymmetrical $Si_xO_yN_z$ film stack

As mentioned in the coupler design, light from the fiber is confined vertically by an asymmetrical step-wise parabolic index profile. We can deposit $Si_xO_yN_z$ films at different indices to form a step index profile with PECVD technique. In our design, the bottom layer has index of 1.70 and the top layer has index of 1.52. We chose a design of 7 step-index layers because FDTD simulation results verified that a 10-layer structure at the same total thickness only has the coupling efficiency 0.02 higher. The bottom waveguide thickness is 900nm while each subsequent layer is 850nm. The total stack is 6 μm thick.

We deposit the film stack by PECVD in Applied Materials Centura chamber. The index is varied by adjusting the flow of SiH_4 and N_2O. The layers from 2 to 7 are deposited on top of the waveguide layer and the poly silicon etch stop. All the $Si_xO_yN_z$ deposition recipes had to been calibrated to yield on-wafer thickness non-uniformity < 1.5 % and index non-uniformity < 0.015.

The 6 μm stack of $Si_xO_yN_z$ films has high compressive stress. Since PECVD only deposits film on one wafer side, the wafer is bowed. The amount of bow is around 125 μm. We compensated the front side bow with deposition of PECVD oxide on the back of the wafer. One thing that we need to be cautious is that a thick backside film can hinder wafer processing in later steps. The reason is that after the front side $Si_xO_yN_z$ layers are removed, the wafer will bow in the reversed direction due to the oxide film on its back.

As a result, we only deposited a 4 μm of PECVD oxide in the back to reduce the wafer bow to 60-70 μm. After the front-side film was etched to create pattern of the 2nd mask, the wafer bow was measured at around 60 μm in the reversed direction.

10.3.2. Improving lithographic alignment of coupler and waveguide

To confine the light in the lateral direction, a combination of taper and lens is used. The taper was defined with this level 2's mask while the lens at the fiber-end facet will be patterned in the next. The wafers with the $Si_xO_yN_z$ stack were deposited with 1.2 μm of LPCVD silicon as hard mask. PR was used to pattern the silicon mask. The pattern of level 2's was applied using alignment marks on the first level.

We observed that in many wafers, the misalignment was large enough to be visible under the microscope. For example, for the structures in the picture on the left, we estimated that the misalignment is an unacceptable 0.8 μm. This misalignment is larger than half the waveguide width. As a result, coupling efficiency would be significantly reduced.

To correct the problems, we need to make the alignment marks more prominent so that they could provide stronger diffraction signal. First, we increased the thickness of the alignment mark so there would be a higher contrast between these LPCVD silicon structures and its $Si_xO_yN_z$ background as illustrated in the Figure X-2A below. The new silicon etch stop would be 0.25 μm thick. In addition, we increased the number of dies sampled in the alignment process. For the previous alignment process, the number of dies used had been 7 and most of them situated near the center of the wafer. We

increased the number of dies inspected to 20 by adding dies further away from the center. The combination of thicker alignment marks and increased number of sampled dies improved the accuracy and consistency of alignment as observed in the microscope images of Figure X-2B below. We would check for misalignment with higher resolution SEM after completing the etch process for the $Si_xO_yN_z$ stack.

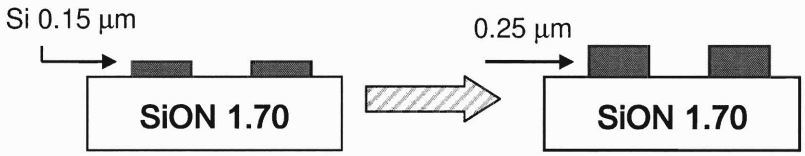

(A)

Figure X-2. (A) Improving the layer alignment accuracy by increasing the thickness of the silicon layer. Thicker silicon marks would enhance contrast with respect to $Si_xO_yN_z$ background. (B) Alignment is more accurate and consistent following application of techniques as observed my images taken from microscope.

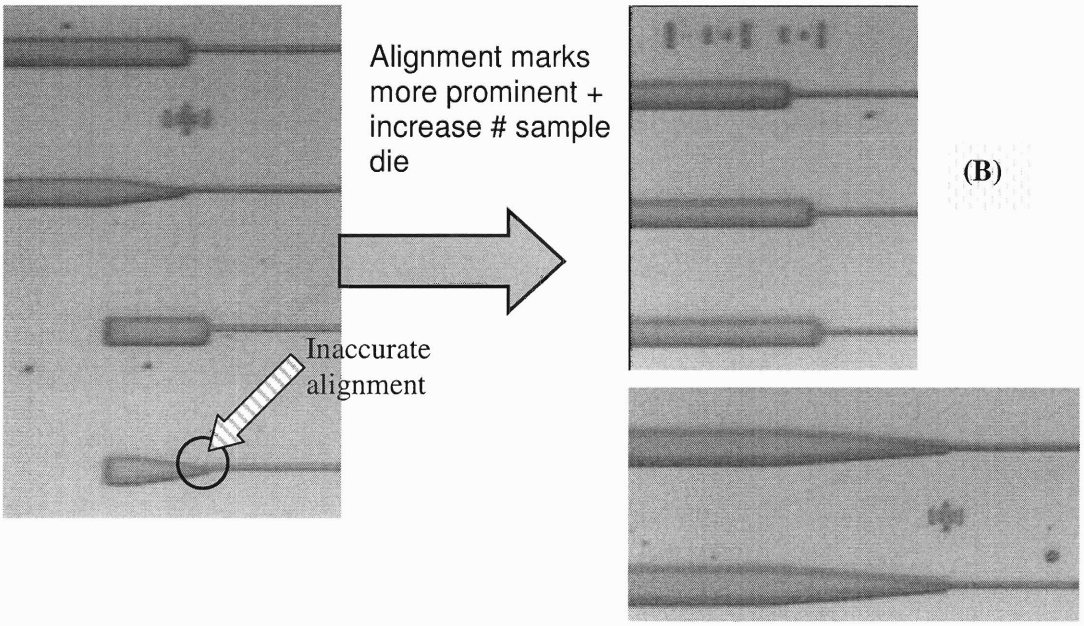

10.3.3. Etching thick $Si_xO_yN_z$ to define the taper

We used silicon as hard mask for etching of thick $Si_xO_yN_z$ layers. We had shown in section 9.3 that for the same stack thickness of 6 μm, etching with a silicon hard mask would yield a better angle profile and smoother sidewall than a conventional PR mask. The silicon mask was patterned by plasma etching in LAM490B chamber with He/Cl_2 chemistry.

To minimize isotropic etching of dielectric, etching gas flow should not contain CF_4. We had developed two recipes for etching dielectric in the Applied Materials P5000 chamber that use only CHF_3 as etching gas as reported in chapter 9.3.5. The recipe at higher power and lower pressure etches with a faster rate and has sidewall's slope closer to 90°. However, the etch uniformity and selectivity to the hard mask are better at low power and high pressure at the same CHF_3 flow rate. Their properties are illustrated in Figure X-3.

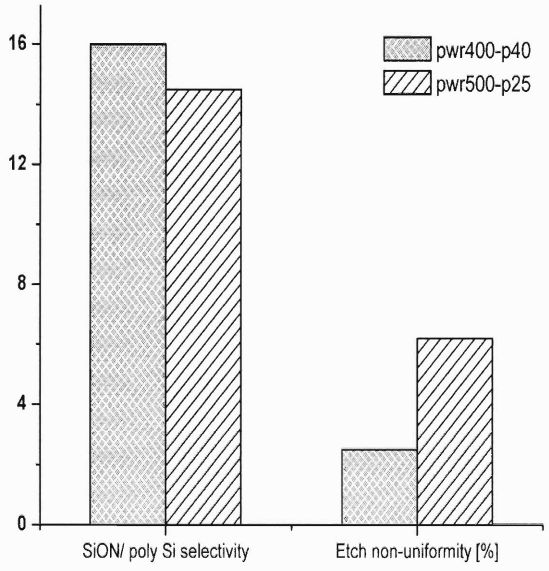

Figure X-3. Etch properties comparison shows that the recipe with lower power and higher pressure have better mask selective and on-wafer etch rate uniformity. However, the sidewall angle is reduced.

We combined these two recipes to etch our 6 μm $Si_xO_yN_z$ stack. Our goal would be to achieve good sidewall angle and have sufficient etch stop and hard mask protection throughout the wafer. 80% of the etching

process was completed with recipe of power of 500 W at 25 mtorr. The remaining materials would be removed by recipe of lower power 400 W and higher pressure 40 mtorr. The first recipe etches for 4 x 250-second intervals to a total of 1000 seconds. The second recipe etches for 2 x 175-second intervals to a total of 350 seconds. The SEM images of Figure X-4 reveal the shape of the couplers. On our mask, we have both taper-shape and box-shape structures.

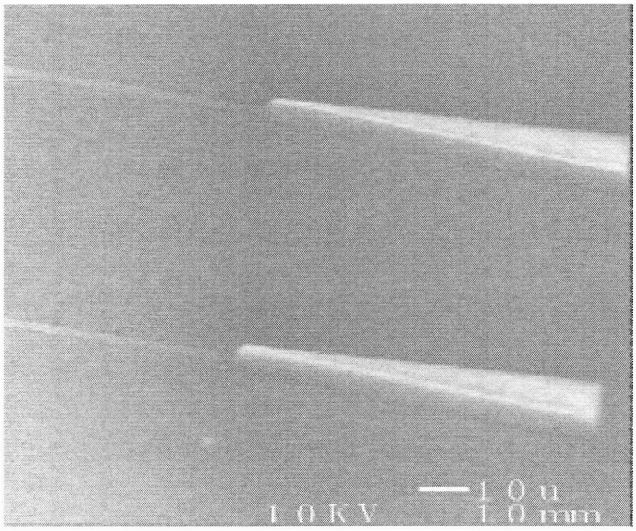

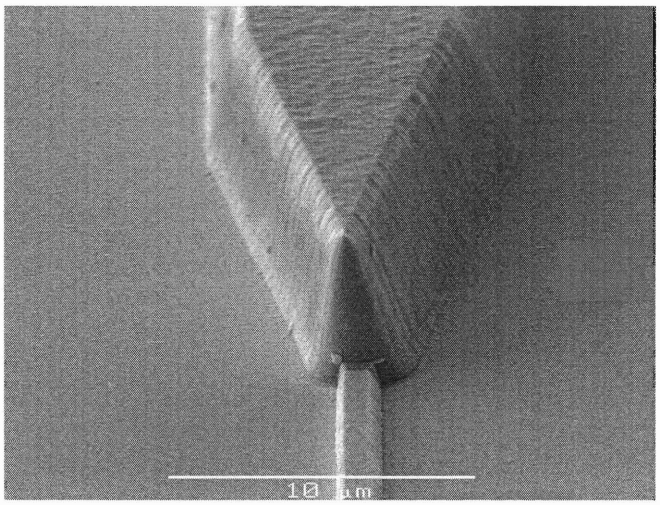

Figure X-4. SEM images of the unclad tapers defined by etching of $Si_xO_yN_z$ stack with CHF_3. The images reveal excellent alignment of the stack and the waveguide. The sidewall is smooth and stack profile angle is 78 degree.

We achieved a 78° angle for the sidewall. A consequence of the sloped sidewall is the overlapping of the stack's end to the waveguide's as seen in the SEM image in Figure X-5. In the SEM images, the tip of the stack and the waveguide touch while they are supposed to be 1.0 μm apart. We concluded that the slope extends the stack length by approximately 1 μm. The slope is the result of equipment limitation in ICL. A better angle profile can theoretically be achieved with higher bias power. However, our etching chamber does not have bias power above 600W. If conditions are permitted, we could explore the etching capability of outside vendors using thin silicon mask.

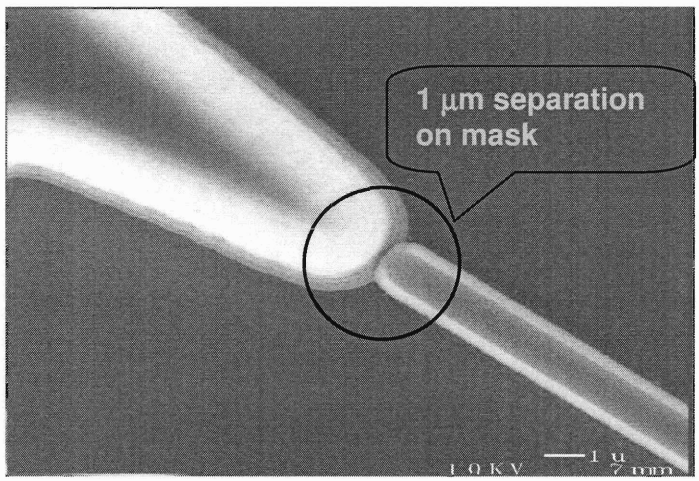

Figure X-5. SEM image shows effect of sloping profile. This test structure is designed to have a 1 μm gap between stack and waveguide on the mask. However, the structures overlap after etching.

10.3.4. Removal of silicon etch stop by selective etching

After the removal of 6 μm $Si_xO_yN_z$ film to form the tapered stack, the remaining poly silicon films from the etch stop and hard mask must be removed by selective etching. In ICL, there are two CMOS-compatible processes available for etching silicon. In the first process, He/Cl_2 plasma from the LAM 490B provides anisotropic etching of silicon at 60:1 selectivity with oxide and $Si_xO_yN_z$. The silicon etch rate is 300 nm/min. However, the ion bombardment can roughen up the top surface of the waveguide that leads to

higher propagation loss. In addition, since the process is highly anisotropic, we could not remove the silicon trapped under the nose of the sloped $Si_xO_yN_z$ stack as described in Figure X-6.

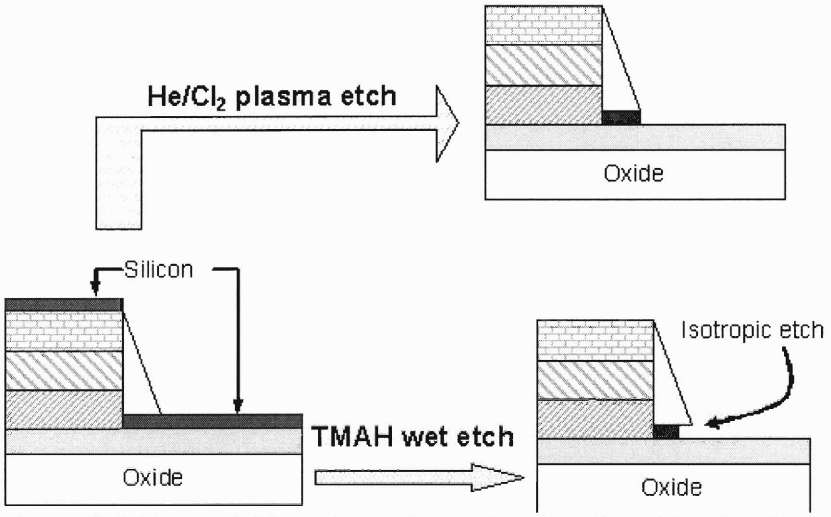

Figure X-6. Two available methods of removing thin silicon films in ICL are illustrated. Removal method that uses TMAH solution is a more preferred method because it doesn't cause damage to $Si_xO_yN_z$ surface and has high etch isotropy.

The 2nd method is using TMAH solution to remove silicon with more 150:1 selectivity to $Si_xO_yN_z$. The wet etch is more suitable to our process since it does not attack the top surface of the waveguide. The silicon etch rate is approximated at 1.5 μm/min. In addition, it is also isotropic and can partially remove the silicon trapped under the $Si_xO_yN_z$ stack's nose as seen in SEM images of Figure X-7 below.

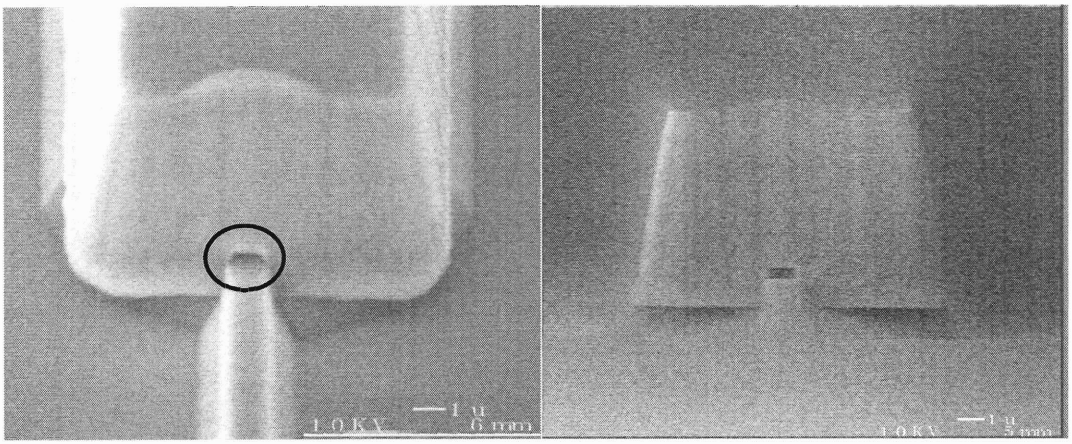

Figure X-7. SEM images of $Si_xO_yN_z$ stack on silicon substrate after TMAH etch indicate isotropic etching of silicon etch stop layer.

We experimented with both silicon removal methods. In our experiment at that time, the plasma etches in LAM490B proceeded fine while the silicon films on test wafer was impervious to TMAH etch. We could not solve that problem at the point. So, we decided to use plasma to remove silicon hard mask and proceed with fabrication since the coupling efficiency of our structure is independent to the propagation loss of the waveguide.

At a later time, we recognized the problem of TMAH solution not etching the silicon film was due to the polymer residue from CHF_3 etches. Since this polymeric film does not react with both HF and TMAH, it shields the native oxide from being removed in diluted HF. Therefore, the silicon reaction in TMAH cannot occur. We corrected this problem by processing the wafer in O_2 plasma, followed by dip in HF solution. After both the polymer and the native oxide films had been removed, the fast silicon etches in TMAH solution ensued smoothly. We did not see this inhibitive behavior in plasma etching since the plasma bombardment had removed both the polymer and native oxide films.

After the silicon mask and etch stop are removed, a 9 μm PECVD oxide film was grown as upper clad. We also deposited an additional 2 μm of oxide in the wafer's back to compensate for the wafer bow.

The 6 μm etching of $Si_xO_yN_z$ to define the tapering shape had formed high steps on the wafer's surface. The deposition of 9 μm oxide and silicon mask changes the on-wafer topography little since both processes form conformal films. The wafer has dielectric films that total to 18 μm thick at the peaks and 12 μm thick at the valleys.

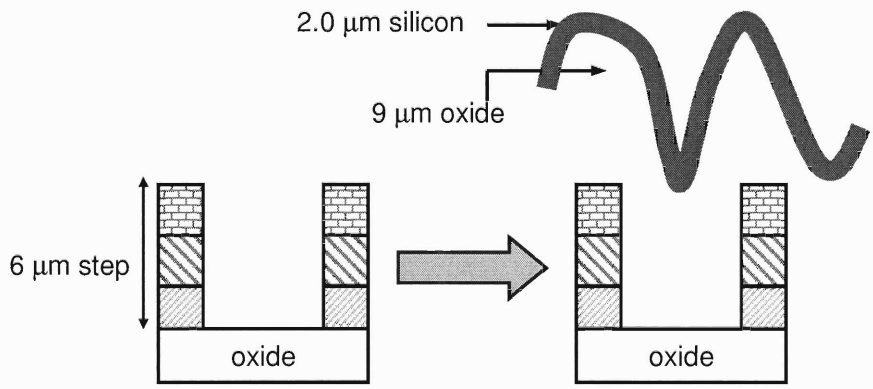

Figure X-8. Schematic illustration of the wafer topography after thick oxide upper clad was deposited. The peaks and valleys were formed by etching $Si_xO_yN_z$ stack.

10.4 Defining the coupler's length and lens shape with the 3rd mask

10.4.1. Advantages of defining coupler's length with lithography and etching

Level 3 mask defines the taper's length and also the radius of the planar lens in some structures at the end facets of the coupler. To define the end facets by lithography process is more advantageous to die saw and then back-polishing for its precision, accuracy and smoother facet. First, lithography is much more precise because the alignment error of optical lithography is less than 0.5 μm while die saw placement error is approximately 100 μm. Polishing the chip is also not accurate because the polishing rate cannot be well calibrated due to its dependence on many factors such as the conditions of the pad, the down pressure. Second, the die saw creates micro-cracks and scratches, and bumps that scatter light significantly at the facet. Our current polishing setup can only improve light coupling capability minimally. Plasma etches, on the other hand, will form a smooth sidewall. At a smooth facet, the light scattering is significantly reduced and the coupling efficiency is improved.

The process flow is detailed below. After the dielectric etch is finished, the silicon substrate is then etched to form a ledge to accommodate for moving the fiber as close as 1 μm from the coupler facet. Since a standard single mode fiber has 80-100 μm cladding diameter, we need to clear a minimum 50 μm of silicon substrate for the fiber to not bump into and cause damage to the chip facet and fiber's end during measurement.

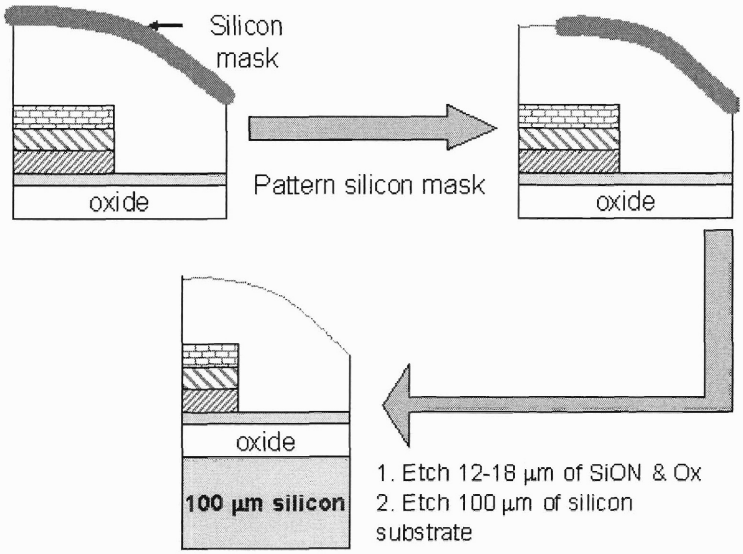

Figure X-9. A schematic illustration of the process flow that defines the input facet of the couplers is shown.

10.4.2. Improving alignment capability through thick silicon mask

We encountered alignment problems in the process of patterning mask of level 3 using Nikon stepper lithography. Each die has two sets of marks from patterning of previous mask levels as illustrated in the drawing below.

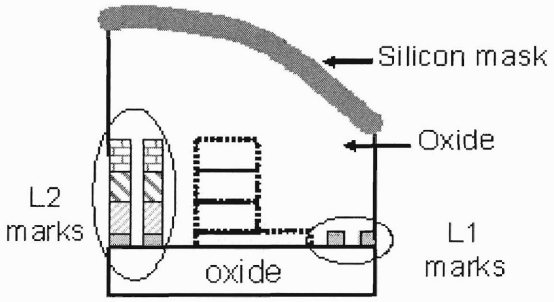

Figure X-10. Relative heights of two sets of alignment marks with respect to the couplers are shown.

The 1st set of alignment marks from the waveguide layer was not recognized by the stepper because it is only 0.9 μm thick and buried deep under oxide and silicon layers. In addition, that the stepper could not obtain focus for the 2nd set of alignment marks due to its 6 μm step height. We had to re-create the 1st level marks so that the stepper could recognize them. The strategy was to transfer

the alignment marks from the lowest layer to top of the oxide cladding before silicon mask was deposited. The modified process flow is illustrated in Figure X-11.

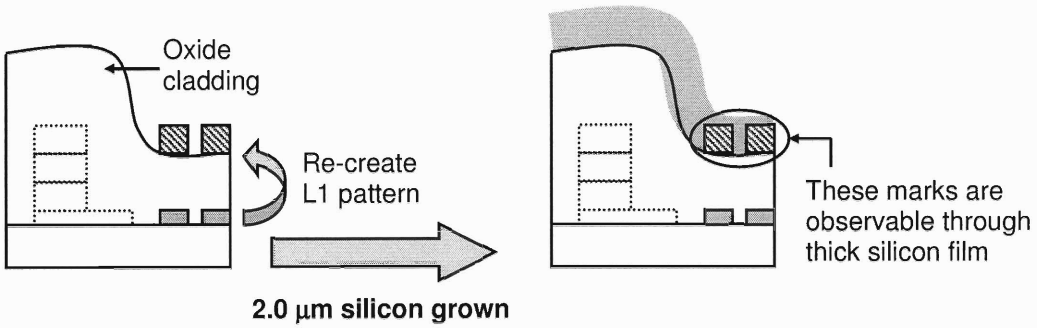

Figure X-11. Re-printing of alignment marks on the top oxide cladding enhances their chances of being detected through thick silicon film.

The pattern of level 1 was re-printed on top the oxide upper clad. It was then etched 0.8 μm down. The PR was removed and 2.0 μm of the poly-silicon was grown by LPCVD on top. The stepper recognized the marks and level 3's mask was patterned.

However, we encountered a different problem with insufficient PR coverage at high points on the wafer. The high points on the wafers are 6 μm high $Si_xO_yN_z$ stacks that require PR protection when the silicon mask is etched. Even when using in the *sts* system with silicon/PR selectivity > 15:1, we still did not have enough PR coverage for etching 2.0 μm silicon film with our current PR deposition technique. Since there is not a silicon mask on top of the taper, the whole stack is etched as seen in the SEM images of Figure X-12.

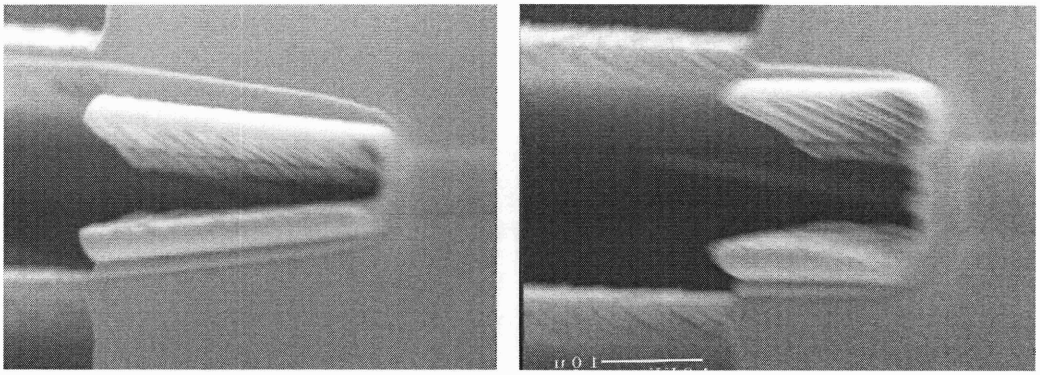

Figure X-12. SEM images reveal $Si_xO_yN_z$ stacks being etched due to insufficient PR coverage at wafer's high points. Planarization of the 6-μm high oxide bump is required before level 3's pattern is printed.

We can deposit thicker PR (> 10 μm) with the coater system in the Technology Research Lab (TRL). However, the critical dimension increases with thick PR. Since our structures vary in micron scale, the large critical dimension will restrict us from fully investigating the coupling efficiency variation with physical parameters.

10.4.3. Etch process to define the fiber input facet

To solve the problems derived from the 6 μm step height of the stack, chemical mechanical polishing of the oxide upper clad is the solution. Since the 6-in CMP system at MTL did not work at the time, our wafers were planarized at Lincoln Lab. When returned, the oxide field was measured at 12 μm thick and the step height was reduced to 0.3 μm. The wafers was readied to be coated with the silicon mask and printed with mask of level 3.

After the level 3's mask had been printed and silicon mask was patterned, the dielectric film in the open field was etched in Applied Materials P5000. The etching recipe was the same lower power, high pressure recipe used in stack definition of level 2. The silicon

substrate was subsequently etched to form a ledge to accommodate the single-mode fiber. Part of the oxide upper clad was used as hard mask for silicon etching. In the standard recipe that we used for silicon etching, the system alternates between depositing C_4F_8 polymer to protect the sidewall with silicon etch by SF_6. The etch cycle is 14 seconds while the polymer coating cycle is 11 seconds. The etch rate is ~1.7 μm of silicon/min for our pattern. Our total etch time was 50 minutes. Approximately 1 μm of oxide mask was consumed.

As observed from the SEM images of Figure X-13, the lens shape at the end facet is defined at a 76° angle in the dielectric top. The silicon substrate's strata formation is due to the alternation between etching and polymer deposition cycles. We measured a 100 μm step height from the top of oxide to the silicon base. The oxide thickness is 11 μm. We still have sufficient oxide upper clad for the $Si_xO_yN_z$ coupler structures.

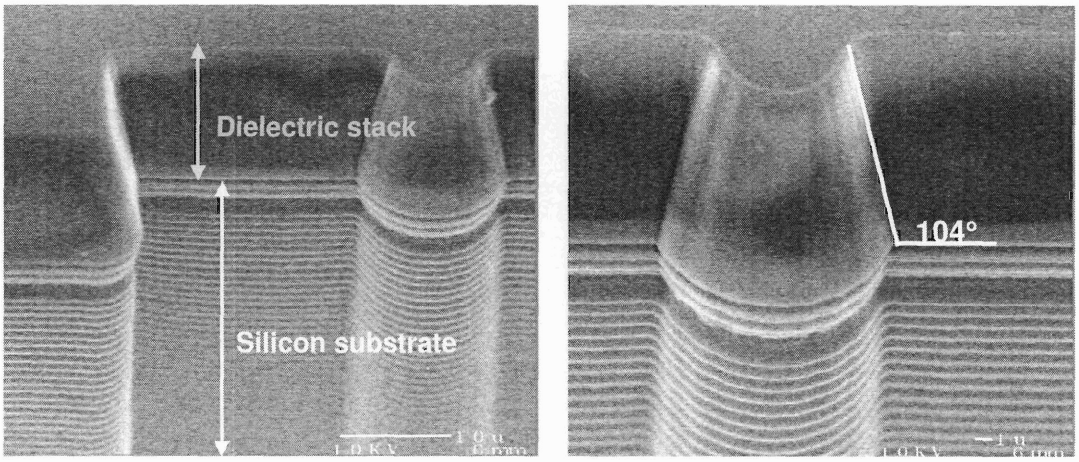

Figure X-13: The SEM images show fiber input facet of the coupler structure. The silicon substrate is etched down 100 μm to form a ledge that brings the fiber in very close to the coupler. The slope sidewall is due to the low power dielectric etch recipe. The sidewall is very smooth to have minimal scattering loss at the input interface. The oxide clad's roughness does not affect device performance.

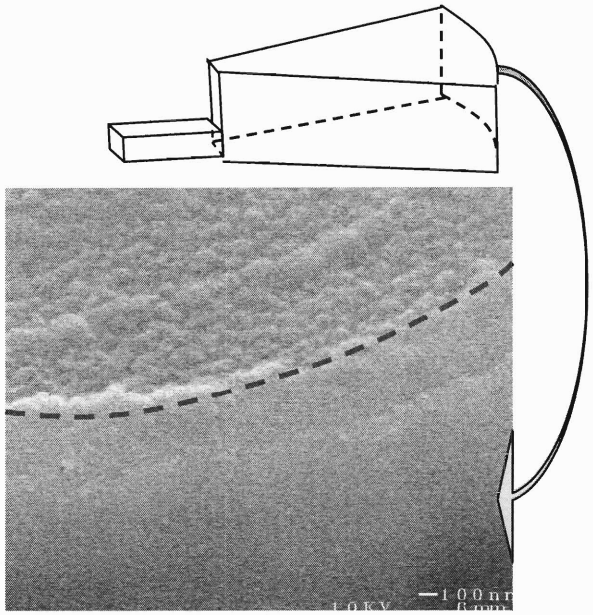

Due to the ion bombardment during silicon etching, top of the oxide clad is much rougher than the facet sidewall. Roughness on top of the oxide will not affect the performance of the couplers. Since the sidewall is very smooth, we can expect that the scattering at the facet is low. With the silicon ledge formed, the fiber can move very close to the coupler's facet without bumping into and damaging its core during measurement. The last processing step was to die saw the chip anywhere in the ledge to have a sample that fits on the vacuum stage of the Newport Auto Aligner station.

Chapter 11: Optical Characterization of Fabricated Couplers

11.1. Setup for measurements of coupling efficiency

After the couplers had been successfully fabricated, their power throughput was measured and coupling efficiency was calculated. The measurement system is the Newport Auto Aligner station that measures direct throughput power. Single mode fibers are used to guide light from the laser source to the input facet and from the output facet to the power meter. The fibers' placements to the coupler are optimized in all three directions to yield maximum throughput. A schematic of the measurement setup is shown in Figure XI-1.

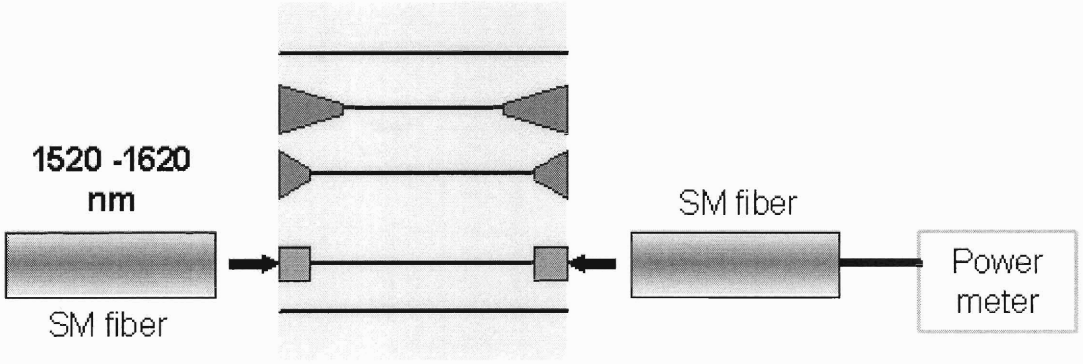

Figure XI-1. Schematic of the Newport Auto Aligner setup for measuring power that transmits through the coupler is shown. Single mode fibers SMF28 and Nufern980 were used in measurements.

The maximum throughput power of the station was calibrated by connecting input and output fibers with index-matching fluid. This maximum power has accounted for all internal loss of the system. The coupling efficiency of the device is calculated from the throughput power of our coupler devices minus the reflection losses at the interfaces and the propagation loss in the waveguide. For the 1st set of experiments, we used Nufern980

fibers with an MFD of 6.8 μm. The MFD of this fiber is close to the thickness of the stack to optimize the vertical confinement. However, we can also use same structures to couple light from the larger diameter SMF28 fiber as we did in the 2nd set of measurements. A future design that optimizes vertical light confinement from SMF28 fiber should have its stack thickness near equal to the fiber's diameter of 10 μm.

Index matching fluid reduces reflection loss at the fiber-coupler interface. When an index-matching fluid of 1.46 is used between the fibers and chip, the power reflectivity at the interface is very small. If there is an air gap between the fiber and chip, there will be reflections at both fiber-air and air-coupler interfaces. The transmission coefficient is only 0.90. We also had calculated the propagation loss of the waveguide between the structures. The propagation loss for a 1 cm long waveguide is 4.8 dB, measured by Fabry-Perot resonant and cutback methods in section 6.2. Since we have two symmetrical structures at both sides of the chip, we assume they have equal coupling efficiencies due to the reciprocity properties of the propagating wave.

11.2. Baseline measurements: fiber to fiber and fiber to waveguide direct coupling

11.2.1. Throughput power for fiber-to-fiber direct coupling

To calculate the maximum throughput of the system, we connect the input and output fibers with index-matching fluid and optimize alignment of the cores. We obtained slightly different throughput powers for Nufern980 and SMF28 fibers. The power throughputs of different setups are listed below.

Setup	Power throughput
SMF28 –SMF28	485 μW
SMF28 – IMF=1.46- SMF28	525 μW
Nufern980 – IMF=1.46- Nufern980	485 μW
Nufern980 – IMF=1.74- Nufern980	455 μW

Table XI-1: Maximum throughput power obtained through the Newport station with different connecting fibers.

11.2.2. Throughput power for fiber-to-waveguide direct coupling

Throughput power for fiber and on-chip waveguide direct coupling is theoretically estimated via overlapping integral of Gaussian beams Γ:

$$\Gamma = \frac{\int_{-\frac{W_x}{2}}^{\frac{W_x}{2}} \int_{-\frac{W_y}{2}}^{\frac{W_y}{2}} e^{-2\left[\frac{x^2+y^2}{W_0^2}\right]} dxdy}{\int_{-\infty}^{\infty} \int_{-\infty}^{\infty} e^{-2\left[\frac{x^2+y^2}{W_0^2}\right]} dxdy}$$

With W_0= 3.5 μm for a Nufern980 fiber and W_x=W_y=0.9 μm for our on-chip single-mode waveguide, the overlapping factor Γ is 0.0435. If the on-chip waveguide is 1-cm long with propagation loss of 4.75 dB/cm, the theoretical transmitted power is **8100** nW. We measured values between **7700 ±150** nW on our system which indicates very low scattering loss at the facets. Similarly, if a SMF28 fiber is used in the setup, the overlapping factor is 0.0211 since less power is confined at the center. The theoretical power throughput is now **3650** nW. The measured values is **3500 ± 200** nW.

11.3. Variation of focal length due to sloping effect and IMF

11.3.1. FDTD simulation results for fabricated couplers with sloped sidewall

For our initial design of the asymmetrical step-wise index stack, the 2D FDTD simulations indicate the highest coupling efficiency at focus length of 19.5 μm. The structures in those simulations have perfect sidewall angle of 90° and the fiber is launched right at the input facet.

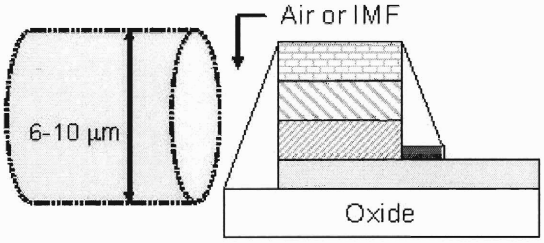

A fabrication constraint that will affect the coupling efficiency is the dielectric stack slope created during plasma etching. As observed in the SEM pictures in chapter 10.5, we have a 76° slope. For a 6 μm thick $Si_xO_yN_z$ stack etched in the P5000, the coupler's length at the bottom is 1.5 μm longer than at the top. Due to the slope, there is a gap between the fiber and the coupler structure. Index matching fluid can fill the gap and lower the reflection loss at the interfaces.

We need to re-simulate with 2D FDTD the propagation in these structures taking into account the sloping profile. We ran simulations for three scenarios. In the first scenario, we have only the air gap in between structures. The other twos, we use index matching fluid at 1.46 and 1.75 to fill the gap. From the FDTD outputs, we calculated the coupling efficiency with adjustment for reflection loss.

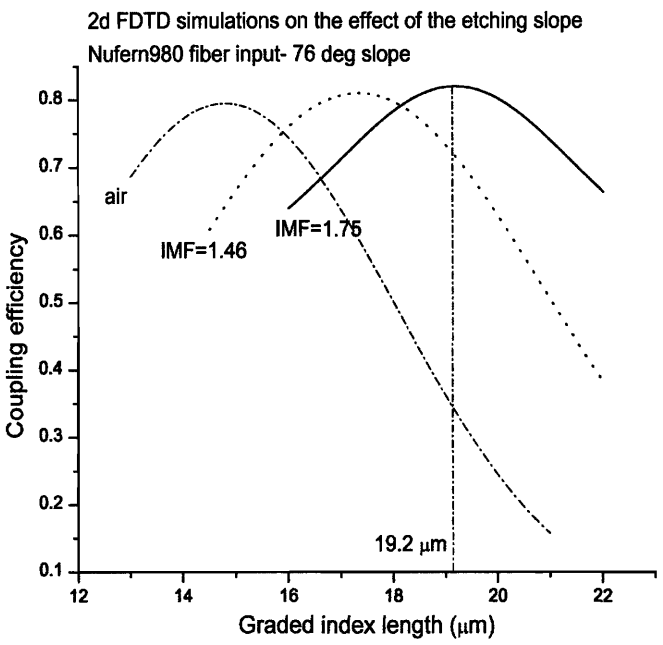

Figure XI-2. 2D FDTD simulations taking account for the sloping profile indicates the same maximum 0.81 efficiency for Nufern980 fiber with or without IMF. The focal distance increases with index of IMF.

From Figure XI-2, a maximum of 0.81 coupling efficiency in the vertical plane is recorded for Nufern980 input fiber. This value is independent to the index matching fluid used. However, the focal length of the stack is strongly influenced by IMF. When there is an air gap between the structures, the focal length is at 15.5 μm. It increases to 17.5 μm and 19.2 μm when IMF=1.46, 1.75 are used respectively. The reason is that with the air gap, the index contrast at the coupler interface ($\Delta n = N_{coupler\_eff} - N_{background} = 1.63 - 1.00 = 0.63$) is higher than when index-matching is used ($\Delta n = N_{coupler\_eff} - N_{background} = 1.63 - 1.46 = 0.17$). The focusing length of a GRIN lens is reversed with the index contrast at the interface.

The efficiency for a 3D structure is the product of the efficiencies obtained from 2D FDTD simulations on each plane. We confine the light horizontally by a linear non-adiabatic taper whose efficiency depends on the tapering angle. At constant input and output width of 8 μm and 0.9 μm, the efficiency for a 15 μm long taper is calculated to be 0.75 from 2D FDTD. It increases to 0.79 at L=17.5 μm and 0.81 at L=19.5 μm. Taking

into account the efficiency on the horizontal plane, the efficiency is highest for coupler structure at 19.5 μm long as seen in Figure XI-3.

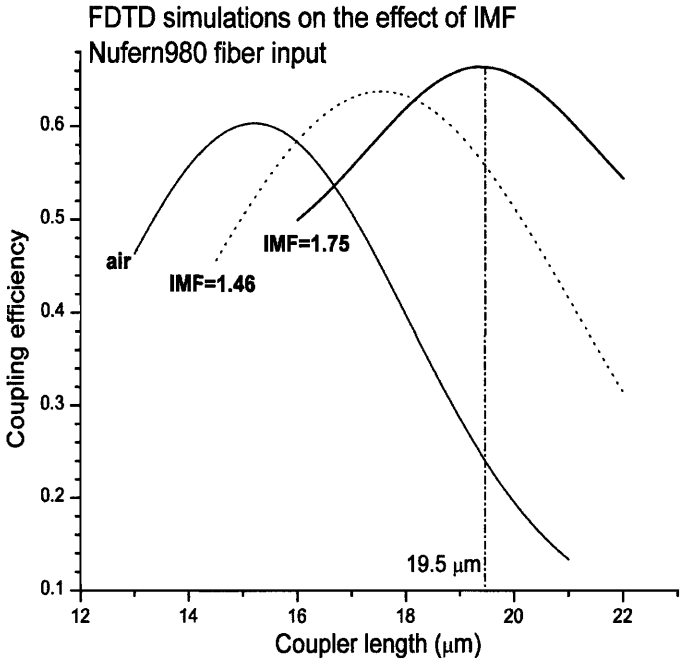

Figure XI-3. Theoretical coupling efficiency calculated for our 3D structures shows highest efficiency obtained at 19.5 μm when IMF= 1.75 is used. The efficiency of a horizontal non-adiabatic taper is higher at longer distance.

11.3.2. Experimental coupling efficiency as a function of coupler's length

By using optical lithography, we can study the efficiency's variation with couplers' dimensions by measuring different devices on a same chip. The shift in the focus length with index matching fluid has been observed in the measurement data for our fabricated coupler structures. We first present the measurement results obtained when measuring input from Nufern980 fiber with IMF=1.75 used. All the structures in this experimental set have the same input width of 8 μm and their length varies around our bull-eye design length of 20 μm. The experimental coupling efficiency is compared with theoretical results obtained from effective FDTD calculations.

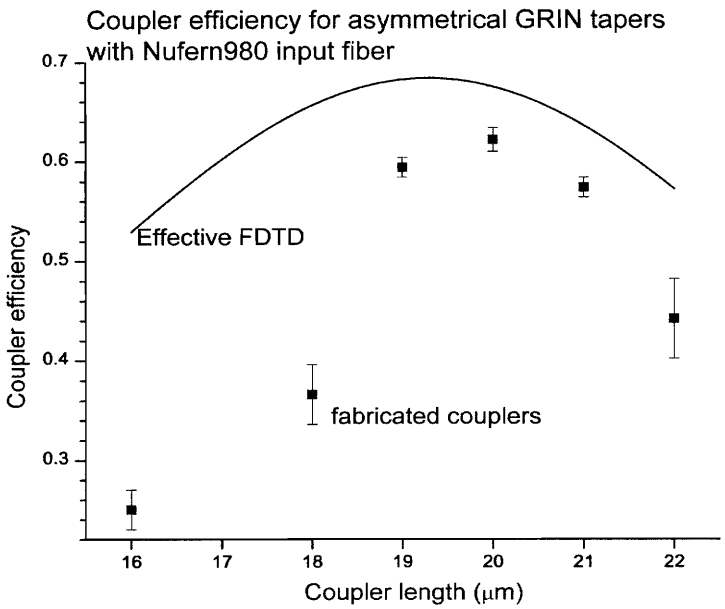

Figure XI-4. A comparison, of the experimentally measured coupling efficiency and effective FDTD simulations, shows similar variation with structure length. Highest coupling efficiency of 0.61 (2.2 dB loss) is achieved at a coupler length of 20 μm.

We obtained a highest **0.61** coupling efficiency (**2.2 dB insertion loss**) at L= 20 μm for Nufern980 input fiber. A 1-μm variation of the coupler's length reduces the efficiency by only 0.05. Although the structures had gone though many process steps, experimentally measured coupling efficiencies at different lengths are closely matched by results obtained by FDTD simulations. The simulation results represented as the solid line in Figure XI-4, display a self-focusing effect at focal length of 20 μm. We observe from that figure that the highest coupling efficiency is measured on structures of length L=20 μm. Measured coupler efficiencies are smaller for structures of length shorter or longer than 20 μm. However, we also obtained the efficiency of 0.61 at coupler length of 58 μm due to self-focusing effect of the GRIN stack.

Although the light enters the input stack at its midpoint, which is above the waveguide layer, the parabolic step-wise GRIN structure gradually transforms the mode and couples it into the waveguide. Very near the end of the stack, the maximum power of the modal

distribution is still located above the waveguide for shorter devices. Since there is a vertical offset between this maximum and the center of the waveguide, not all light is guided into the waveguide. The 2D coupling efficiency in the vertical plane is not optimized. In addition, shorter linear tapers have sharper tapering angles that cause more radiation loss in the horizontal direction. The combination of these two effects results in lower coupling efficiencies for structures with lengths shorter than the focal distance.

A similar effect in the vertical direction is observed for couplers longer than 20 μm. Due to the effect of self-focusing, the maximum power of the modal distribution moves upward within the waveguide, after light propagates past the focal point. As a result, less power is coupled into the waveguide.

11.3.3. Effect of the silicon remained at the top of the coupler

Another fabrication constraint that we have is the ability to remove the silicon remained under the nose of the SiON stack at the waveguide facet of the coupler. As seen in the schematic drawing on the left, a 1.0 μm nose is formed after 6 μm of etching. The plasma removal of silicon film is very anisotropic which leaves a 0.25 μm high, 1.0 μm long silicon strip under the stack nose.

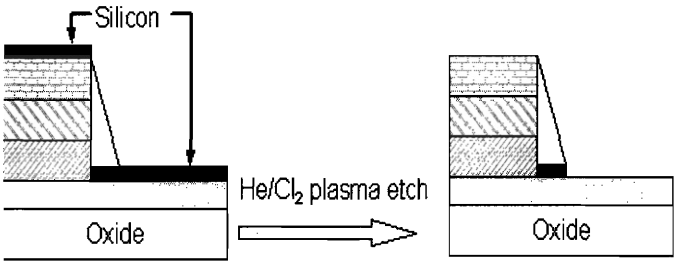

Figure XI-5. Schematic of silicon mask removal process with He/Cl_2 plasma. The anisotropic etch left a thin film of silicon underneath the tip of the dielectric stack.

Although we can assume low absorption loss from the silicon loss due to its small dimension, this high index silicon strip will prevent the light from converging to the waveguide under it. How much the silicon changes the efficiency depends on the length of the structure. As observed in the 2D FDTD simulation results, if the coupler's length is near or slightly longer the GRIN focal distance of 20 μm, the effect is minimal since most of the light is already converged underneath. If the coupler's length is shorter, the effect is more detrimental since the silicon layer prevents the light from converging down to the bottom waveguide.

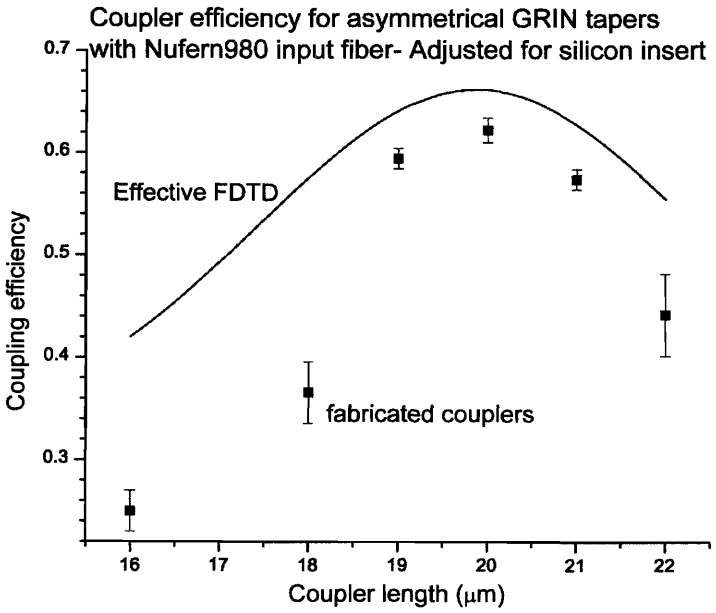

Figure XI-6. Theoretical FDTD curve adjusted for silicon film insertion. The curve displays a better fit to the experimentally measured data at device's length far away from focal distance.

Using the new FDTD simulation results, we adjusted the theoretical effective FDTD curve in Figure XI-6. The new curve shows a better fit to the experimentally measured data at device's length far away from focal distance.

11.4. Effect of input width on the coupling efficiency

The coupling efficiency is also studied as a function of the input width of the tapers. Figure XI-7 shows the variation in coupling efficiency as a function of the input width of coupler devices which are 20 μm in length. A maximum efficiency of 0.61 is measured

at an input width of 7-8 μm, a width which matches the mode field diameter (MFD) of the Nufern980 fiber. Couplers with input widths from 6 μm to 9 μm yield efficiencies that vary within 0.02 of the maximum value. For devices with input widths much smaller than the MFD of the fiber, the fiber mode is not well contained in the coupler stack. Therefore, coupling efficiency at smaller input widths is lower due to radiation loss into the cladding. At larger input widths, the efficiency is again reduced due to radiation losses at sharper tapering angles, even though the entire fiber mode is well contained.

Figure XI-7. Coupling efficiency, both, measured from the fabricated couplers, and calculated from effective FDTD simulations, is high for input width which is close to the Nufern980 MFD (6.8μm) for structures 20 μm long.

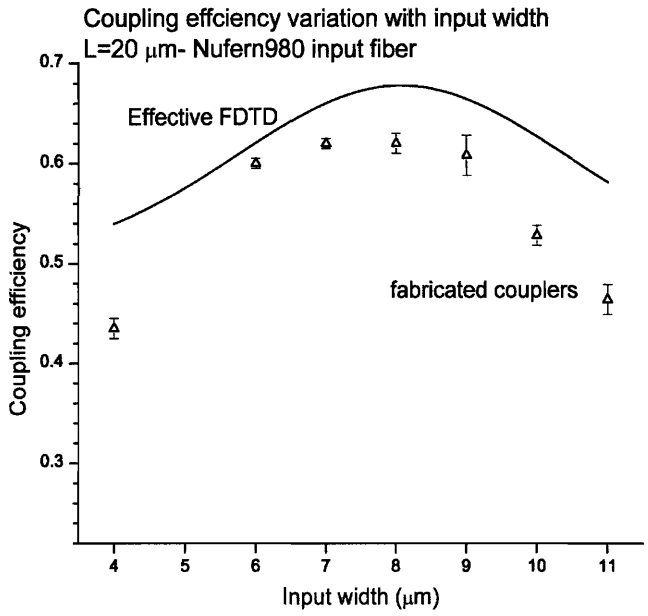

11.5. Effect of misalignment between the input fiber and the $Si_xO_yN_z$ stack

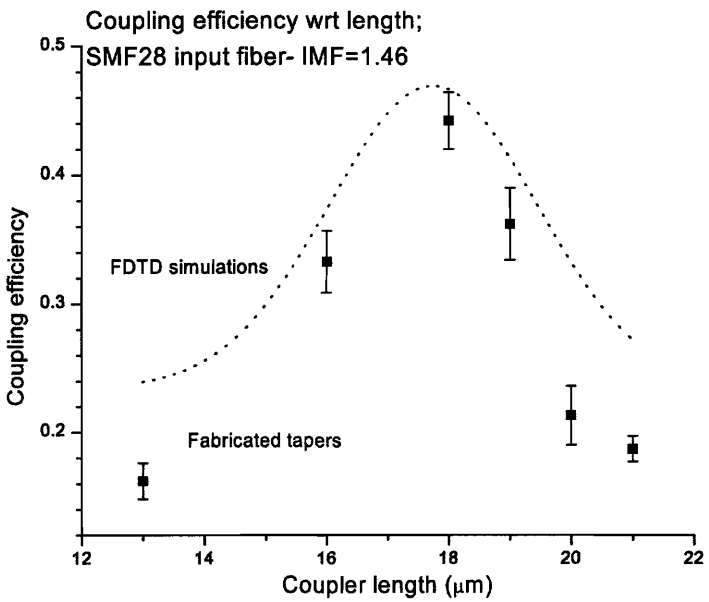

The effect of GRIN is again confirmed when IMF=1.46 is used with SMF28 input fiber. We achieved 0.45 coupling efficiency at coupler length of 18 μm. The FDTD simulation curve also follows the results well.

Figure XI-8. Similar trend with respect to length of the coupler is observed for SMF28 input fiber using IMF=1.46. Highest coupling efficiency of 0.45 is achieved at focal length of 18 μm.

The maximum power throughput for each device is obtained when the alignment between fiber and device is optimized in all three directions. From FDTD, the optimized position for the fiber center is at the center of the taper horizontally and 3 μm higher than the waveguide vertically. The fiber end's z-position is 1-2 μm away from the device facet. Moving away from this point will cause power drop that will lead to lower coupling efficiency. To study the *XY*-plane misalignment between the input fiber and the coupler, we first optimized the output fiber is all 3 directions. Then, the input fiber is moved to a location only 1-2 μm away from the coupler's facet, and it is moved on X and Y-axis on two independent scans. The misalignment scans for an SMF28 input fiber to an 18 μm flat-end coupler are presented in Figure XI-9 below.

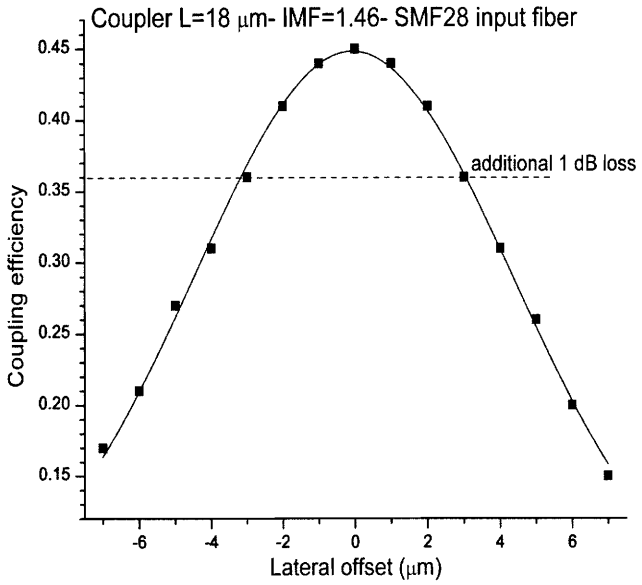

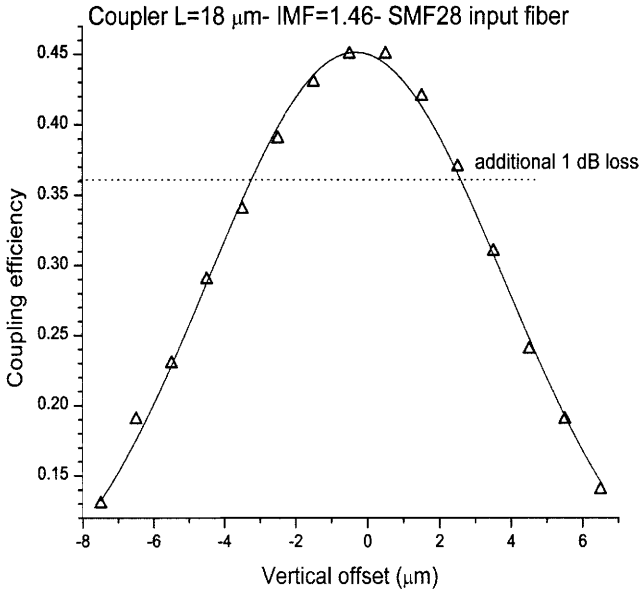

Figure XI-9. Misalignment scans on *XY* plane for SMF28 input fiber to the tested coupler. The lateral offset curve is symmetrical due to the tapered shape. The vertical scan is slightly asymmetrical due to the step-wise index profile.

The lateral scan follows a symmetrical Gaussian shape with an extrapolated radius of 9 μm. The highest coupling efficiency is achieved when the fiber's center coincides with the taper's center. When the fiber center is moving from this optimized position, more power is lost into the cladding. Since the taper and fiber half widths are 4 μm and 5 μm, at 9 μm offset, only the power in the fiber's evanescent tail is contained in the taper structure. An additional 1 dB insertion loss is incurred at offset of 3 μm.

The vertical scan has a slightly asymmetrical shape and smaller Gaussian radius which represent the asymmetrical nature of our GRIN design. We assume that the optimized vertical placement of the fiber is at the stack's center since we cannot observe their relative vertical positions with microscope. Because the lower bottom layers have indices close to that of waveguide, they have more important roles in vertical confinement. As a result, the efficiency reduces faster when the fiber moves up. For example, at +6.5 μm offset, the efficiency is 0.13 while it is 0.19 at -6.5μm offset as observed from the scan. An additional 1 dB insertion loss is incurred when the input fiber is moved 2.6 μm up or 3.3 μm down from its optimized vertical position.

11.6. Effect of horizontal planar lens

11.6.1. Mode transform by planar lens

A planar lens is used in combination with the non-adiabatic taper to transform the mode in the horizontal direction. The shape and curvature of the lens were defined by reactive ion etching with mask #3. To study the effect of lens radius to coupling efficiency, we designed taper structures with varying lens radius at length L=20 μm, which is the focal distance of a GRIN structure. The SEM images in Figure X-13 illustrate the input facet of the coupler that has an R=4 μm planar lens. The shape of the lenses were well defined for coupler with radius up to R=8 μm. Due to the resolution limits of optical lithography, we could not define the curvature of lenses with highest radii. These high-radius lenses are essentially flat-end. On the other hand, the minimal lens radius is equal to half the input width of the coupler. This coupler has a semi-circle at the fiber input facet.

The first contribution to coupling efficiency of the lens is the focusing effect as demonstrated in the 2D FDTD simulations shown in section 7.2. Our couplers have short length of 20 μm, which is more closely matched to the focal length of high-curvature, small radius lens. As a result, strongest focusing effect and highest coupling efficiency is achieved with minimal lens radius. 2D FDTD simulations have shown that the coupling efficiency increases by 0.05 when a radius lens of R=4 μm replaces a flat-end input.

The second benefit of the lens to the coupling efficiency is the matching with the curvature of in the incoming wavefronts of the fiber's guided mode. The single mode of the fiber will incur high loss at flat-end input facet because the curvature of the wavefronts changes abruptly. A planar lens will preserve the shape of the wavefronts as they enter the coupler. As a result, a coupler with a lens at the input facet will have higher efficiency. However, we cannot quantify this enhancement in coupling efficiency since curvature of the wavefronts cannot be accounted for in 2D FDTD simulations. 3D FDTD simulations are time-consuming and we do not have the computing power.

11.6.2. Effect of sloped input facet and index matching fluid

We had designed the length of test structures with planar lens to be 20 μm, which is the focal distance of the coupler's vertical GRIN with straight sidewall. However, due to the low power etching conditions, the focal length is at 18 μm as reported in section 11.3. Maximum efficiency of the GRIN lens is no longer achieved at 20 μm for light at 1550

nm. For example, coupler with length L=18 μm has **0.60** efficiency while at L=20 μm, the efficiency is reduced to **0.40**.

We had worked on two tentative solutions to solve this problem. The first is to use a high-index matching fluid to extend the focus length to 20 μm. As reported in section 11.3, the focal length is extended to 20 μm when IMF=1.75 is placed between the fiber and coupler. However, since the index of the fluid is higher than the effective index of the $Si_xO_yN_z$ stack of 1.63, light will enter from high to low index medium. As a result, the light is instead diverged by the lens. The trend of lens radius variation with coupling efficiency is reversed. We had experimentally observed this trend in our test structures. Highest coupling efficiency of **0.60** was recorded for coupler with high radius or flat-end. A coupler with a planar lens of R=4 μm has a coupling efficiency of only **0.38**.

The 2nd approach is to eliminate the slope of the dielectric layer with a different dielectric etching tool. Analog Devices engineers advised us to send the wafer out to Ulvac for the last dielectric etching step. Their process also uses a silicon mask 2.0 μm thick. With a profile angle close to 90° at the input facet, the GRIN focal length is 20 μm without using IMF of 1.75. The light enters the $Si_xO_yN_z$ stack from a lower index medium (RI=1.46) and the enhancement effect of the planar lens can be investigated. However, the samples sent to Ulvac took longer time to process than we had anticipated. We will include the results in an addendum of this thesis at a later time.

11.6.3. Efficiency at coupler length not optimized for GRIN structure

Figure XI-10 illustrates the effect of varying the lens' radius to coupling efficiency for couplers of L=20 μm and sloped input facet. The input width of the structures is 6 μm. Nufern980 input fiber and IMF (RI=1.46) were used. Highest coupling efficiency of 0.49 is achieved at smallest lens radius of 3 μm. At R=10 μm or flat end coupler, the efficiency is 0.38.

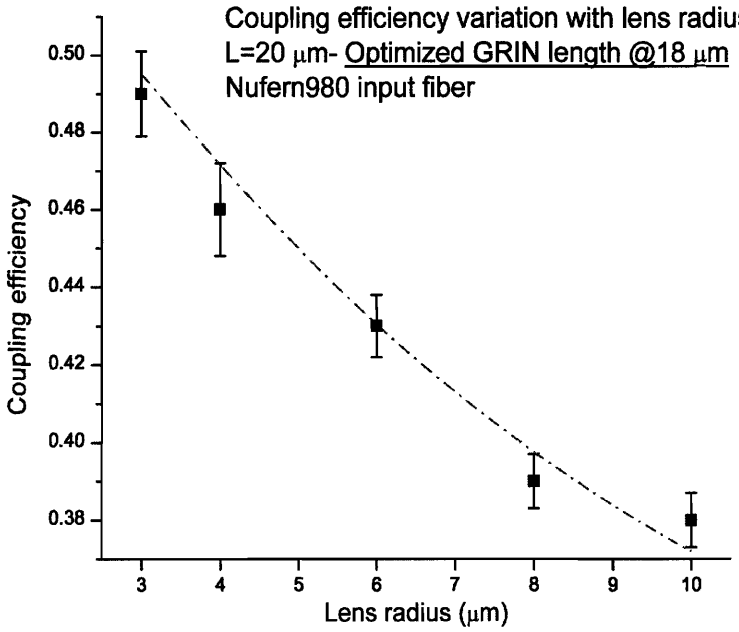

Figure XI-10. Variation in coupling efficiency with respect to the radius of planar lenses is shown. The improvement in coupling efficiency is due to both lens' focusing effect and by matching its radius to the curvature of the incoming fiber's guided mode.

The 10% enhancement in coupling efficiency is the result of both focusing effect of the lens and its ability to preserve the curvature of incoming wavefronts. From 2D FDTD simulations, focusing effect increases the efficiency by 5%. Since the wavefronts of the fiber's guided mode is not plane wave, but having radius of curvature, they have higher reflection loss at a planar mirror, in comparison to a curved mirror surface. To accurately calculate the difference in reflection loss in the two scenarios, 3D FDTD simulations are required. We do not have that capability. However, we can safely assume that the

remaining 5% coupling efficiency improvement is from the matching of the wavefront's curvature to the radius of the lens.

We are confident that we will achieve coupling efficiency of approximately 0.70 for our structures with lenses at the input facet when they have a straight input sidewall. The measured efficiency for a flat-end coupler is 0.60.

11.7. Coupling efficiency variation between 1520 nm and 1620 nm

We measured the insertion loss of our coupler structures when a JDS Uniphase tunable laser source was used to investigate their behaviors in C-band. We first performed the wavelength scan from 1520 nm to 1620 nm for two connecting Nufern980 fibers. This scan result is the internal loss of the system. The result is a relative flat curve near – 2.9 dB. The next scan was for a 1 cm long $Si_xO_yN_z$ waveguide directly coupled with Nufern980 fiber. The result is the total transmission loss of this coupling scheme that includes waveguide propagation loss and insertion loss from the fiber. If we subtract insertion loss of 12.5 dB, we obtain the propagation loss of the waveguide with respect to wavelength. The Fabry-Perot resonances were smoothed out and the loss curve is shown as the solid thicker curve in Figure XI-11.

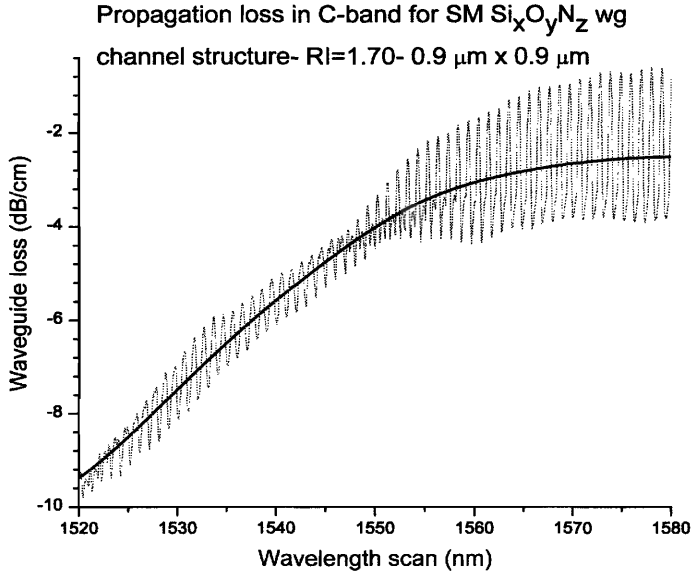

Figure XI-11. Propagation loss of $Si_xO_yN_z$ single mode waveguide with respect to wavelength in C-band is shown. The loss is highest at 1520 nm since the core material contains N-H bonds, which absorb strongest at 1510 nm.

The loss is much higher at 1520 nm because the waveguide core is PECVD $Si_xO_yN_z$ which contains N-H bonds. The peak of the N-H absorption curve is near 1510 nm and no absorption is observed for wavelength longer than 1560 nm.

The insertion loss of the couplers is the total insertion loss less the JDS Uniphase loss and waveguide propagation loss. The insertion loss of one coupler was calculated and presented in Figure XI-12.

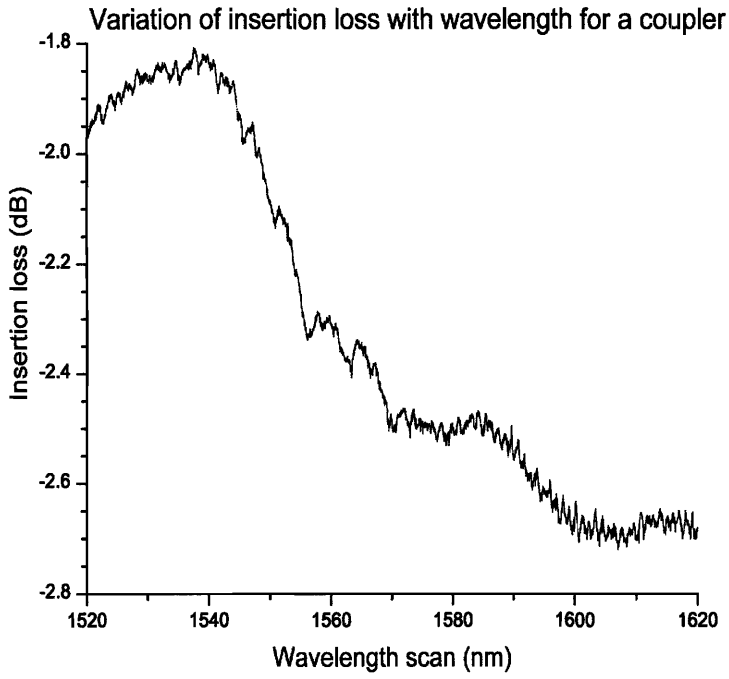

Figure XI-12. Insertion loss with respect to wavelength from 1520 nm to 1620 nm of our fabricated coupler structure shows small variation. The insertion loss was normalized to the wavelength dependent systems response.

Figure XI-14 displays the wavelength dependent response from 1520 nm to 1620 nm for our coupler structure.. The insertion loss at 1550 nm is 2.15 dB, similar to the results obtained in measurements with constant wavelength laser source. The lowest insertion loss of 1.85 dB, equivalent to coupling efficiency of 0.65, is achieved at wavelength near 1535nm. Then, the insertion loss increases with wavelength to 2.7 dB at 1620 nm. This loss is equivalent to a 0.54 coupling efficiency. Our fabricated coupler demonstrates excellent broadband properties with small variation of coupling efficiency in C-band.

This behavior of the coupler's insertion loss with wavelength reflects response of the vertical GRIN structure with wavelength. The confinement in the horizontal direction less sensitive to the wavelength since the input width of 8 μm is sufficiently large to

contain the all the guided mode of the fiber. The highest efficiency obtained at 1535 nm wavelength indicates that the focal length of the GRIN structure at 1550 nm is slightly longer than the length of the test structure. As a result, we can fine-tune the length of couplers in future work to obtain maximum coupling efficiency at 1550 nm.

11.8. Coupler efficiencies of box structures

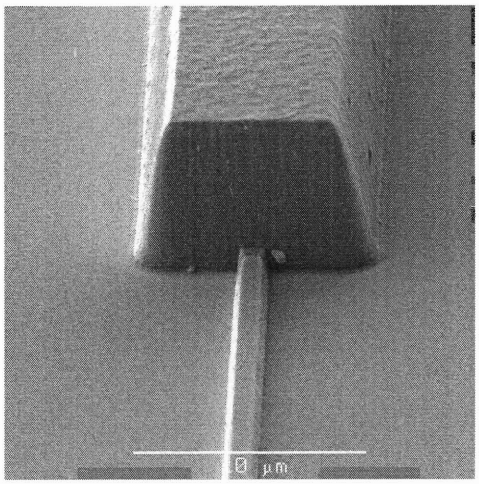

Besides using a linear taper to slowly confine the beam in the horizontal dimension, we also studied the efficiency of box shape coupler as seen in the SEM on the left. The box-shape coupler still has light confinement in the vertical direction and minimal light confinement horizontally. We observed the similar efficiency variation with box length and IMF. Highest coupling of **0.26 ± 0.02** is achieved for box structure of length 20 µm.

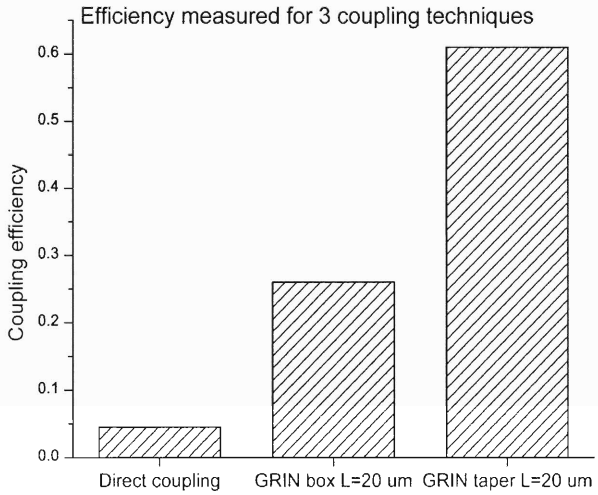

Figure XI-13. (Top) SEM image of an unclad box shape coupler connected to a $Si_xO_yN_z$ waveguide. (B) Experimentally measured data indicates the focusing effect in GRIN box coupler that results in efficiency higher than direct coupling.

11.9. Conclusions

We have experimentally demonstrated a compact, on-chip, fiber-to-waveguide coupler with a low insertion loss. The coupler, fabricated entirely by silicon-based processes is a 20 μm long and 6 μm high stack. It was then tested by coupling light from cleaved single-mode fibers to a sub-micron single-mode waveguide. We achieve a low insertion loss of 2.2 dB at 1550 nm for Nufern980 input fiber and 3.1 dB for SMF28 fiber. In addition, the coupler exhibits excellent broadband behavior with small variation of coupling efficiency from 1520 nm to 1620 nm. Our design combines an asymmetric step-wise GRIN profile with a linear taper to simultaneously confine the light in vertical and horizontal directions. The structure can achieve lower insertion loss via further optimization of the design and fabrication although it has already demonstrated good tolerance for fabrication conditions. Since we can vary the indices of $Si_xO_yN_z$ and Si_xN_y films, this robust design can be scaled to achieve similarly high efficiencies for coupling to waveguides of indices up to 2.2. In principle, the same coupling design can be used to guide light into Si or SiGe single-mode waveguide. However, obtaining materials with index variation from 2.2 to 3.5 is very challenging.

Chapter 12: Suggestions for Future Works

12.1. Summary of the thesis

I had presented in this thesis the works related to efficient routing of optical signal in silicon-based waveguides. Two sets of prototypes were fabricated and their optical characteristics were measured. The first set includes symmetrical multimode interference couplers for Si_xN_y single mode waveguides. The optical signal input is equally distributed to 4 and 8 waveguides at the output facet. The fabricated structures are compact and yield uniform output and high efficiency of 0.80. These devices can be incorporated into complex designs such as optical clock distribution, Mach-Zehnder switches and modulator. More complicated structures can be designed for wavelength division multiplexer applications.

The second set of devices includes fiber-to-waveguide couplers for $Si_xO_yN_z$ single mode waveguides. We have successfully realized a novel scheme which uses a vertically asymmetric step-wise parabolic index profile and a combination of a lens and taper to achieve simultaneous vertical and horizontal confinement. With compact structures of 18-20 μm long, we reduce the insertion loss of 12.5 dB for direct coupling to 2.2 dB. The design exhibits good broadband properties in spectral range from 1520 nm to 1620 nm. Improved processing will lead to coupling losses of less than 1.9 dB. The coupler design offers effective coupling for single mode waveguides of core indices up to 2.0.

We drew on the strength and knowledge of silicon-based fabrication technology to construct the efficient optical couplers presented in this thesis. By developing novel optical components with existing electronics manufacturing technology, we are one step closer to the realization of an integrated optical circuit.

12.2. Suggestions for future works

In chapter 3, we had developed PECVD recipes to deposit Si_xN_y films of index up to 2.25. We minimized the difference in absorption losses between 1310 nm and 1550 nm. However, the silicon-rich Si_xN_y material has a much higher slab loss at 1310 nm compared to N-rich, lower index Si_xN_y. So, future works are required to answer the question regarding the sources of loss at this wavelength. Some suggests that the loss stems from absorption of Si dangling bonds and/or from the scattering of silicon nanocrystals formed due to excess amount of silicon in films.

Future work is also needed in developing recipe or chemistry to deposit Si-rich Si_xN_y with better on-wafer uniformity and lower surface roughness. At high SiH_4 flow to deposit silicon-rich Si_xN_y, the plasma has strong edge effect where the index is much lower near the wafer's edge. As a result, new PECVD recipe or chemistry need to be developed to enhance the device's yield on the wafer.

In chapter 5 regarding the multimode interference couplers, we could not investigate the effect of device's height with coupling efficiency since 3D FDTD propagation is not available to us. So, future works should address that question. Also, the properties of

MMI with respect to wavelength need to be studied further. Future developments can use the developed knowledge to fabricate MMI devices with multiple inputs and outputs for more efficient routing of optical signal. Their main applications are in wavelength division multiplexing (WDM) and de-multiplexing (WDDM).

In chapter 7, we cannot etch a 90° profile angle of a thick dielectric stack with the etching tools and chemistry available to us. A sloped profile compromises the integrity of the coupler structure's dimensions. We need to look for vendors or develop new etch chemistry for straight sidewall etching of thick dielectric stack.

In chapter 11, we have shown the variation of coupling power with respect to misalignment between the fiber and the coupler. Active alignment on the Auto Aligner station was used to obtain the highest coupling efficiency. However, for large scale commercialization, passive alignment is required. Future works should focus on the integration of passive alignment techniques such as the v-groove to our current coupling scheme.

As we had demonstrated the efficient coupling from fiber to $Si_xO_yN_z$ waveguides, the future work will focus on efficient coupling into waveguide of higher index, in particular silicon single mode waveguide. There are two major challenges in applying the same design to coupling into Si or SiGe waveguides. The first is the small dimension of silicon channel waveguide. The 2^{nd} problem is the difficulty in depositing materials of progressive indices between 2.25 and above. However, windows of operation are the

varying indices of SiGe alloy and O-mixed Si materials. We should also explore non silicon-based materials and different coupling schemes.

Completed at the *Massachusetts Institute of Technology*

Cambridge, MA 02139

August 25, 2005.

Appendix A: Deposition of Amorphous Silicon by PECVD

We have the capability to deposit amorphous silicon (a-Si) using the Applied Materials PECVD chamber. Amorphous silicon can be deposited by conventional LPCVD technique at 560°C. However, the LPCVD process is time consuming and susceptible to thickness variation dependence on the position of wafer in the boat.

The deposition of a-Si film by PECVD occurs at 350°C using SiH_4, Ar or He as precursors. Here are the two recipes that we had investigated

High SiH_4 flow rate recipe	Low SiH_4 flow rate recipe
p=4.5 torr, plasma power=180 W, blocker plate-heater spacing=400 mils, SiH_4=330 sccm , Ar=1450 sccm	p=4.5 torr, plasma power=180 W, blocker plate-heater spacing=400 mils, SiH_4=165 sccm, Ar=1450 sccm

The chamber clean recipe at 350°C provided by Mark Beals is:

p=5.5 torr, plasma power=1500 W, blocker plate-heater spacing =600 mils, CF_4=150 sccm and N_2O=500 sccm.

The thickness of the film was measured first by ellipsometer. The results were confirmed with TEM images. The refractive index and the absorption coefficient k at 850 nm were measured by Filmetric system in EML.

	Deposition rate [nm/s]	**Thickness non-uniformity**	**K @ 850 nm**	**RI @850nm**
High SiH_4 flow recipe	400	0.6	0.2	3.66
Low SiH_4 flow recipe	190	0.5	0.2	3.67

The film roughness was measured by atomic force microscope. For a 5 μm x 5 μm sample area, 400 nm thick films from two above recipes have surface roughness of about 4 nm as observed in Figure A-1. This value is 10 times higher than the roughness of blank silicon wafer.

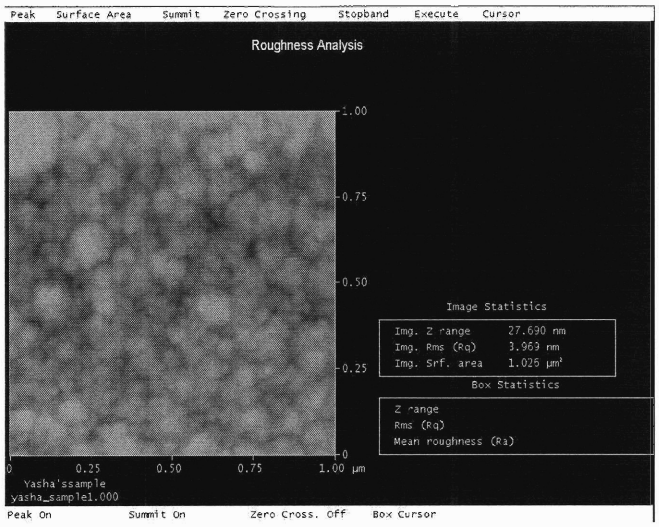

Figure A-1. The AFM results for a-Si film deposited by PECVD using SiH_4 / Ar precursor. The surface roughness is ~ 4 nm for 400 nm thick film.

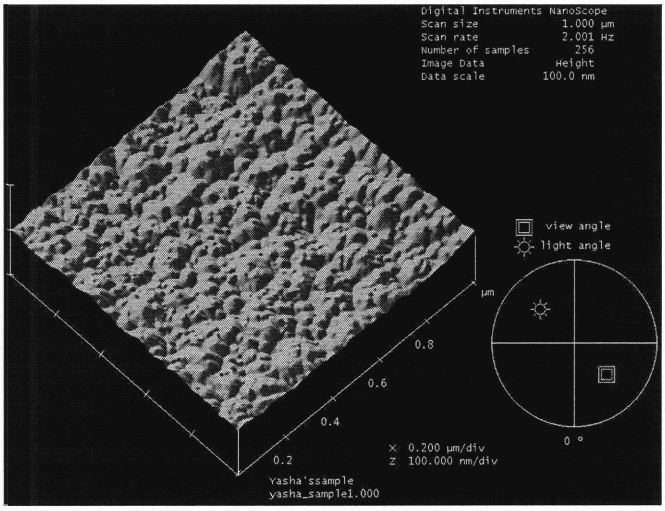

Appendix B: Chromatic Dispersion of PECVD $Si_xO_yN_z$ Films

We used the SOPRA wide-spectral ellipsometer to measure the chromatic dispersion of $Si_xO_yN_z$ films deposited with PECVD technique. The dependence of index to wavelength is stronger for films of higher indices as observed in Figure B-1. The fit function is Cauchy.

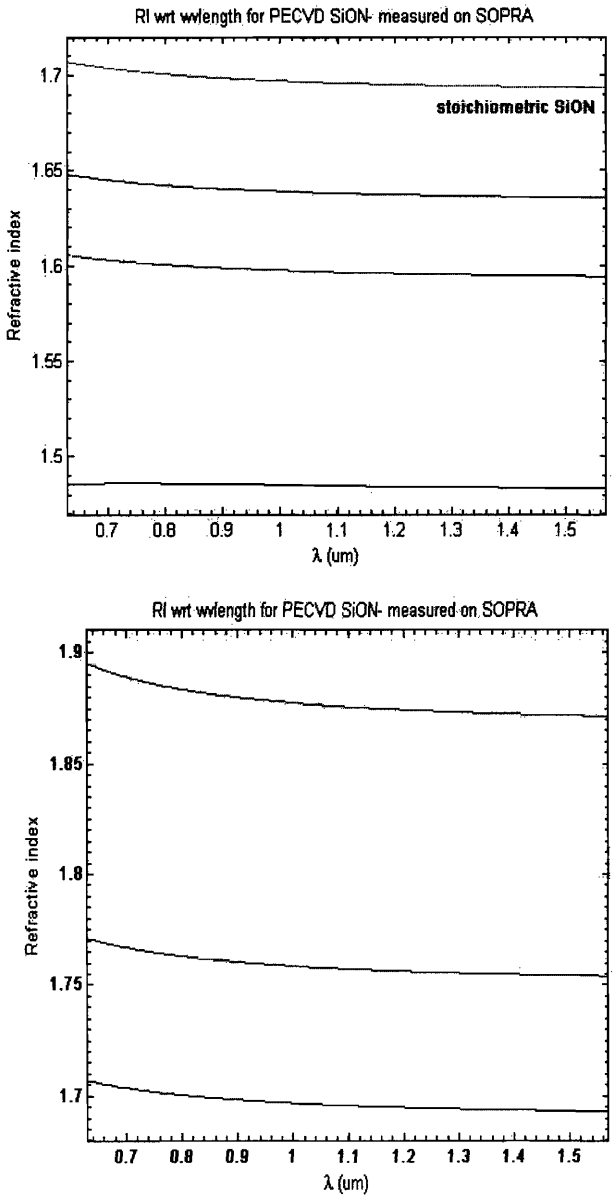

Figure B-1. Chromatic dispersion curve for $Si_xO_yN_z$ films deposited with PECVD technique. The dispersion effect is stronger with higher index (more silicon atoms) materials.

Bibliography

1. K. Lee, D. Lim, L.C. Kimerling, J. Shin, and F. Cerrina, Opt. Lett. **26**(23), 1888 (2001).
2. A. Sakai, G. Hara, and T. Baba, Jpn J Appl Phys Part 2 Letter **40**(4B), L383 (2001).
3. K. Lee, Ph. D. Thesis (DMSE- MIT, Cambridge MA, 2001), p. 41.
4. K. Worhoff, A. Driessen, P. Lambeck, L. Hilderink, P. Linders, and Th. Popma, Sens Actuators A Phys **74**(1-3), 9 (1999).
5. R. Germann, H. Salemink, R. Beyeler, G. Bona, F. Horst, I. Massarek, and B. Offrein, J. Electrochem. Soc. **147**(6), 2237 (2000).
6. R. de Ridder, K. Worhoff, A. Driessen, P. Lambeck, and H. Albers, IEEE J Sel Top Quantum Electron **4**(6), 930 (1998).
7. R. Henda, L. Laanab, E. Scheid, and R. Fourmeaux, Jpn. J. Appl. Phys. 2, Lett. **34**(4A), L437 (1995).
8. X. Liu, J. Zhang, X. Sun, Y. Pan, L. Huang, and C. Jin, Thin Solid Films **460**(1-2), 72 (2004).
9. S. Akiyama, Ph.D. Thesis (DMSE-MIT, Cambridge MA 2004), p. 35.
10. D.L. Smith, J. Vac. Sci. Technol. A, Vac. Surf. Films **11**(4, pt2), 1843 (1993).
11. W. Lanford and M. Rand, J. of Appl. Phys. **49**(4), 2473 (1978).
12. C. Boehme and G. Lucovsky, J. Vac. Sci. Technol. A, Vac. Surf. Films **19**(5), 2622 (2001).
13. S. He, V. Shannon, and T. Nguyen, Flat Panel Display Materials Symposium **424**, 109 (1996).
14. A. Lee, N. Rajagopalan, M. Le, B. H. Kim, and H. Msaad, J. Electrochem. Soc. **151** (1), F7 (2004).

15. A.I. Chowdhury, T. Klein, T. Anderson, and G. Parsons, J. Vac. Sci. Technol. A, Vac. Surf. Films **16**(3), 1852 (1998).

16. D.L. Smith, A. Alimonda, C. Chen, S. Ready, and B. Wacker, J. of Vac. Sci. & Tech. B **8**(3), 551 (1990).

17. O. Bryngdahl, J. Opt. Soc. Am. **63**(4), 416 (1973).

18. L. Soldano and E. Pennings, J. Light. Tech. **13**(4), 615 (1995).

19. R. Ulrich and G. Ankele, Appl. Phys. Lett. **27**(6), 337 (1975).

20. M. Bouda, J. van Uffelen, C. van Dam, and B. Verbeek, Elec. Lett., **30**(21), 1756 (1994).

21. L. Soldano, F. Veerman, M. Smit, B. Verbeek, A. Dubost, and E. Pennings, J. Light. Tech. **10**(12), 1843 (1992).

22. E. Pennings, R. Deri, R. Bhat, T. Hayes, and N. Andreadakis, Appl. Phys. Lett. **59**(16), 1926(1991).

23. S. Chen, J. Yu, J. Liu, Z. Wang, and J. Xia, 1st IEEE International Conf. on Grp. IV Photonics, 46 (2004).

24. H. Wei, J. Yu, Z. Liu, H. Ma, G. Li, X. Zhang, L. Wang, W. Shi, and C. Fang, CLEO Technical Digest **2**, II246 (2001).

25. J. Yu, H. Wei, X. Zhang, Q. Yan, and J. Xia, SPIE Proceedings **4582**, 57 (2001).

26. D. Lim, Ph. D. Thesis (EE-MIT, Cambridge MA 2000) p. 88.

27. A. Bhatnagar, K. Nair, R. Kumar, K. Chalapati, and Y. Patro, IEEE Photon. Tech. Lett. **6**(8), 1004 (1994).

28. F. Mustieles, E. Ballesteros, and P. Baquero, IEEE Photon. Tech. Lett. **5**(5), 551 (1993).

29. L.C. Kimerling, L. Dal Negro, S. Saini, Y. Yi, D. Ahn, S. Akiyama, D. Cannon, J. Liu, J. Sandland, D. Sparacin, K. Wada, J. Michel, and M. Watts, Top. in Appl. Phys. **94**, 89 (2004).

30. R. Soref, MRS Bull. **23**(2), 20 (1998).

31. F. Nikolajeff, O. Larsson, S. Hard, and M. Kindlundh, SPIE-Int. Soc. Opt. Eng. **5177**, 16 (2003).

32. D. Shimura, M. Uekawa, R. Sekikawa, K. Kotani, Y. Maeno, S. Sasaki, and T. Takamori, Proceedings. 54th Electron. Comp. and Tech. Conf., 219 (2004).

33. M. Fritze, J. Knecht, C. Bozler, C. Keast, J. Fijol, S. Jacobson, P. Keating, J. LeBlanc, E. Fike, B. Kessler, M. Frsih, and C. Manolatou, IEEE International SOI Conf. , 165 (2002).

34. Y. Shani, C. Henri, R. Kistler, R. Kazarinov, and K. Orlowsky, IEEE J. of Quant. Electron. **27**(3), 556 (1991).

35. C. Manolatou, Ph.D. Thesis (EECS-MIT, Cambridge, MA 2001) p. 139.

36. M. Aly, M. Abouelwafa, and M. Keshl, J. Opt. Commun. **19**(2), 54(1998).

37. J. Povlsen, Electron. Lett. **20**(13), p. 543(1984).

38. B.E.A. Saleh, M.C. Teich, *Fundamentals of Photonics* (Wiley Interscience, New York,1991) p. 18.

39. K. Shiraishi, A. Ogura, and N. Hiraguri, 11th IOOC- 23rd ECOC, 50 (1997)

40. D. Beltrami, J. Love, A. Durandet, A. Samoc, M. Samoc, B. Luther-Davies, and R. Boswell, Electron Lett. **32**(6), 549(1996).

41. R. Smith, C. Sullivan, G. Vawter, G. Hadley, J. Wendt, M. Snipes, and J. Klem, IEEE Photon. Tech Lett. **8**(8), 1052(1996).

42. K. Lee, D. Lim, D. Pan, C. Hoepfner, W. Oh, K. Wada, L.C. Kimerling, K. Yap and M. Doan, Opt. Lett. **30**(5), 498 (2005).

43. T. Shoji, T. Tsuchizawa, T. Watanabe, K. Yamada, and H. Morita, Electron. Lett. **38**(25), 1669 (2002).

44. V. Almeida, R. Panepucci, and M. Lipson, Opt. Lett. **28**(15), 1302 (2003).

45. K. Yamada, M. Notomi, A. Shinja, I. Yokohama, T. Shoji, T. Tsuchizawa, T. Watanabe, J. Takahashi, E. Tamechika, and H. Morita, Proc SPIE Int Soc Opt Eng **4870,** 324(2002).

46. Y. Shani, C. Henri, R. Kistler, and D. Ackerman, Appl. Phys. Lett. **55**(23), 2389 (1989).

47. S. Janz, A. Delage, A. Bogdanov, D. Dalacu, B. Lamontagne, and D. Xu, 1st IEEE International Conference on Group IV Photonics, 148 (2004).

48. T. Montalbo, M.S. Thesis (DMSE- MIT, Cambridge, MA 2004) p. 36.

49. K.Yee, IEEE Trans. Antennas Propag. **AP-14**(3), 302 (1966).

50. A. Sakai, G. Hara, and T. Baba, Jpn. J. of Appl. Phys., Part 2 (Letters). **40**(4B), L383 (2001).

51. W. Graf, D. Basso, F. Gautier, J. Martin, E. Sabouret, and O. Skinner,1998 IEEE/SEMI Conference and Workshop, 314 (1998).

52. R. Castellano, Sol. Stat. Tech., **27**(5), 203 (1984).

53. K. Ueno, T. Kikkawa, and K. Tokashiki, J. Vac. Sci. Technol. B, Microelectron. Nanometer Struct.. **13**(4), 1447 (1995).

54. G. Oehrlein, H. Williams, J. Appl. Phys. **62**(2), 662 (1987).

55. H. Lehmann, R. Widmer, J. Vac. Sci. Technol., **15**(2), 319 (1978).

56. G. Oehrlein, Y. Zhang, D. Vender, and M. Haverlag, J. Vac. Sci. Technol. A, Vac. Surf. Films **12**(2), 323 (1994).

57. G. Zhao, Proceedings of the 11th Symp. on Plasm. Proc., (1996). 58. H. Chae, S. Vitale, H. Sawin, J. Vac. Sci. Technol. A, Vac. Surf. Films **21**(2), 381(2003).

59. X. Li, M. Schaepkens, G. Oehrlein, R. Ellefson, L. Frees, N. Mueller, and N. Korner, J. Vac. Sci. Technol. A, Vac. Surf. Films **17**(5), 2438 (1999).

60. H. Anderson, S. Radovanov, J. Mock, and P. Resnick, Plasm. Sourc. Sci. Technol. (UK) 3(3), 302 (1994).

61. Y. Liu, Y. Tu, W. Lain, B. Chan, and M. Chi, IEEE ASMC, 153 (2000).

62. K. Rho, J. of Vac. Sci. & Tech. B **18**(6), 3476 (2000).